ADVANCED TECHNIQUES FOR THE DESIGN OF MIMO FREE SPACE OPTICAL COMMUNICATION SYSTEMS

by

Tuğba Özbilgin

B.S., Electrical and Electronics Engineering, Bilkent University, 2004

M.S., Electrical and Computer Engineering, Koç University, 2008

Submitted to the Institute for Graduate Studies in
Science and Engineering in partial fulfillment of
the requirements for the degree of
Doctor of Philosophy

Graduate Program in Electrical and Electronic Engineering

Boğaziçi University

2016

ADVANCED TECHNIQUES FOR THE DESIGN OF MIMO FREE SPACE OPTICAL COMMUNICATION SYSTEMS

APPROVED BY:

Assoc. Prof. Mutlu Koca (Thesis Supervisor)	.....
Prof. Hakan Deliç	.....
Prof. Cem Ersoy	.....
Prof. Murat Uysal	.....
Assist. Prof. Heba Yüksel	.....

DATE OF APPROVAL: 09.12.2015

ACKNOWLEDGEMENTS

First I would like to thank my supervisor Assoc. Prof. Mutlu Koca for his guidance throughout my Ph.D. with his knowledge and valuable advices.

I am grateful to my dissertation committee members Prof. Hakan Deliç, Prof. Cem Ersoy, Assist. Prof. Heba Yüksel and Prof. Murat Uysal for critical reading of the dissertation and for their valuable comments.

I thank Scientific and Technological Research Council of Turkey (TÜBİTAK) for encouraging me to pursue a graduate study.

Finally I thank my family for providing me a morale support that helped me in hard days of my research.

This work is supported by TÜBİTAK under Contract 111E274, and the Boğaziçi University Research Fund under Contract 9800.

Abstract

ADVANCED TECHNIQUES FOR THE DESIGN OF MIMO FREE SPACE OPTICAL COMMUNICATION SYSTEMS

Free space optical (FSO) communication is an effective alternative to radio frequency (RF) communication in terms of potential high data rates, cost efficiency and wide bandwidth on unregulated spectrum. However, FSO systems are susceptible to severe atmospheric turbulence conditions causing random fluctuations in the intensity and phase of the optical signal. These turbulence induced fading effects may severely degrade the FSO system performance, limiting its use to only short-range applications and clear weather conditions. In this dissertaion, with the motivation to overcome these limitations, analysis and design of FSO communication systems are considered. First a unified framework for determining the inter-aperture separations in multiple-input-multiple-output (MIMO) FSO systems such that the transmitter-receiver paths are resolvable is presented. Second a novel non-coherent MIMO optical modulation method combining optical spatial modulation (OSM) with joint pulse position and amplitude modulations, which offers better power and spectral efficiencies than conventional MIMO optical modulation methods, is proposed. Then two novel FSO communication approaches based on polarization shift keying (POLSK) are considered. The first non-coherent approach combines MIMO POLSK with pulse position modulation (PPM) constituting a good compromise between power and spectral efficiencies compared to standard uses of PPM and POLSK, while the second employs POLSK in an OSM based MIMO architecture and introduces a spectrally efficient coherent FSO communication scheme that also offers better error performance gains than other spectrally efficient modulation techniques. Finally error ratios belonging to separate signalling dimensions of these POLSK schemes are evaluated and unequal error protection (UEP) is offered to optimize the error control coding gains attained.

ÖZET

ÇGÇÇ SERBEST UZAY OPTİK İLETİŞİM SİSTEMLERİ TASARIMI İÇİN İLERİ TEKNİKLER

Serbest uzay optik (SUO) haberleşme sistemleri yüksek veri hızı, ekonomiklilik ve düzenlemesiz spektrum üzerinde geniş bant genişliği gibi potansiyelleri açısından radyo frekans (RF) haberleşme sistemlerine alternatif oluşturmaktadır. Ancak SUO sistemler optik sinyalin genliği ve fazı üzerinde dalgalanmalara sebep olan sert atmosferik türbülans şartlarından muzdariptir. Bu türbülans temelli sönümleme SUO sistemlerin başarımını ciddi bir şekilde kötüleştirip kullanım alanlarını kısa mesafe uygulamalar ve açık hava koşulları ile sınırlandırabilir. Bu tezde bu kısıtlamaların üstesinden gelmek motivasyonu ile SUO haberleşme sistemlerinin analizi ve tasarımı ele alınacaktır. İlk olarak çok-girdili-çok çıktılı (ÇGÇÇ) SUO sistemlerde alıcı-verici arası kanal iletimlerinin birbirinden ayırt edilebilir olmasına imkan verecek açıklık arası mesafelerin belirlenmesine yönelik genelleştirilmiş bir çerçeve sunulacaktır. İkinci olarak optik uzamsal kiplenim (OUK) yöntemini dürtü konumlu genlik kiplenimi ile birlikte kullanan ve geleneksel ÇGÇÇ optik kiplenim yöntemlerinden daha iyi güç ve spektral etkinlik sağlayan evreuyumsuz bir optik kiplenim yöntemi önerilecektir. Ardından polarizasyon kaydırmalı kiplenim (POLKK) temelli iki yeni SUO iletişim yaklaşımı ele alınacaktır. Bunlardan evreuyumsuz olan ilki ÇGÇÇ POLKK'yi dürtü konumlu kiplenim (DKK) ile birleştirerek DKK ve POLKK'nin standart kullanımlarına göre güç ve spektral etkinlik arasında ödünleşim sağlamakta olup, evreuyumlu olan ikincisi ise POLKK'yi OUK temelli ÇGÇÇ mimari altında kullanarak diğer spektral etkin yöntemlere nazaran daha iyi hata başarım kazançları sağlamaktadır. Son olarak bu POLKK temelli yöntemlerin farklı sinyalizasyon boyutlarına ait hata oranları değerlendirilip hata kontrolü kodlama ile elde edilecek kazanç artırımlarının en iyileştirilmesi maksatıyla eşit olmayan hata koruması önerilecektir.

Contents

ACKNOWLEDGEMENTS . . . iii
Abstract . . . iv
ÖZET . . . v
List of Figures . . . vii
List of Tables . . . xii
LIST OF SYMBOLS . . . xiii
LIST OF ACRONYMS/ABBREVIATIONS . . . xvii
1. INTRODUCTION . . . 1
1.1. Background . . . 1
1.2. Research Motivation and Contributions . . . 2
1.3. Outline of the Dissertation . . . 8
2. FUNDAMENTALS OF FREE SPACE OPTICAL COMMUNICATION . . . 9
2.1. Overview of FSO Communication Systems . . . 9
2.2. System Configuration . . . 12
2.2.1. Impact of Atmospheric Effects on the FSO Channels . . . 12
2.2.2. Channel Fading Models . . . 15
2.2.3. Optical Modulation and Detection Schemes . . . 17
2.3. Overview of Scintillation Mitigation Techniques . . . 19
2.4. Conclusion . . . 22
3. INTER - APERTURE CORRELATION IN MIMO FREE SPACE OPTICAL SYSTEMS . . . 23
3.1. Optical Scintillation . . . 26
3.2. Channel Correlation for Point Apertures . . . 27
3.3. Impact of Aperture Diameter on Channel Correlation . . . 30
3.4. Design Guidelines for Resolvable Channels . . . 41
3.5. Conclusion . . . 43
4. OPTICAL SPATIAL MODULATION OVER ATMOSPHERIC TURBULENCE CHANNELS . . . 44
4.1. System Model . . . 46

4.2. ABEP Analysis 51
4.2.1. Error Types 53
4.2.2. APEP Analysis Under Weak-to-Moderate Turbulence 56
4.2.3. APEP Analysis Under Moderate-to-Strong Turbulence . . . 58
4.3. ABEP Bound with Coded SPPAM 60
4.4. Simulation Results 61
4.5. Conclusion 70
5. POLARIZATION DIVERSITY IN MIMO COMMUNICATION OVER ATMOSPHERIC TURBULENCE CHANNELS 72
5.1. Non-Coherent Polarization Shift Keying with Pulse Position Modulation 74
5.1.1. System Model 74
5.1.2. ABEP Analysis 77
5.1.2.1. Error Types 78
5.1.2.2. APEP Analysis Under Weak-to-Moderate Turbulence 79
5.1.2.3. APEP Analysis Under Moderate-to-Strong Turbulence 80
5.2. Coherent Polarization Shift Keying with Spatial Modulation 81
5.2.1. System Model 82
5.2.2. ABEP Analysis 84
5.3. Coded architectures 86
5.4. Simulation Results 95
5.4.1. Non-coherent PPM-BPOLSK system 95
5.4.2. Coherent SM-POLSK system 96
5.5. Conclusion 100
6. CONCLUSION AND FUTURE WORK 101
Bibliography 104

List of Figures

Figure 2.1. Distortion of a laser beam propagating through atmosphere. . 14

Figure 2.2. Atmospheric effects on a Gaussian beam. (a) Original beam shape, (b) random changes in the width and position of the beam in time, (c) average observed beam shape. 14

Figure 2.3. Illustration of diversity techniques: (a) Aperture averaging, (b) diversity combining, (c) spatial multiplexing (if the transmit apertures send different signals) or repetition coding (if the transmit apertures send the same signal), (d) spatial modulation. 20

Figure 2.4. SM principle for a 4 transmitter 4-ary SM system. (a) Bit mappings for transmitter antenna and symbol indices, (b) Illustration of the SM algorithm. 21

Figure 3.1. NCF for (a) plane waves and (b) spherical waves. 31

Figure 3.2. NCF including aperture effects for (a) plane waves and (b) spherical waves. 33

Figure 3.3. NCF vs. inter aperture separation for various link distances and Rytov variances (solid, dashed and dotted curves are for point source, $D = 1$ cm and $D = 10$ cm, respectively) with a fixed structure parameter of $C_n^2 = 1.4 \times 10^{-14} \mathrm{m}^{-2/3}$ (a) for plane waves, (b) for spherical waves. 34

Figure 3.4. NCF vs. inter aperture separation for various link distances and Rytov variances (solid, dashed and dotted curves are for point source, $D = 1$ cm and $D = 10$ cm, respectively) with a fixed structure parameter of $C_n^2 = 7.4 \times 10^{-14} \mathrm{m}^{-2/3}$ (a) for plane waves, (b) for spherical waves. 35

Figure 3.5. Correlation width ρ_c vs. Rytov variance for a link distance of $L = 1$ km (a) for plane waves and (b) for spherical waves. Dashed and solid curves are for $\lambda = 0.85\,\mu$m and $\lambda = 1.55\,\mu$m, respectively. 36

Figure 3.6. Correlation width ρ_c vs. Rytov variance for a link distance of $L = 3$ km (a) for plane waves and (b) for spherical waves. Dashed and solid curves are for $\lambda = 0.85\,\mu$m and $\lambda = 1.55\,\mu$m, respectively. 37

Figure 3.7. Correlation width ρ_c vs. Rytov variance for a link distance of $L = 5$ km (a) for plane waves and (b) for spherical waves. Dashed and solid curves are for $\lambda = 0.85\,\mu$m and $\lambda = 1.55\,\mu$m, respectively. 38

Figure 3.8. Comparison of theoretical and numerical approach for a fixed Rytov variance of $\sigma_R^2 = 16$ and for various link distances. Solid curves with markers show the theoretical results whereas dashed curves denote the curve fitting values from numerical results. . 39

Figure 4.1. System model for SPPAM. Tx stands for transmitter and Rx stands for receiver. $\mathbf{s}$ and $\widehat{\mathbf{s}}$ are the input and estimated bit-streams, respectively. 47

Figure 4.2. System model for coded SPPAM 61

Figure 4.3. Accuracy of Kernel density estimates for (a) log-normal and (b) Gamma-Gamma distributions. 62

Figure 4.4. Performance results and theoretical upper bounds for the uncoded and coded SPPAM systems under (a) log-normal fading with $\sigma_I^2 = 0.5$ and (b) Gamma-Gamma fading with $\sigma_I^2 = 1.09$. 63

Figure 4.5. Simulation results at 1 b/s/Hz for (a) log-normal and (b) Gamma-Gamma distributed channels 64

Figure 4.6. Simulation results at 2 b/s/Hz for (a) log-normal and (b) Gamma-Gamma distributed channels 65

Figure 4.7. Simulation results at 3 b/s/Hz for (a) log-normal and (b) Gamma-Gamma distributed channels 66

Figure 4.8. Simulation results for the uncoded and coded SPPAM systems (a) at 2 b/s/Hz and (b) 3 b/s/Hz for Gamma-Gamma fading with scintillation indices $\sigma_I^2 = 1.09$ for $D = 2$ cm, $\sigma_I^2 = 0.42$ for $D = 10$ cm and $\sigma_I^2 = 0.22$ for $D = 20$ cm. 67

Figure 4.9. Effect of SI on the performance of the SPPAM system for (a) log-normal and (b) Gamma-Gamma distributed channels . . . 68

Figure 4.10. Effect of SI on the performance of type-IV and sum of type-I, II and III errors for (a) log-normal and (b) Gamma-Gamma distributed channels 69

Figure 5.1. System model for PPM-BPOLSK. Tx stands for transmitter and Rx stands for receiver. $\mathbf{u}$ and $\widehat{\mathbf{u}}$ are the input and estimated bitstreams, respectively. 75

Figure 5.2. PPM-BPOLSK transceiver model. (a) Transmitter model for the i-th transmitter and (b) receiver model for the j-th receiver. TL, PD, PBS and PBC stand for transmitting laser, photodiode, polarization beam splitter and polarization beam combiner, respectively. 76

Figure 5.3. System model for SM-MPOLSK. Tx stands for transmitter and Rx stands for receiver. $\mathbf{u}$ and $\widehat{\mathbf{u}}$ are the input and estimated bitstreams, respectively. 81

Figure 5.4. SM-MPOLSK transceiver model. (a) Transmitter model for the i-th transmitter and (b) receiver model for the j-th receiver. TL, PBS, PBC, PM, AM, OBPF, BPF, LO, AFC, PD and MF stand for transmitting laser, polarization beam splitter, polarization beam combiner, phase modulator, amplitude modulator, optical band pass filter, band pass filter, local oscillator, automatic frequency controller, photodiode and matched filter, respectively. 84

Figure 5.5. Performance results for the uncoded (a) 4PPM-BPOLSK and (b) $N_t = 4$ SM-8POLSK systems under Gamma-Gamma fading with $\sigma_I^2 = 1.122$. 86

Figure 5.6. Transceiver model for the UEP coded PPM-BPOLSK system. (a) Transmitter model and (b) receiver model. 89

Figure 5.7. Performance results for the coded (a) $R = 7/10$ UEP 4PPM-BPOLSK and (b) $R = 2/3$ UEP $N_t = 4$ SM-8POLSK systems under Gamma-Gamma fading with $\sigma_I^2 = 1.122$. 90

Figure 5.8. Transceiver model for the UEP coded SM-MPOLSK system. (a) Transmitter model and (b) receiver model. 91

Figure 5.9. Performance results and theoretical upper bounds for the uncoded and coded PPM-BPOLSK systems under (a) log-normal fading with $\sigma_I^2 = 0.5$ and (b) Gamma-Gamma fading with $\sigma_I^2 = 1.22$. 96

Figure 5.10. Performance results for the PPM-BPOLSK system under (a) log-normal fading with $\sigma_I^2 = 0.5$ and (b) Gamma-Gamma fading with $\sigma_I^2 = 1.22$. 97

Figure 5.11. Performance results and numerical upper bounds for the uncoded and coded SM-MPOLSK systems under (a) log-normal fading with $\sigma_I^2 = 0.5$ and (b) Gamma-Gamma fading with $\sigma_I^2 = 1.22$. 98

Figure 5.12. Performance results at 2 b/s/Hz under Gamma-Gamma fading with $\sigma_I^2 = 1.22$. 99

Figure 5.13. Performance results at 3 b/s/Hz under Gamma-Gamma fading with $\sigma_I^2 = 1.22$. 99

List of Tables

Table 2.1. International visibility range and atmospheric losses in dB/km for 785 nm wavelength (Adapted from [1]) 13

Table 3.1. Correlation widths for plane waves under various system configurations 40

Table 3.2. Correlation widths for spherical waves under various system configurations 42

Table 4.1. A sample SM mapping for $N_t = 2$, $L = 2$ and $M = 2$ 48

Table 4.2. Spectral efficiency of modulation schemes 49

Table 4.3. Spectral efficiency of a sample selection of PAM, PPM, SSK, spatial multiplexing (MUX) and SPPAM 50

Table 4.4. Codes used in simulations 70

Table 5.1. A sample OSM and SM-MPOLSK mapping for 3 b/s/Hz spectral efficiency 85

Table 5.2. A sample bit mapping for $R = 5/8$ coded $N_t = 4$ 16POLSK system obtained with rate-1/2 encoder and puncturing 93

Table 5.3. Spectral efficiency of a sample selection of POLSK [2], SSK [3] and SM-MPOLSK 94

LIST OF SYMBOLS

a_n	Abscissa factor for the Gauss-Hermite expansion
$ABEP$	Average bit error probability of the uncoded system
$ABEP_{SOP}$	Average SOP bit error probability of the uncoded system
$ABEP_{symbol}$	Average symbol bit error probability of the uncoded system
$ABEP_{tx}$	Average transmitter index bit error probability of the uncoded system
$ABEP^C$	Average bit error probability of the coded system
$ABEP^C_{SOP}$	Average SOP bit error probability of the coded system
$ABEP^C_{symbol}$	Average symbol bit error probability of the coded system
$ABEP^C_{tx}$	Average transmitter index bit error probability of the coded system
B_d	Weighting coefficients for the convolutional code
b	Bandwidth controlling the degree of smoothing for the KDE
$b_I(\rho)$	Normalized covariance function for the extended Rytov model
$B_I(\rho)$	Covariance function for the extended Rytov model
$B_I^{pl}(\rho)$	Covariance function for plane waves
$B_I^{sp}(\rho)$	Covariance function for spherical waves
$B_X(\rho)$	Covariance function for large scale homogeneities
$B_Y(\rho)$	Covariance function for small scale homogeneities
$B_\chi(\mathbf{r}_1, \mathbf{r}_2, L)$	Log-amplitude covariance of Gaussian beam wave
C_n^2	Structure parameter
d	Beam separation
d	Hamming distance
d_{free}	Free distance of the convolutional code
D	Receive aperture diameter
$E[\cdot]$	Expected value
${}_pF_q$	Hypergeometric function
$G[\cdot]$	Meijer's G function

h	Channel coefficient
$\mathbf{H}$	Channel matrix
I	Received irradiance
$\mathrm{J}_\nu(\cdot)$	Modified Bessel function of the first kind of order ν
k	Number of input bits for the k/n convolutional code
k	Wave number
$K(\cdot)$	Known kernel function
$\mathrm{K}_\nu(\cdot)$	modified Bessel function of the second kind of order ν
L	Link distance
l_0	Inner scale of turbulence
$L(\cdot)$	Log-likelihood ratio
L_0	Outer scale of turbulence
$M_S(\cdot)$	Moment generating function
n	Number of output bits for the k/n convolutional code
N	Kernel size for KDE
$\mathcal{N}(\mu, \sigma^2)$	Normal distribution with mean μ and variance σ^2
N_e	Number of bits in error
N_{GH}	Number of terms used in the Gauss-Hermite expansion
N_r	Number of receivers
N^e_{symbol}	Number of symbol bits in error
N^e_{SOP}	Number of SOP bits in error
N_t	Number of transmitters
N^e_{tx}	Number of transmitter index bits in error
p	First of the two orthogonal polarization states
p'	Second of the two orthogonal polarization states
P	Transmitted power
P_{av}	Average power per bit
P_{lo}	Power from the local oscillator
P_r	Power of the received optical signal
$\mathrm{Prob}(\cdot)$	Probability of
r	Spectral efficiency

$\mathbf{r}$	Vector in the receiver plane transverse to the propagation distance
R	Protection rate of the convolutional code
R_s	Protection rate of the convolutional code for the symbol bits
R_{SOP}	Protection rate of the convolutional code for the SOP bits
R_{tx}	Protection rate of the convolutional code for the transmitter bits
$\Re$	Photodiode responsivity
$U_0(\mathbf{r}, L)$	Free space Gaussian beam wave at the receiver without turbulence
$\wp$	Active polarization state
w_n	Weight factor for the Gauss-Hermite expansion
α	Effective number of large scale eddies
β	Effective number of small scale eddies
β_0^2	Rytov variance for spherical waves
β_m	Phase modulation parameter of the m-th symbol from the MPOLSK constellation
ε_m	Amplitude modulation parameter of the m-th symbol from the MPOLSK constellation
ϵ_N	Adjustment parameter
$\Gamma(\cdot)$	Gamma function
λ	Wavelength
$\Psi(\mathbf{r}, L)$	Total complex phase perturbations along the propagation path
ρ	Electrical signal-to-noise ratio
ρ_0	Transverse correlation radius
ρ_c	Correlation width
σ_I^2	Scintillation index
σ_n^2	Additive white Gaussian noise variance
σ_R^2	Rytov variance for plane waves
σ_X^2	Log-amplitude variance for large scale inhomogeneities
σ_Y^2	Log-amplitude variance for small scale inhomogeneities

$\chi(\mathbf{r}, L)$	Log-amplitude perturbation for weak turbulence
$\chi_1(\mathbf{r}, L)$	Log-amplitude first order perturbation for weak turbulence

LIST OF ACRONYMS/ABBREVIATIONS

2D	Two Dimensional
ABEP	Average Bit Error Probability
AM	Amplitude Modulation
APEP	Average Pairwise Error Probability
AFC	Automatic Frequency Controller
BER	Bit Error Ratio
BPF	Band Pass Filter
BPOLSK	Binary Polarization Shift Keying
b/s/Hz	Bits per second per Hertz
BSC	Binary Symmetric Channel
DPSK	Differential Phase Shift Keying
EEP	Equal Error Protection
EGC	Equal Gain Combining
FSO	Free Space Optical
HID	Hard Input Decoding
ICI	Inter Channel Interference
i.i.d.	Independent and Identically Distributed
KDE	Kernel Density Estimation
LLR	Log Likelihood Ratio
LO	Local Oscillator
MIMO	Multiple-Input Multiple-Output
MISO	Multiple-Input Single-Output
MF	Matched Filter
MGF	Moment Generating Function
ML	Maximum Likelihood
MPOLSK	Multilevel Polarization Shift Keying
MUX	Spatial Multiplexing
NCF	Normalized Covariance Function

OBPF	Optical Band Pass Filter
OOK	On-Off Keying
OSM	Optical Spatial Modulation
PAM	Pulse Amplitude Modulation
PAPR	Peak-to-Average Power Ratio
PBC	Polarization Beam Combiner
PBS	Polarization Beam Splitter
PD	Photodiode
PDF	Probability Distribution Function
PM	Phase Modulation
POLSK	Polarization Shift Keying
PPAM	Pulse Position Amplitude Modulation
PPM	Pulse Position Modulation
PPM-BPOLSK	Pulse Position Modulation Binary Polarization Shift Keying
PSK	Phase Shift Keying
QAM	Quadrature Amplitude Modulation
RC	Repetition Coding
RF	Radio Frequency
Rx	Receiver
SI	Scintillation Index
SID	Soft Input Decoding
SIM	Subcarrier Intensity Modulation
SISO	Single-Input Single-Output
SM	Spatial Modulation
SM-MPOLSK	Spatial Modulation Multilevel Polarization Shift Keying
SNR	Signal-to-Noise Ratio
SOP	State of Polarization
SPAM	Spatial Pulse Amplitude Modulation
SPPAM	Spatial Pulse Position Amplitude Modulation
SPPM	Spatial Pulse Position Modulation

SSK	Space Shift Keying
TL	Transmitting Laser
Tx	Transmitter
UEP	Unequal Error Protection

1. INTRODUCTION

1.1. Background

The idea of utilizing light to send messages has it roots in ancient eras when earliest civilizations use fire and smoke to transfer military messages [4]. Greeks and Romans are known to use coded signalling systems based on fire beacons and torches even with luminous relaying stations located on the top of mountains. Although ancient human had realized that coded messages can be transmitted through open space, the visibility, range and capacity limitations prevented the intense use of free space optical (FSO) communications until the nineteenth century. In the early 1800's the U.S. military used a solar telegraph called heliograph, which transmitted messages through Morse coded flashes of sunlight reflected by mirrors. Later Alexander Graham Bell constructed the photo-phone device which modulated the sun's radiation with voice signals allowing for the transmission of sound on light beams. Although Bell contracted a patent in 1880 for the device, its first practical use came decades later in the early 1900's when U.S. military used it for communication. Nevertheless the revolution in optical communications has been the invention of optical sources, especially the laser in 1960's [5], which led to the first real FSO implementations.

Although first appeared in 1960's with the discovery of laser, FSO systems could not find immediate application due to detrimental atmospheric effects under adverse weather conditions and the invention of fibers in 1970's [6]. For this reason early interests on this technology concentrated largely on non-commercial communication areas such as military and space applications. However, in the recent decades as the demand for high speed broadband communications increased, the limited spectrum of radio frequency (RF) technology have reawakened the interest in FSO communication. Additionally rapid development of optoelectronic devices facilitated the commercialization and deployment of FSO systems in contemporary communication infrastructures. Due to the high carrier frequency of the optical spectrum ranging from 30 THz to 300 THz these systems have potential for very high data rates of 100 Tbps and

beyond [7]. In summary, FSO communication has gained attention in the research community due to its potential to overcome the limitations of RF communication in terms of potential high data rates, cost and size efficiency and wide bandwidth with no frequency spectrum regulations [5]. Today FSO communication systems find application in a vast variety of areas comprising space and satellite communications, military applications, unmanned aerial vehicles, last mile applications for fiber communications, backbone links in metropolitan or campus area networks, and back haul for cellular communications [8], [9].

Despite their advantages, FSO systems are subject to certain impairments including pointing errors, building sway, scattering due to weather conditions such as fog, rain, snow and dust, and the atmospheric turbulence caused by the variations in the refractive index of the transmission medium [10]. The most significant of these is the atmospheric turbulence as it causes random fluctuations in the intensity and phase of the optical signal, a phenomenon known as scintillation. As shown by performance evaluations in [11–13], these turbulence induced fading effects may severely degrade the FSO system performance, limiting its use to only short-range applications and clear weather conditions. For this reason combating the performance degrading atmospheric turbulence effects has been the subject of intensive experimental and theoretical researches among the FSO communication community over the past decades. The main objective of this research is to investigate FSO communication links and demonstrate scintillation mitigation techniques through designing and developing optical communication systems over atmospheric turbulence channels. In the following section we provide a brief literature review and description of the motivation and contributions of the dissertation, leaving the detailed literature survey and discussions to the related chapters.

1.2. Research Motivation and Contributions

The performance impairments due to atmospheric turbulence induced scintillation can be mitigated by exploiting several methods such as advanced modulation schemes [14], error control coding [15, 16], diversity techniques [17–27] and adaptive

optics [28]. Diversity techniques have gained widespread interest in FSO communications because the effect of scintillation can be reduced substantially through the redundancy provided by the use of multiple transmitters and/or receivers. In addition, the availability of multiple apertures at both ends of the system prevents the possible blockage of the laser beam by obstacles, making it possible to cover longer distances. However spatial correlation among the paths over FSO links may result in a significant performance degradation. As a result, as in most multiple-input-multiple-output (MIMO) techniques, the key condition for optimal functioning of MIMO FSO systems is to ensure that different communication paths experience uncorrelated scintillation effects. There have been studies such as [11, 19, 25, 29–31] considering the effect of correlation in FSO diversity systems, however channel correlation has not always been described realistically taking into account factors such as the array geometry, wave type, channel structure and other system specifications. In this regard, an optical system-based model for the spatial correlation effects according to the propagation optics and system configuration parameters would be beneficial for the design of high performance MIMO FSO systems. This model can also be used to determine the minimum inter-aperture separations so as to ensure uncorrelated scintillation or at least negligibly small correlation. Therefore a unified framework for evaluating the spatial correlations among both the transmit and receive apertures of MIMO FSO systems is presented as the first contribution of the dissertation. The proposed framework takes into account the FSO system structure parameters, link distances, wave types, turbulence conditions and aperture specifications. As a result, for any given set of system parameters, it is possible to evaluate the inter-aperture correlations. In addition, it is also possible to evaluate the minimum separation such that received beams experience uncorrelated scintillation.

For the development of FSO systems the main design consideration has been the power efficiency rather than the spectral efficiency due to the unlimited bandwidth assumption for these systems. However, recently there has been a surge of interest in systems which are also spectrally efficient. One approach to achieve higher spectral efficiency is to employ amplitude modulation schemes with higher order constellations, however these multilevel modulation schemes have higher hardware costs since

increased modulation levels cause higher peak-to-average power ratios (PAPR) and sensitivity to device nonlinearities and noise as shown in [1]. Alternatively systems with subcarrier intensity modulation (SIM) as proposed in [32] can be used to improve spectral efficiency, however these systems are inefficient in terms of power due to their DC bias requirement for making the signal non-negative. MIMO spatial multiplexing methods are also considered for the design of spectrally efficient FSO systems but usually the presence of inter-channel interference (ICI) results in relatively poor error performances as discussed in [33]. Recently, another multiplexing method called optical spatial modulation (OSM), has emerged as an alternative for spectrally efficient optical communication, where part of the incoming information bits is mapped onto one of the transmitters that will be the only active transmitter during one symbolling time while rest of the bits is used to select a modulation symbol. This operation not only improves the error performance but also increases the spectral efficiency and completely avoids ICI. Note that space shift keying (SSK) [3] has also emerged as a special form of spatial modulation (SM) where no modulation is used and only the antenna space is utilized to convey information. Despite their advantages, existing optical SM/SSK systems have a few potential drawbacks. For instance, for optical SSK presented in [34, 35], every single bit increment in the spectral efficiency requires doubling the number of transmitters. In addition, introducing resilience against channel errors via coding automatically reduces the data rate. As an alternative, in [36] SM is implemented with pulse position modulation (PPM) to provide performance and power gains but again by having the side effect of reduced spectral efficiency. Other schemes such as pulse amplitude modulation (PAM) in [37] would improve the spectral efficiency but at the cost of added power penalty.

These observations signify the need to jointly use multiple modulations and for this reason, the dissertation presents as the second contribution a novel OSM system, denoted by spatial pulse position and amplitude modulation (SPPAM), that combines the antenna shift keying principle with pulse amplitude and position modulations. Here, PAM is used to achieve a high spectral efficiency whereas PPM provides a power gain. This hybrid use of two different modulations having counteracting effects allow a flexible design according to the data rate and error performance requirements.

Notice SM based MIMO signaling has been considered for optical wireless communication before in [34–37] particularly for indoor visible light applications, however we consider the proposed OSM scheme for FSO communications over atmospheric turbulence channels. That is why another contribution of the dissertation is application of the SM principle to FSO communication for the first time in the literature.

Notice that in all the previous MIMO FSO works mentioned above, pulse-based or phase modulations are considered with either direct or coherent detection methods. However, even when used within MIMO configurations, intensity modulation schemes are highly sensitive to atmospheric turbulence effects whereas phase modulation schemes suffer from phase noise. On the other hand, as shown in [38], the state of polarization (SOP) is much less sensitive to the atmospheric turbulence than amplitude and phase. That is why, polarization shift keying (POLSK) proposed in [39] forms a feasible alternative to optical amplitude and phase modulation techniques because of its immunity to phase noise and efficiency for operation over long distances as shown in [40] and [41], respectively. Based on this idea the authors of [42] propose a non-coherent binary POLSK (BPOLSK) scheme that relies on using the SOP of a fully polarized beam having two orthogonal channels as the information bearing parameter.

Since the turbulence induced scintillation can also be reduced substantially by the redundancy provided by the use of multiple transmitters and/or receivers as mentioned above, POLSK is also utilized with MIMO FSO systems as shown in [43–45]. In all these systems coherent BPOLSK or coherent multilevel POLSK (MPOLSK) systems are investigated. On the other hand the non-coherent BPOLSK system of [42] is not considered in a MIMO architecture. With this motivation we propose as the third contribution of the dissertation a novel coded non-coherent MIMO optical modulation method, denoted by PPM-BPOLSK, which implements BPOLSK with PPM. The proposed scheme combines the power efficiency of PPM with the robustness of SOP in a non-coherent MIMO architecture to yield an efficient optical transmission method with feasible computational complexity. We show by both theoretical analysis and simulation results that the proposed method provides improved error performances

over atmospheric turbulence channels compared to systems employing only BPOLSK or PPM and thus constitutes a feasible alternative to other direct detection intensity modulation techniques in terms of power efficiency.

As discused above the required number of constellation levels for a selected spectral efficiency can be decreased by the use of OSM without sacrificing power efficiency and with less receiver complexity compared to MIMO spatial multiplexing techniques. This constellation level requirement can be further decreased with the use of polarization dimension. Thus the fourth contribution of this dissertation is a novel coherent coded MIMO OSM architecture combining the SM principle with multilevel POLSK, denoted by SM-MPOLSK, and present an error performance analysis over atmospheric turbulence channels. Because one bit is allocated to the additional polarization dimension, the proposed OSM method requires smaller constellations or less number of transmit apertures than previously proposed OSM approaches of [13, 34, 46, 47]. As validated by both theoretical analysis and simulation results, because of the inherent robustness of POLSK to channel scintillation effects, the proposed OSM method utilizing polarization dimension as well as multiple transmit/receive apertures also provides improved error performances over atmospheric turbulence channels.

Error control coding has also been an effective method to achieve robustness against scintillation as shown in [15], [16]. Equal error protection (EEP) schemes, where all the transmitted information bits are assumed to be affected similarly from channel impairments and protected with the same protection ratios, can be preferred for simplicity. However for systems like PPM-BPOLSK and SM-MPOLSK that have multiple signalling dimensions, bit groups corresponding to different dimensions can be affected unequally from the scintillation and applying the same amount of protection to all the data may be feasible but wasteful. With this motivation first the average bit error probability (ABEP) results corresponding to the two signalling dimensions of PPM-BPOLSK - that is SOP and symbol dimensions - and three signalling dimensions of SM-MPOLSK - that is transmitter index, SOP and symbol dimensions - are investigated separately, and it is shown that bits belonging to each dimension are affected unequally from the channel impairments. Then unequal error protection (UEP)

is introduced for these systems in order to optimize the performance gains obtained by error control coding, which constitutes the final contribution of the dissertation.

In summary this dissertation is mainly aimed at investigating the performance of MIMO FSO systems in atmospheric turbulence channels. Additionally the work provides a unified framework for determining the inter-aperture separations in MIMO FSO architectures. A list of contributions mentioned above can be summarized as follows:

- A unified framework for determining the inter-aperture separations in MIMO FSO systems such that the transmitter-receiver paths are resolvable is presented in Chapter 3. The analysis framework is also useful in determining the amount of spatial correlation for a given set of system configuration parameters and aperture separations. It is applicable to both point apertures and also apertures with larger diameters and can be used at both transmit and receive arrays. It is shown that the results obtained via theoretical derivations are in good agreement with those in the literature obtained via measurements or simulations.
- A novel MIMO optical modulation method combining antenna shift keying with joint pulse position and amplitude modulations is proposed in Chapter 4. The proposed approach, denoted by SPPAM, offers better power and spectral efficiencies than conventional MIMO optical modulation methods. Additionally a theoretical analysis framework for the performance of both uncoded and coded SPPAM systems in FSO communication channels is provided. Theoretical derivations are validated with simulations which illustrate the feasibility of the proposed transceiver in key design metrics such as spectral efficiency, error performance and robustness against scintillation effects.
- Two novel MIMO FSO communication approaches exploiting the polarization state of the light wave is considered in Chapter 5. The first approach, denoted by PPM-BPOLSK, combines MIMO POLSK with PPM constituting a good compromise between power and spectral efficiencies compared to standard uses of PPM and POLSK. A theoretical analysis for the performance of uncoded and coded PPM-BPOLSK systems in atmospheric turbulence FSO channels is given

and it is shown that by combining the power efficiency properties of PPM and POLSK, PPM-BPOLSK provides reduction in the required position levels of the PPM. The second approach, denoted by SM-MPOLSK, employs POLSK in the OSM architecture of Chapter 4 and introduces a spectrally efficient scheme that also offers better error performance gains than other spectrally efficient modulation techniques. It is shown by extensive simulations that by distributing some of the bits to the spatial and polarization state domains SM-MPOLSK provides reduction in the required amplitude constellation levels. By evaluating the error ratios corresponding to each signalling dimension of these multidimensional modulation schemes it is demonstrated that bits belonging to each dimension are affected unequally from the channel impairments. For this reason UEP is introduced to these systems in order to optimize the performance gains obtained by error control coding.

1.3. Outline of the Dissertation

The dissertation is organized as follows: The fundamentals of FSO communication are reviewed in Chapter 2, where the distinctive features, application areas and widely used fading models, modulation schemes and scintillation mitigation techniques of the FSO technology are presented. Chapter 3 discusses the methods to determine the inter-transmitter and inter-receiver separations rendering the independent channel statistics assumption valid for MIMO FSO architectures. In Chapter 4 SPPAM is presented as a novel optical communication scheme offering spectral/power/performance efficiencies and a design flexibility over conventional systems. Two POLSK based optical MIMO communication techniques, PPM-BPOLSK and SM-MPOLSK are presented in Chapter 5. Additionally importance of UEP is discussed in this chapter. Finally Chapter 6 summarizes the results of the previous chapters and outlines a number of possible topics for future work.

2. FUNDAMENTALS OF FREE SPACE OPTICAL COMMUNICATION

This chapter provides a through understanding of FSO systems to place the dissertation in context. First the features and applications of FSO technology are summarized and then the atmospheric effects, models used to describe these effects and modulation and detection schemes used in optical communications are reviewed. Finally an overview on techniques utilized to mitigate the turbulence induced fading is provided.

2.1. Overview of FSO Communication Systems

FSO technology finds utilization in a wide variety of applications from short range inter-chip connection and underwater networks to longer range terrestrial and inter-satellite communications whenever high data rate communication between two points is needed. Before mentioning to the application areas we first list the advantages of the technology as follows:

- Unregulated spectrum and huge bandwidth: There is almost no regulation for using optical bandwidth covering a spectral range of at least 200 THz near the infrared frequencies of the electromagnetic spectrum as mentioned in [1].
- Cost and size effectiveness: FSO devices are lighter and smaller than their RF counterparts. Additionally they offer practically the same bandwidth that fiber optical links provide, without the high installation costs.
- No need for infrastructure, and portability: Compared to fiber optical systems almost no infrastructure is needed for FSO systems, which brings construction time and portability advantages. For this reason FSO technology is very helpful for maintaining communication in difficult terrains such as mountains or crowded cities. Additionally the technology is very suitable for building temporary links such as those needed after disasters.

- Interference avoidance: The information is carried on a very narrow and directed beam which prevents interference of several FSO channels.
- High security: Since the transmitted power is concentrated in a very narrow beam its detection by other devices is almost impossible.

Despite the attractions listed above FSO communication has also potential drawbacks given below:

- Link reliability: The performance of the FSO communication links is heavily dependent on weather conditions and potential obstacles on the communication path. Adverse weather conditions, especially fog and low clouds, and short term blockings of the line-of-sight path can have serious impact on the link reliability of these systems. The severity of these random effects can be relieved substantially by diversity techniques and hybrid FSO/RF applications.
- Alignment problems: Beam wander and building sway along with the highly directionality of the transmitted laser beams and narrow field of view of the receivers constitute a primary challenge to the precise alignment of the transmitter and receiver apertures. Misalignment makes the acquisition and pointing of the transmitted beam more difficult and may result in severe power losses especially for long range operations. The misalignment induced losses can be alleviated through beam tracking techniques.

The features listed above make FSO communication attractive for high speed, reliable, cheap and easy to construct portable applications. In the sequel we mention to some of the application areas that FSO systems find use.

- Campus area networks: Campus area networks permit easy and fast data sharing among campus-wide users by interconnecting a variety of buildings such as academic and administrative units, library and dormitories located within the campus. FSO communication offers fast, reliable and cheap connectivity solutions for medium range applications within a few kilometers, rendering itself a good candidate for establishment of campus area networks.

- Last mile applications for fiber communications: The last mile problem constitutes a bottleneck for communications because no matter how high the capacity of the available fiber optical infrastructure is, the bandwidth of the data that can be delivered to the end-user is limited by the capacity of the communication link between the two. That is why, as discussed in [48] the quick and cheap deployability of FSO technology has attracted attention in solving the last mile problem in fiber optical communications.
- Backhaul for cellular networks: The need for increasing capacity, energy efficiency and coverage for cellular networks resulted in a move away from large cells with huge and high-power base stations to larger number of small microcells with increased number of base stations. This increase in the small cell deployment brought with it new challenges to maintain the backhaul connections across all the base stations in the network. Recently designing FSO communication based backhaul networks has become a promising solution to cope with these challenges by exploiting especially the cost-effectiveness of FSO infrastructures as considered in [49].
- Underwater communications: Traditionally underwater communication is accomplished through systems exploiting the propagation delay of acoustic waves. However these systems, though capable of working over very long distances, cannot provide high data rates required for short or moderate range - up to a few hundred meters - underwater applications such as underwater sensor networks and monitoring technologies. For this reason, optical underwater communication is being used to establish underwater links between mobile or stationary users over short-to-moderate distances as mentioned in [50].
- Satellite communications: Recent advances in observation technologies used in satellite systems led to a rapid increase in the demand for high capacity data transmission over space communication links. This ever increasing demand has been pushing the satellite communications to shift from RF to FSO area as mentioned in [51]. FSO systems provide higher bandwidth and better size, weight and power consumption advantages which are more significant for satellite systems compared to terrestrial communications.

2.2. System Configuration

2.2.1. Impact of Atmospheric Effects on the FSO Channels

The characteristics of FSO links depend on the medium in which the information bearing light beam propagates. For this reason it is important to observe the experience of the optical wave as it travels through the atmosphere. Light interacts with the atmosphere due to air molecules and small suspended particles moving around causing attenuation of the optical signal. This attenuation is a result of both the conversion of the internal energy of the photons interacting with matter to heat, which is called absorption, and dispersal of beam into a range of directions after its interaction with particles moving in the air, which is called scattering [52]. The amount of scattering is dependent on the relative sizes of the particles in air and the wavelength of the travelling optical beam. When the particles are the same size or larger than the wavelength the degradation in the FSO transmission is very low. That is why, rain and snow, for which the particle sizes are much larger than the wavelength, do not have severe degrading effects on the optical wave. On the other hand when the particle sizes are on the order of the wavelength the scattering is extremely high. For this reason fog and haze are the most important sources of attenuation. As discussed in [53], rain and snow can cause to attenuations up to 25 and 45 dB/km, respectively, whereas fog's deleterious effect can be up to 130 and even above 300 dB/km for moderate and dense fog conditions, respectively. A table of atmospheric losses as a function of visibility for 785 nm wavelength is given in Table 2.1 to show the relationship between atmospheric weather conditions and attenuation.

Apart from these interactions the travelling beam also experiences atmospheric turbulence arising from the mixing of air particles at different temperatures by sun-induced wind and convection. The sun light arriving the earth heats the earth surface, which in turn heats the surface air layer. This warm air then mixes turbulently with the cooler air above causing random fluctuations in the air temperature. This wind and altitude dependent temperature fluctuations result in inhomogeneities in the refractive index and cause the formation of local unstable air masses called eddies of different

Table 2.1. International visibility range and atmospheric losses in dB/km for 785 nm wavelength (Adapted from [1])

Atmospheric condition	Precipitation		Visibility (m)	Attenuation (dB/km)
Dense fog			0	315
Thick fog			200	75
Moderate fog			500	28.9
Light fog	Snow	Storm	770	18.3
Very light fog			1000	13.8
		Strong rain	1900	6.9
Light mist			2000	6.6
		Average rain	2800	4.6
Very light mist			4000	3.1
		Light rain	5900	2
			10000	1.1
Clear air		Drizzle	18100	0.6
			20000	0.54
Very clear air			23000	0.47
			50000	0.19

length scales as shown in Figure 2.1. When a light beam is transmitted it is deviated by these prism-like acting eddies during its travel through the atmosphere and the movement of these eddies is called atmospheric turbulence.

The detrimental effects that refractive index fluctuations have on the propagating optical wave are irradiance fluctuations, beam wander, beam spreading, loss of spatial coherence and random fluctuations in the irradiance and phase [6]. Beam spreading is the broadening of the beam size which reduces the amount of energy contained within the spot size. On the other hand the randomly deviation of the beam from the direction of propagation is called beam wander, which cause random wandering of

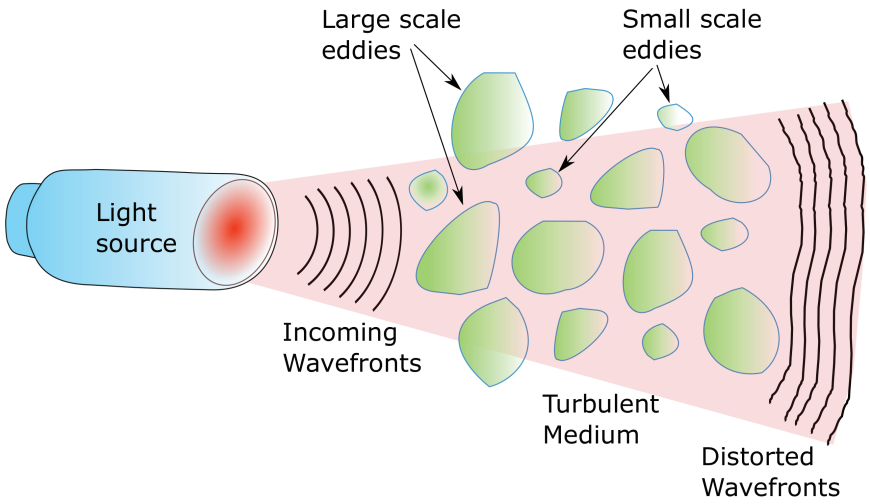

Figure 2.1. Distortion of a laser beam propagating through atmosphere.

the instantaneous beam center. The effect of turbulence on the intensity of a Gauss shaped beam is given in Figure 2.2 for demonstration purposes. As seen from the figure the original beam is broadened and thus its directionality and peak intensity is decreased due to spreading and wandering. Atmospheric turbulence has also spatial coherence destroying effects. Spatial coherence is a measure of the uniformity of the wavefront phase and its loss limits the collimation and focusing of laser beams.

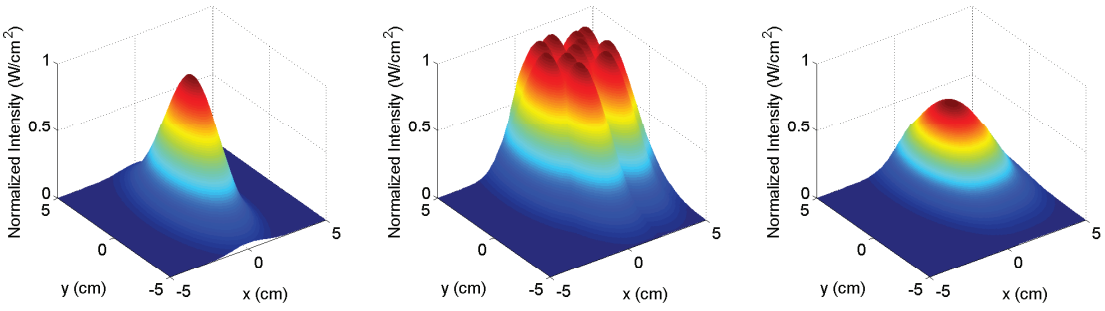

(a) (b) (c)

Figure 2.2. Atmospheric effects on a Gaussian beam. (a) Original beam shape, (b) random changes in the width and position of the beam in time, (c) average observed beam shape.

2.2.2. Channel Fading Models

Atmospheric turbulence induced scintillation can significantly degrade the performance of FSO links by causing random fluctuations in the optical signal. Especially power losses can lead to fading of the received signal below a threshold value and result in catastrophic deep fades as discussed in [6]. For this reason accurate description of the fading effects with mathematical models constitutes a key issue for determining the reliability of an optical system operating in such random environments. As a result one of the outputs of the optical wave propagation studies has been the identification of probability density functions (PDF) for describing the random fading of the optical signal. Many statistical models are offered to describe the PDF of the fading effects each valid for different ranges of turbulence strengths and with varying success.

Among these models log-normal distribution [11] is often used to describe weak turbulence effects, whereas distributions like exponential and K-distribution [54] are used to model strong atmospheric turbulence effects. Distributions for modelling a wide range of turbulence conditions such as Gamma-Gamma [15], log-normal-Rice [55], I-K and H-K [56] distributions are also proposed. In this dissertation log-normal and Gamma-Gamma distributions, which are in agreement with the experimental measurements for weak-to-moderate and moderate-to-strong atmospheric turbulence effects, respectively, as mentioned in [17] are considered.

For log-normal distributed scintillation the PDF is given by

$$f_{\mathrm{H_a}}^{LN}(h_a) = \frac{1}{h_a \sigma \sqrt{2\pi}} \exp\left(- \frac{(\log h_a - \mu)^2}{2\sigma^2} \right) \tag{2.1}$$

where h_a is the atmospheric turbulence induced channel fading coefficient, $\mu = -\log(1+\sigma_I^2)$ and $\sigma^2 = \log(1+\sigma_I^2)$ with σ_I^2 denoting the scintillation index (SI) that is a parameter used to describe the severity of the fluctuations.

The PDF corresponding to the Gamma-Gamma distributed scintillation is ex-

pressed as

$$f_{\mathrm{H_a}}^{GG}(h_a) = \frac{2(\alpha\beta)^{\frac{\alpha+\beta}{2}}}{\Gamma(\alpha)\Gamma(\beta)} h_a^{\frac{\alpha+\beta}{2}-1} \mathrm{K}_{\alpha-\beta}(2\sqrt{\alpha\beta h_a}) \tag{2.2}$$

where $\Gamma(\cdot)$ and $\mathrm{K}_\nu(\cdot)$ denote the Gamma function and the modified Bessel function of the second kind of order ν, respectively, and α and β are related to SI via the relation

$$\sigma_I^2 = \frac{1}{\alpha} + \frac{1}{\beta} + \frac{1}{\alpha\beta}. \tag{2.3}$$

In this PDF expression α and β are the parameters showing the effect of large and small scale eddies in the turbulence environment, respectively and they are defined as given in [6] as

$$\alpha = \left(\exp\left[\frac{0.49\sigma_R^2}{\left(1 + 0.65d^2 + 1.11\sigma_R^{12/5}\right)^{7/6}} \right] - 1 \right)^{-1}, \tag{2.4}$$

$$\beta = \left(\exp\left[\frac{0.51\sigma_R^2(1 + 0.69\sigma_R^2)^{-5/6}}{1 + 0.9d^2 + 0.62\sigma_R^{12/5}} \right] - 1 \right)^{-1}, \tag{2.5}$$

where σ_R^2 is the Rytov variance, $d = \sqrt{kD^2/4L}$ with $k = (2\pi/\lambda)$ and D being the wave number and the receive aperture size, respectively and L being the link distance. In FSO communication systems it is customary to measure the strength of the atmospheric turbulence by Rytov variance σ_R^2 as stated in [1]. Typically weak, moderate, strong and saturated turbulence correspond respectively to $0 < \sigma_R^2 \leq 0.3$, $0.3 < \sigma_R^2 \leq 1$, $\sigma_R^2 \approx 1$ and $\sigma_R^2 >> 1$ regions.

As discussed above FSO channels also suffer from alignment problems due to highly directionality of the transmitted beams and relatively narrow field of views of the receivers. This situation brings another random disturbing effect called pointing error or misalignment fading. Notice the random channel coefficient h considering

both atmospheric turbulence and misalignment induced fadings can be modeled as $h = h_{pe}h_a$ as given in [57], where h_{pe} and h_a are the random coefficients signifying the pointing errors and atmospheric turbulence, respectively. The PDF of the pointing error coefficient h_{pe} in terms of jitter rms variance σ_s is given by [51]

$$f_{H_{pe}}(h_{pe}) = \gamma h_{pe}^{\gamma-1} \tag{2.6}$$

where $\gamma = \theta_0^2/4\sigma_s^2$ with θ_0 being the divergence angle. Using the PDF's of random coefficients for the turbulence and misalignment fadings the combined PDF can be expressed as

$$f_H(h) = \gamma h^{\gamma-1} \int_h^\infty h_a^{-\gamma} f_{H_a}(h_a) dh_a \tag{2.7}$$

as given in [57].

2.2.3. Optical Modulation and Detection Schemes

Selection of the right modulation scheme during the design of optical communication systems is of critical importance because the selected technique determines the important system parameters such as power and spectral efficiency, which in turn affect the performance of the overall optical system in terms of battery duration, capacity and error performance efficiencies. For example power efficient modulation schemes can be chosen for battery limited applications such as wireless infrared systems or bit-error-ratio (BER) limited applications such as satellite communications, whereas bandwidth efficient ones are preferred in case high data rates are required.

Although optical communication systems can modulate the transmitted optical signal in its intensity, phase, frequency or state of SOP, a great number of FSO applications prefer intensity modulation schemes due to their simplicity. The simplest form of the intensity based modulations is on-off keying (OOK), in which binary 1 is represented with a pulse of light occupying a bit duration while binary 0 with the absence

of light. Although OOK is one of the widely used intensity based modulation techniques due to its simplicity and low implementation costs, both its spectral efficiency and noise resilience are limited. Phase modulation schemes such as phase shift keying (PSK) and differential PSK (DPSK) offer better performances compared to OOK as discussed in [58], however they suffer from phase noise and require rather complex synchronization techniques. Multilevel modulation schemes such as PAM and quadrature amplitude modulation (QAM) offer higher spectral efficiencies, but unfortunately they have higher hardware costs since increased modulation levels cause higher PAPR and sensitivity to device nonlinearities and noise as shown in [1]. SIM as proposed in [32] can also be used to attain higher spectral efficiency, however these systems are inefficient in terms of power due to their DC bias requirement for making the signal non-negative. As discussed in [59] PPM and PWM, which have a constant power level are better suited for optical communications compared to multilevel modulation methods particularly for space communications where power efficiency is a critical factor, however these pulse modulation techniques have very limited spectral efficiency. In summary despite their simplicity, intensity modulation schemes are highly sensitive to atmospheric turbulence effects whereas phase modulation schemes suffer from phase noise as discussed in [2]. On the other hand, as shown in [38], SOP is much less sensitive to the atmospheric turbulence than amplitude and phase. That is why, POLSK proposed in [39] forms a feasible alternative to optical amplitude and phase modulation techniques because of its immunity to phase noise and efficiency for operation over long distances as shown in [40] and [41], respectively.

Apart from the selection of the right modulation scheme problem, choosing the right detection technique constitutes another design consideration. The optical receiver employs either direct detection that is useful only for intensity based modulations, or coherent detection that offers performance gains especially against shot noise at the expense of more complex receiver requirements. Direct detection receivers just measure the instantaneous power impinging on the photodetector and thus can be implemented with very simple receiver structures. Coherent receivers, on the other hand, mix the incoming optical signal with another locally generated signal before being detected by the photodetector. If the locally generated signal has exactly the same

wavelength and thus frequency properties with the original signal this receiver type is called homodyne. Although homodyne receivers offer high detection sensitivities, the frequency synchronization requirement brings additional receiver complexity. On the other hand if the local oscillator and original signal frequencies are chosen to be different the receiver is said to be heterodyne, and heterodyne detection schemes are preferred more than homodyne ones due to lack of synchronization requirements as mentioned in [60]. Compared with direct detection, coherent reception offers higher signal-to-noise ratios (SNR) that can be achieved by increasing the local oscillator power to reject the background noise and also improved spectral efficiency at the cost of increased complexity. Notice optical coherent detection differs from its RF counterpart, because it is not required for the optical detection that output signal of the local oscillator has the same phase with the incoming signal.

2.3. Overview of Scintillation Mitigation Techniques

As mentioned in Chapter 1 performance impairments due to scintillation can be mitigated by exploiting several methods such as advanced modulation schemes (as discussed in the previous section), aperture averaging, diversity techniques, error control coding and adaptive optics.

The most famous of these are spatial diversity techniques which can be realized by multiple apertures at the transmit, receive or both sides of the system [19–22,33,46]. Diversity can be attained by several approaches depicted in Figure 2.3 such as aperture averaging and diversity combining at the receive side, and spatial multiplexing, repetition coding (RC) and spatial modulation at the transmit side. Notice although aperture averaging is a single output scheme it can be considered among the diversity techniques, because it relies on using a single big aperture so as to collect several uncorrelated signals and average them to reduce the SI by the so called aperture averaging factor [21]. Similar motivations exist for diversity combining techniques where the signals from sufficiently separated multiple receive apertures are collected and averaged to attain reduction in the impact of scintillation induced degradations [19]. RC, where the same signal is sent over the multiple beams at the transmitter [26], is a

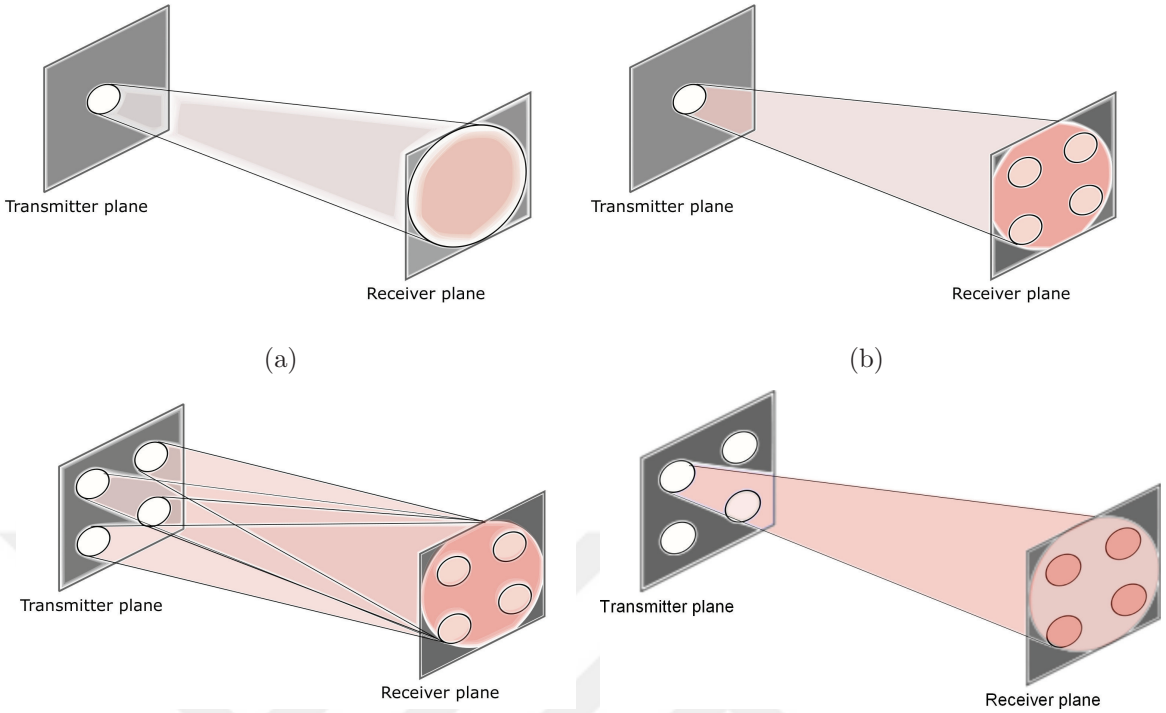

Figure 2.3. Illustration of diversity techniques: (a) Aperture averaging, (b) diversity combining, (c) spatial multiplexing (if the transmit apertures send different signals) or repetition coding (if the transmit apertures send the same signal), (d) spatial modulation.

very power efficient transmission technique achieving full diversity, however its spectral efficiency is limited since the available MIMO channel is not exploited to obtain diversity gain. Orthogonal space-time coding (OSTBC), as being another full diversity achieving technique, is also adapted to FSO systems in [22], however it is shown in [61] that RC outperforms OSTBC and the gap increases with increased number of transmit apertures. On the other hand spatial multiplexing (MUX) techniques, where each transmit source sends independent signal, provides high transmission rates at the expense of reduced diversity gain and increased demodulation complexity due to ICI as evaluated in [33].

Recently a new spatial diversity technique called OSM is proposed in [34] as a novel MIMO transmission method, where the information is conveyed simultaneously

over both the signal and antenna spaces. In SM, part of the incoming bits is used to choose a transmit antenna to be activated while the rest is used to select the modulation symbol to be sent as depicted in Figure 2.4. As shown extensively in the SM literature, this approach provides better multiplexing gains and error performances than conventional methods. Furthermore, because only one antenna is active during each signaling period, the transmit chain is simplified and the ICI is completely avoided.

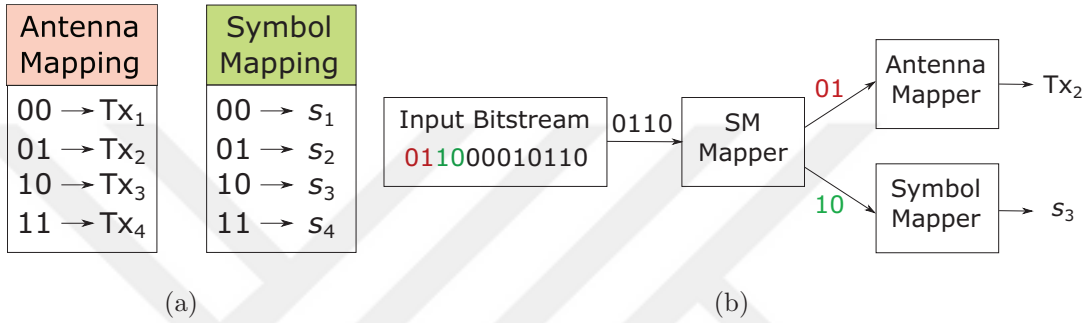

Figure 2.4. SM principle for a 4 transmitter 4-ary SM system. (a) Bit mappings for transmitter antenna and symbol indices, (b) Illustration of the SM algorithm.

Since optical channels have relatively long memory lengths they are very prone to consecutive errors arising from scintillation induced fading especially under adverse weather conditions. This situation leads to the necessity of using multiple mitigation techniques in conjunction with each other as discussed in [15, 16]. From the beginning of the FSO studies error control coding approaches have been used as supplementary fading mitigation methods so as to further increase the power efficiency of the scintillation suffering optical systems, because these techniques offer good resistance against burst errors when used with interleaving as mentioned in [62]. Despite the fact that the early work on coded FSO systems use convolutional codes generally [63, 64], recent studies consider the use of a wide variety of coding techniques including convolutional [65], low density parity check (LDPC) [66] and fountain codes [67] for turbulence mitigation.

Apart from the techniques discussed above, performance improvement can be attained by adaptive optics, where the severity of the wavefront distortions are cor-

rected through the use of deforming mirrors as mentioned in [28, 68]. This technique finds use especially in astronomy and space applications.

2.4. Conclusion

This chapter provided the introductory concepts related to the FSO communication systems with highlight on the features, challenges and applications of the technology. The performance degrading atmospheric phenomenons, importance of the models used to describe the optical channel and optical modulation and demodulation techniques were reviewed to build the essential background knowledge for the research carried out. Finally the optical scintillation mitigation techniques were briefly outlined to prepare the reader for the content of the dissertation.

3. INTER - APERTURE CORRELATION IN MIMO FREE SPACE OPTICAL SYSTEMS

Diversity techniques have gained widespread interest in FSO communications because the effect of scintillation can be reduced substantially through the redundancy provided by the use of multiple transmitters and/or receivers. In addition, the availability of multiple apertures at both ends of the system prevents the possible blockage of the laser beam by obstacles, making it possible to cover longer distances. However spatial correlation among the paths over FSO links may result in a significant performance degradation. As a result, as in most MIMO techniques, the key condition for optimal functioning of MIMO FSO systems is to ensure that different communication paths experience uncorrelated scintillation effects.

Notice that there has been works such as [11, 19, 25, 29–31] considering the effect of correlation in FSO diversity systems with weak turbulence conditions. In [11, 19, 29], the normalized spatial correlation coefficients in receiver arrays are assigned deterministically without employing any physical model. In [30], the dependence of correlation on wavelength and link distances is addressed, however again various correlation coefficients which are not based on a physical model are used in performance evaluations. An exponential correlation model is employed in [25] for transmit arrays and in [31] for multiple-input single-output (MISO) multi-hop relays. Notice that the exponential model is presented in [69] to describe the spatial correlation effects in linear antenna arrays in RF communication. However most FSO applications employ lasers with Gaussian profile beams because no diffraction patterns are formed when they pass through the apertures. The beam power is concentrated in a small cylinder around the beam axis and the intensity is circularly symmetric making the received beam profile on the photodetector also circular. Therefore 2-dimensional (2D) arrays with appropriately placed - on a circular or near circular plane - receiver apertures are able to collect the light beams better than linear aperture arrays. Moreover, the collected light intensity at each aperture in a 2D array can be assumed approximately equal

whereas in a linear array some apertures would receive less light than the others or even no light. That is why, contrary to RF communications, in most FSO applications transmit or receive apertures are not placed in linear arrays and inter-aperture separations are not described with integer multiples of a fixed distance; therefore the exponential correlation model is not really applicable for optical aperture arrays. As seen from these examples, despite being one of the fundamental factors determining the performance of the FSO diversity systems, channel correlation has not always been described realistically taking into account factors such as the array geometry, wave type, channel structure and other system specifications. In this regard, an optical system-based model for the spatial correlation effects according to the propagation optics and system configuration parameters would be beneficial for the design of high performance MIMO FSO systems. This model can also be used to determine the minimum inter-aperture separations so as to ensure uncorrelated scintillation or at least negligibly small correlation.

The condition of uncorrelated scintillation is generally validated through the assumption that each aperture in the transmit and receive arrays are placed sufficiently apart. The minimum inter-aperture separation satisfying this assumption is denoted as the "correlation width" or "correlation length" [6]. The correlation width assumption is used in [18,44,58,70,71] for receiver diversity systems to guarantee independent channel coefficients. Further the authors of [18, 70, 72] use correlation width also for determining the transmit aperture separation assuming the reciprocity of the transmit/receive sides. The correlation width is also used to determine the size of a single larger receive aperture used for aperture averaging. If the aperture size is larger than the correlation length then the impact of scintillation can be reduced significantly by aperture averaging, as used in [11,19,29], where uncorrelated scintillations from many paths are averaged together. Among the aforementioned works considering the constituent channels as statistically uncorrelated, in [71], the authors present correlation length calculations based on the Fried parameter for several configurations while in the others the apertures are simply assumed to be separated by at least the correlation width without explicitly estimating these distances according to the system specifications. However, the correlation width and thus the minimum aperture separation rely

on whether the apertures are placed at the transmitter or receiver, the channel conditions (i.e., weak or strong turbulence), wave type (i.e., plane or spherical waves) and aperture specifications (i.e. aperture diameter).

For this reason, in this work we provide a unified framework for evaluating the spatial correlations among both the transmit and receive apertures of MIMO FSO systems. The proposed framework takes into account the FSO system structure parameters, link distances, wave types, turbulence conditions and aperture specifications. As a result, for any given set of system parameters, it is possible to evaluate the inter-aperture correlations. In addition, it is also possible to evaluate the minimum separation such that received beams experience uncorrelated scintillation. As shown with extensive comparisons, the theoretical derivations agree with the measured and simulated results reported in the literature. Notice that the correlation length can be determined analytically for point apertures using the spatial covariance function obtained by the Rytov model as presented in [6]. Alternatively it is also evaluated numerically via measurements in [73] or computed by simulations as in [74]. The results and claims of [73] are used in [75–77] to assume independent channel statistics, whereas [78] refers to them to show the appropriateness of the spatial correlation assumption. In addition, the results of [6] for point apertures are extended to apertures with non-neglible diameters in [79] for receive diversity systems. However, previous work on this subject has certain limitations especially in the form of considering one or more of system parameters while omitting the others. For instance, the results of [6, 73, 74] are only limited with point apertures; the derivations of [79] are applicable to larger apertures but only for receive diversity systems. Moreover, [73, 74, 79] consider only plane waves and the results/derivations are not extended to spherical waves. In this regard, the novelty of this work is to present a unified framework which is applicable to both point and non-point apertures, plane and spherical waves, and transmit and receive diversity.

The organization of this chapter is as follows: The basics of optical scintillation is reviewed in Section 3.1. In Section 3.2 Rytov theory is introduced to define the correlation width and theoretical results for point apertures, that is apertures with

small diameters that do not exploit aperture averaging, are provided. The impact of aperture size on the channel correlation is discussed and theoretical results are provided and compared with those of other works in the literature in Section 3.3. In Section 3.4 design guidelines for resolvable paths are presented. Finally in Section 3.5 concluding remarks are provided.

3.1. Optical Scintillation

As discussed in Chapter 1 when a light beam travels through free space, random fluctuations in the air temperature result in inhomogeneities in the refractive index and cause the formation of local unstable air masses called eddies of different length scales [6]. Larger eddies are unstable and thus break up into smaller eddies. These smaller eddies successively undergo a similar break up process forming a continuum of eddy size for the transfer of energy from a macro scale L_0, called outer scale, to a microscale l_0, called inner scale. For scale sizes smaller than l_0 the turbulent eddies disappear while dissipating their energy as heat. On the other hand eddies of scale sizes larger than L_0 are assumed to be non-isotropic and their structure is not well defined. Between l_0 and L_0, eddies are assumed to be statistically homogeneous and isotropic, and geometrical optics is valid in this region.

Contributions of small scale eddies to the scintillation are associated with the turbulence cells smaller than either the first Fresnel zone $\sqrt{L/k}$ or transverse correlation radius ρ_0, whichever is smaller. Meanwhile, contributions of large scale eddies are due to the turbulence cells larger than the first Fresnel zone or the scattering disk $L/k\rho_0$, whichever is larger. Here L denotes the path length, $k = 2\pi/\lambda$ is the wave number of the electromagnetic wave, λ is the wavelength and ρ_0 is the spatial coherence radius. Spatial coherence radius is a parameter that shows the degree of the loss of spatial coherence of an initially coherent beam and is given as shown in [6] for plane waves by

$$\rho_0 = \begin{cases} (1.64 C_n^2 k^2 L l_0^{1/3})^{-1/2}, & \rho_0 \ll l_0 \\ (1.46 C_n^2 k^2 L)^{-3/5}, & l_0 \ll \rho_0 \ll L_0 \end{cases} \tag{3.1}$$

and for spherical waves by

$$\rho_0 = \begin{cases} (0.55C_n^2k^2Ll_0^{1/3})^{-1/2}, & \rho_0 \ll l_0 \\ (0.55C_n^2k^2L)^{-3/5}, & l_0 \ll \rho_0 \ll L_0 \end{cases} \tag{3.2}$$

where C_n^2 ($\mathrm{m}^{-2/3}$) is the structure parameter which varies from 1×10^{-13} for strong turbulence to 1×10^{-17} for weak turbulence, with typical average value of 1×10^{-15} [11]. Although C_n^2 shows the strength of the fluctuations, it is customary to distinguish between different fluctuation conditions by Rytov variance given by $\sigma_R^2 = 1.23C_n^2k^{7/6}L^{11/6}$ for plane waves and $\beta_0^2 = 0.492C_n^2k^{7/6}L^{11/6}$ for spherical waves ($\beta_0^2 = 0.4\sigma_R^2$). Weak and moderate fluctuations are associated with $\sigma_R^2 < 1$ whereas strong fluctuations are characterized by $\sigma_R^2 > 1$.

Small scale eddies cause scattering by diffraction whereas large scale ones cause refraction. Combination of these effects results in random changes in the beam direction which is denoted as beam wander and in intensity fluctuations which is called scintillation as discussed in Chapter 1. The beam size also increases due to diffraction. As a result both amplitude and phase of the electric field experience random fluctuations.

3.2. Channel Correlation for Point Apertures

As presented in [6], if the propagation is characterized with a line-of-sight channel the classical Rytov method can be used for the analysis of free space propagation model for weak fluctuations. In the Rytov model, the optical field at distance L from the transmitter is given by

$$U(\mathbf{r}, L) = U_0(\mathbf{r}, L)\exp[\Psi(\mathbf{r}, L)] \tag{3.3}$$

where $\mathbf{r}$, $U_0(\mathbf{r}, L)$ and $\Psi(\mathbf{r}, L)$ denote the vector in the receiver plane transverse to the propagation direction, the free space Gaussian beam wave at the receiver without turbulence and the total complex phase perturbations along the propagation path,

respectively.

The covariance function of irradiance is utilized so as to describe how the fluctuations at one point in the beam are correlated with those at another point and used to define a characteristic *correlation width* for the fluctuations. The log-amplitude covariance of a Gaussian beam wave is defined as

$$B_\chi(\mathbf{r}_1, \mathbf{r}_2, L) = \mathrm{E}[\chi_1(\mathbf{r}_1, L)\chi_1(\mathbf{r}_2, L)] - E[\chi_1(\mathbf{r}_1, L)]\mathrm{E}[\chi_1(\mathbf{r}_2, L)]$$

where $\chi(\mathbf{r}, L) = \frac{1}{2}[\Psi(\mathbf{r}, L) + \Psi^*(\mathbf{r}, L)]$ is the log-amplitude perturbation for weak turbulence and the subscript 1 of χ denotes the first order perturbation.

Classical Rytov method is limited to weak fluctuations since it does not consider the spatial coherence radius of the beam. To analyze moderate-to-strong fluctuations a modified version of the classical approach called extended Rytov method is used. In this method the received irradiance I is modeled as the product of two terms as $I = XY$ with X and Y denoting the effects of large-scale refractive and small-scale diffractive fluctuations, respectively. The covariance function for the extended model is given by

$$B_I(\rho) = B_X(\rho) + B_Y(\rho) + B_X(\rho)B_Y(\rho) \tag{3.4}$$

where $B_X(\rho)$ and $B_Y(\rho)$ denote the covariance for large and small scale inhomogeneities, respectively.

For plane waves, the covariance function, $B_I^{pl}(\rho)$, is expressed by

$$\begin{aligned} B_I^{pl}(\rho) &= \exp\left[1.06\sigma_R^2 \int_0^1 \int_0^\infty \exp\left(-\frac{\eta}{\eta_X}\right) \frac{J_0\left(\rho\sqrt{k\eta/L}\right)}{\eta^{\frac{11}{6}}} \left[1-\cos\left(\eta\xi\right)\right] d\eta d\xi \right. \\ &+ \left. 1.06\sigma_R^2 \int_0^1 \int_0^\infty \frac{J_0\left(\rho\sqrt{k\eta/L}\right)}{(\eta+\eta_Y)^{11/6}} \left[1-\cos\left(\eta\xi\right)\right] d\eta d\xi \right] - 1 \\ &\simeq \exp\left[\frac{0.49\sigma_R^2}{(1+1.11\sigma_R^{\frac{12}{5}})^{\frac{7}{6}}} {}_1F_1\left(\frac{7}{6};1;-\frac{k\rho^2\eta_X}{4L}\right)\right. \\ &+ \left. \frac{0.50\sigma_R^2}{(1+0.69\sigma_R^{\frac{12}{5}})^{\frac{5}{6}}} \left(\frac{k\rho^2\eta_Y}{4L}\right)^{\frac{5}{12}} K_{\frac{5}{6}}\left(\sqrt{\frac{k\rho^2\eta_Y}{L}}\right)\right] - 1 \end{aligned} \tag{3.5}$$

where $J_\nu(x)$ and $K_\nu(x)$ denote the modified Bessel functions of the first and second kind, respectively and ${}_pF_q$ is the hypergeometric function defined as

$${}_pF_q(a_1,a_2,\cdots,a_p;b_1,b_2,\cdots,b_q;z) = \sum_{n=0}^{\infty} \frac{(a_1)_n(a_2)_n\cdots(a_p)_n z^n}{(b_1)_n(b_2)_n\cdots(b_q)_n n!}$$

with $(a)_0 = 1$ and $(a)_n = a(a+1)\cdots(a+n-1)$ for $n \geq 1$. In (3.5), the parameters η_X and η_Y are defined as $\eta_X = 2.61/(1+1.11\sigma_R^{12/5})$ and $\eta_Y = 3(1+0.69\sigma_R^{12/5})$, respectively.

Similarly, for spherical waves the covariance function $B_I^{sp}(\rho)$ is given by

$$\begin{aligned} B_I^{sp}(\rho) &= \exp\left[2.65\beta_0^2 \int_0^1 \int_0^\infty \exp\left(-\frac{\eta\xi}{\eta_X}\right) \frac{J_0\left(\rho\xi\sqrt{k\eta/L}\right)}{\eta^{\frac{11}{6}}} \left[1-\cos\left(\eta\xi(1-\xi)\right)\right] d\eta d\xi \right. \\ &+ \left. 2.65\beta_0^2 \int_0^1 \int_0^\infty \frac{J_0\left(\rho\xi\sqrt{k\eta/L}\right)}{(\eta+\eta_Y)^{11/6}} \left[1-\cos\left(\eta\xi(1-\xi)\right)\right] d\eta d\xi \right] - 1 \\ &\simeq \exp\left[0.04\beta_0^2\eta_X^{\frac{7}{6}} {}_3F_3\left(\frac{7}{6},\frac{3}{2},2;\frac{7}{2},3,1;-\frac{k\rho^2\eta_X}{4L}\right)\right. \\ &+ 3.18\beta_0^2\eta_Y^{\frac{-5}{6}} \times {}_1F_2\left(\frac{1}{2};\frac{1}{6},\frac{3}{2};\frac{k\rho^2\eta_Y}{4L}\right) \\ &- \left. 2.22\beta_0^2\left(\frac{k\rho^2}{L}\right)^{\frac{5}{6}} {}_1F_2\left(\frac{4}{3};\frac{11}{6},\frac{7}{3};\frac{k\rho^2\eta_Y}{4L}\right)\right] - 1 \end{aligned} \tag{3.6}$$

with $\eta_X = 8.56/(1+0.19\sigma_R^{12/5})$ and $\eta_Y = 9(1+0.23\sigma_R^{12/5})$. Notice that equations (3.5) and (3.6) are valid for point apertures only and the effect of aperture averaging on the

covariance functions will be discussed in Section 3.3.

Once the covariance function is found, it is normalized to obtain the normalized covariance function (NCF) that is expressed as

$$b_I(\rho) = \frac{B_I(\rho)}{\sigma_I^2} = \frac{B_X(\rho) + B_Y(\rho) + B_X(\rho)B_Y(\rho)}{\sigma_X^2 + \sigma_Y^2 + \sigma_X^2\sigma_Y^2} \tag{3.7}$$

where σ_X^2 and σ_Y^2 are the respective log-amplitude variances of X and Y, which are given by $\sigma_X^2 = \exp(0.49\sigma_R^2/(1 + 0.111\sigma_R^{12/5)^{7/6}}) - 1$ and $\sigma_Y^2 = \exp(0.51\sigma_R^2/(1 + 0.69\sigma_R^{12/5})^{5/6}) - 1$, respectively for plane waves, and $\sigma_X^2 = \exp(0.2\sigma_R^2/(1+0.19\sigma_R^{12/5})^{7/6}) - 1$ and $\sigma_Y^2 = \exp(0.2\sigma_R^2/(1 + 0.23\sigma_R^{12/5})^{5/6}) - 1$, respectively for spherical waves. SI σ_I^2 is simply $B_I(0)$ and the correlation width ρ_c simply becomes either the zero crossing point or the $1/e^2$ point of it.

NCF's for plane and spherical waves are given in Figure 3.1 according to the solution of (3.7). Both figures are plotted for the wavelength $\lambda = 1.55$ μm and link distance $L = 2.5$ km. In all the figures, C_n^2 values of 4.65×10^{-16} and 1.4×10^{-14} m$^{-2/3}$ are used for weak-to-moderate and 7.4×10^{-14} and 1.5×10^{-13} m$^{-2/3}$ for moderate-to-strong turbulence conditions. These four C_n^2 values respectively correspond to the σ_R^2 parameters of 0.05, 1.5, 7.9 and 16 for plane waves and the β_0^2 parameters of 0.02, 0.6, 3.16 and 6.4 for spherical waves. As seen in the figures, the correlation width, which is taken as the 0 crossing point of the NCF in this dissertation, is about 7-9 cm for plane and 15-17 cm for spherical waves for weak and weak-to-moderate turbulence conditions, and for moderate-to-strong and strong turbulence conditions it is about 19-28 cm and 25-34 cm for plane and spherical waves, respectively.

3.3. Impact of Aperture Diameter on Channel Correlation

Although the extended Rytov model is useful in determining the channel correlation it is valid for point apertures only and it fails to address systems employing large apertures exploiting aperture averaging. If point apertures or apertures with a small diameter are used, smaller number of speckles fall into the receiver aperture. As a re-

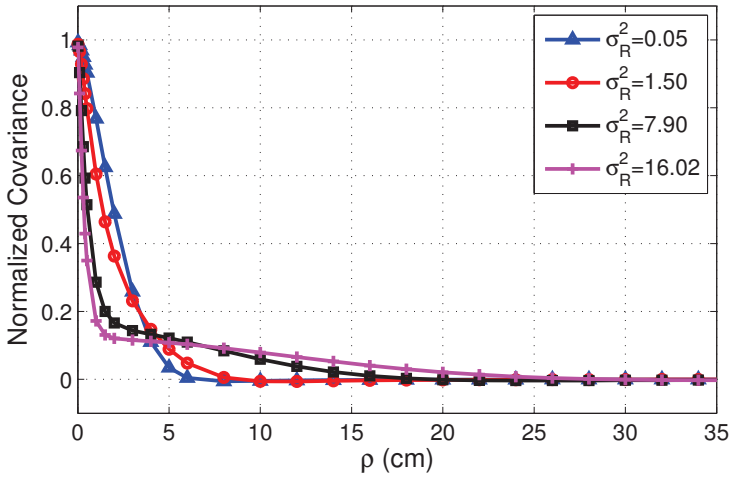

(a)

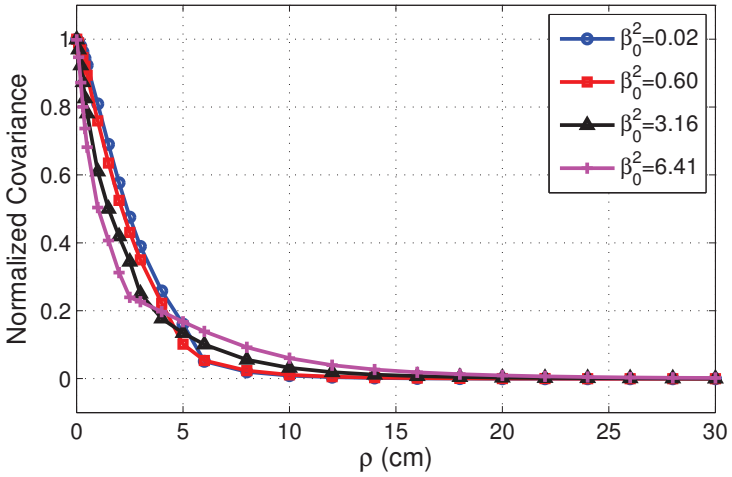

(b)

Figure 3.1. NCF for (a) plane waves and (b) spherical waves.

sult higher power levels are needed at the transmitter to ensure a certain error level even for the worst case, i.e. dark speckles. On the other hand, larger receiver apertures result in a larger number of speckles to be collected and thus aperture averaging. However, if the inter-aperture separations are small the system may again suffer from channel correlation and have a smaller aperture averaging gain factor than expected.

As shown in [79] when receiver separations are large enough, e.g. larger than 20 cm for a 2 km link distance with $\lambda = 1.06\ \mu$m and $C_n^2 = 2 \times 10^{-13}$ corresponding to a Rytov variance of $\sigma_R^2 = 22.1$, this effect is little. In general the speckle sizes which

determine the maximum receiver aperture size for the receiver to be considered as a point receiver are about $\sqrt{\lambda L}$.

According to [6], the covariance function $B_I^{pl}(\rho)$ taking the aperture size into account becomes

$$\begin{aligned} B_I^{pl}(\rho) &= \exp\left[1.06\sigma_R^2 \int_0^1 \int_0^\infty \exp\left(-\frac{\eta d^2}{4} - \frac{\eta}{\eta_X}\right) \frac{J_0\left(\rho\sqrt{k\eta/L}\right)}{\eta^{\frac{11}{6}}} \left[1-\cos\left(\eta\xi\right)\right] d\eta d\xi \right. \\ &+ \left. 1.06\sigma_R^2 \int_0^1 \int_0^\infty \exp\left(-\frac{\eta d^2}{4}\right) \frac{J_0\left(\rho\sqrt{k\eta/L}\right)}{(\eta+\eta_Y)^{11/6}} \left[1-\cos\left(\eta\xi\right)\right] d\eta d\xi \right] - 1 \\ &\simeq \exp\left[\frac{0.49\sigma_R^2}{(1++0.65d^2+1.11\sigma_R^{\frac{12}{5}})^{\frac{7}{6}}} {}_1F_1\left(\frac{7}{6};1;-\frac{k\rho^2\eta_X}{L(4+d^2\eta_X)}\right)\right. \\ &+ \left. \frac{0.51\sigma_R^2(1+0.69\sigma_R^{\frac{12}{5}})^{\frac{-5}{6}}}{1+0.90d^2+0.62d^2\sigma_R^{\frac{12}{5}}} \left(\frac{k\rho^2\eta_Y}{L}\right)^{\frac{5}{12}} K_{\frac{5}{6}}\left(\sqrt{\frac{k\rho^2\eta_Y}{L}}\right)\right] - 1. \end{aligned} \tag{3.8}$$

for plane waves and

$$\begin{aligned} B_I^{sp}(\rho) &= \exp\left[2.65\beta_0^2 \int_0^1 \int_0^\infty \exp\left(-\frac{\eta d^2}{4} - \frac{\eta\xi}{\eta_X}\right) \frac{J_0\left(\rho\xi\sqrt{k\eta/L}\right)}{\eta^{\frac{11}{6}}} \right. \\ &\left[1-\cos\left(\eta\xi(1-\xi)\right)\right] d\eta d\xi + 2.65\beta_0^2 \int_0^1 \int_0^\infty \exp\left(-\frac{\eta d^2}{4}\right) \frac{J_0\left(\rho\xi\sqrt{k\eta/L}\right)}{(\eta+\eta_Y)^{11/6}} \\ &\left. \left[1-\cos\left(\eta\xi(1-\xi)\right)\right] d\eta d\xi \right] - 1 \end{aligned} \tag{3.9}$$

for spherical waves where D is the aperture diameter and $d = \sqrt{kD/4L}$ in both equations. Notice that the NCF is simply $b_I(\rho) = B_I(\rho)/\sigma_I^2$ again.

The normalized covariance curves for plane and spherical waves including the receiver aperture effects are given in Figure 3.2 for aperture sizes of $D = 1$ cm and $D = 10$ cm using the same parameter setup as Figure 3.1. It is seen that for stronger turbulence conditions the 0 level is almost the same for both aperture sizes. Comparing the results of Figure 3.2 with Figure 3.1 it is observed that the two models, that is the one for point sources and the other taking the receiver aperture into account, coincide at the 0 level especially for high Rytov variances. Thus one may conclude

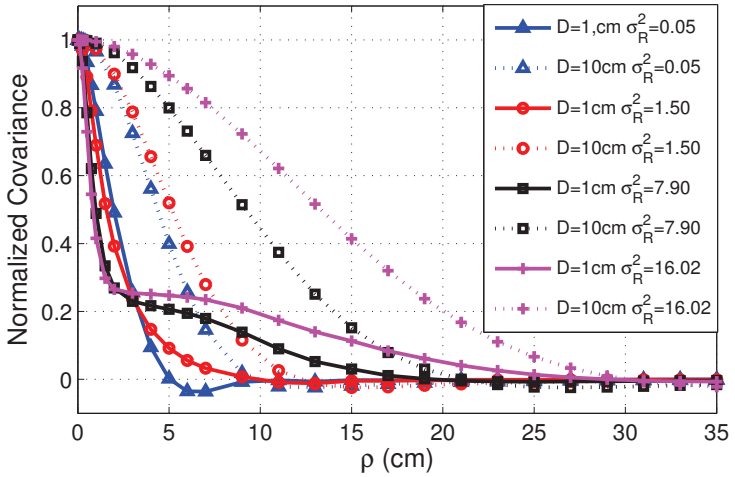

(a)

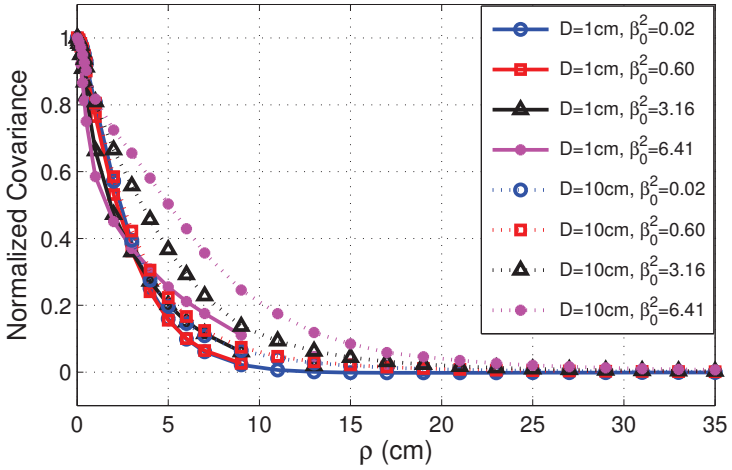

(b)

Figure 3.2. NCF including aperture effects for (a) plane waves and (b) spherical waves.

that for stronger turbulence conditions aperture size has negligible effect on channel correlation and plays almost no role in determining the aperture separations. As a final point the authors of [79] show that based on the plane wave model, the correlation width is approximately $\sqrt{\lambda L}$ and $2L/k\rho_0$ for weak and strong turbulence conditions, respectively which comply with the presented results.

Notice that Rytov variance is a function of the link distance and that is why, the results shown in Figure 3.1 and Figure 3.2 for fixed Rytov variances correspond to

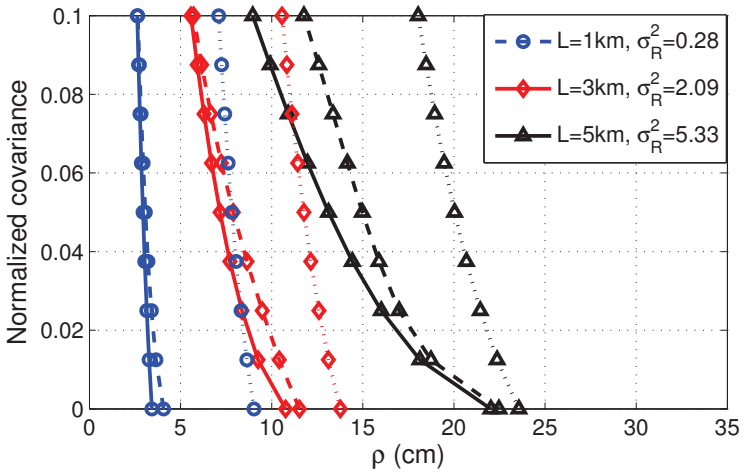

(a)

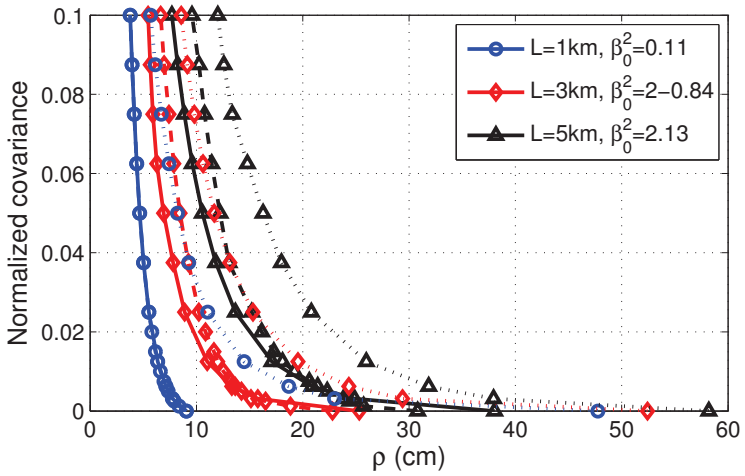

(b)

Figure 3.3. NCF vs. inter aperture separation for various link distances and Rytov variances (solid, dashed and dotted curves are for point source, $D = 1$ cm and $D = 10$ cm, respectively) with a fixed structure parameter of $C_n^2 = 1.4 \times 10^{-14}\mathrm{m}^{-2/3}$ (a) for plane waves, (b) for spherical waves.

different structure parameters. As an alternative, instead of considering a fixed Rytov variance, we fix the structure parameter and depict the relation of the correlation width to various link distances each corresponding to a different Rytov variance as shown in Figure 3.3 for $C_n^2 = 1.4 \times 10^{-14}$ m$^{-2/3}$ and Figure 3.4 for $C_n^2 = 7.4 \times 10^{-14}$ m$^{-2/3}$ considering plane and spherical waves. It is seen that correlation widths for $C_n^2 = 1.4 \times 10^{-14}$ m$^{-2/3}$ vary from 4 cm for plane and 9 cm for spherical waves at 1

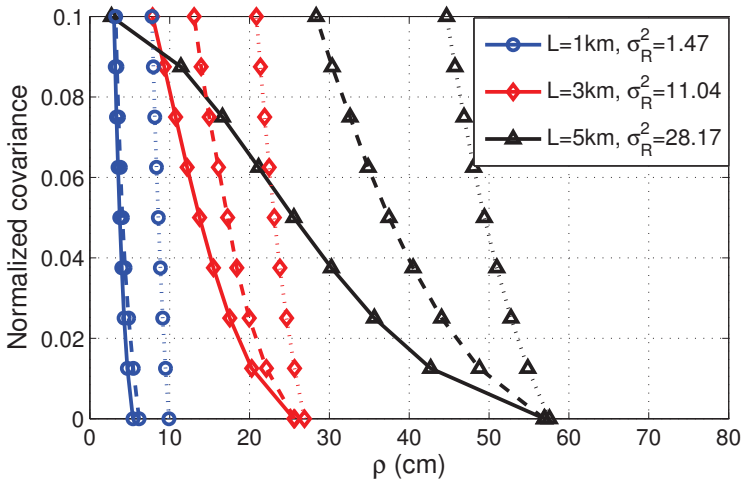

(a)

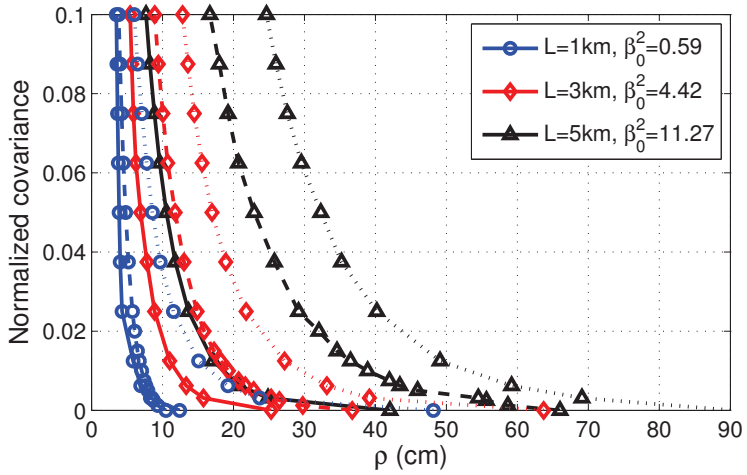

(b)

Figure 3.4. NCF vs. inter aperture separation for various link distances and Rytov variances (solid, dashed and dotted curves are for point source, $D = 1$ cm and $D = 10$ cm, respectively) with a fixed structure parameter of $C_n^2 = 7.4 \times 10^{-14}\mathrm{m}^{-2/3}$ (a) for plane waves, (b) for spherical waves.

km to 23 cm for plane and 48 cm for spherical waves at 5 km link distances whereas the same parameters for $C_n^2 = 7.4 \times 10^{-14}$ m$^{-2/3}$ are 5 cm to 55 cm for plane and 12 cm to 93 cm for spherical waves. The coincidence of the point source, $D = 1$ cm and $D = 10$ cm curves at 0 level for high Rytov variances is also apparent in Figure 3.3-a, Figure 3.3-c, Figure 3.4-a and Figure 3.4-c. Notice that the Rytov variances indicate a weak turbulence at short link distances and a strong one as the distances increase

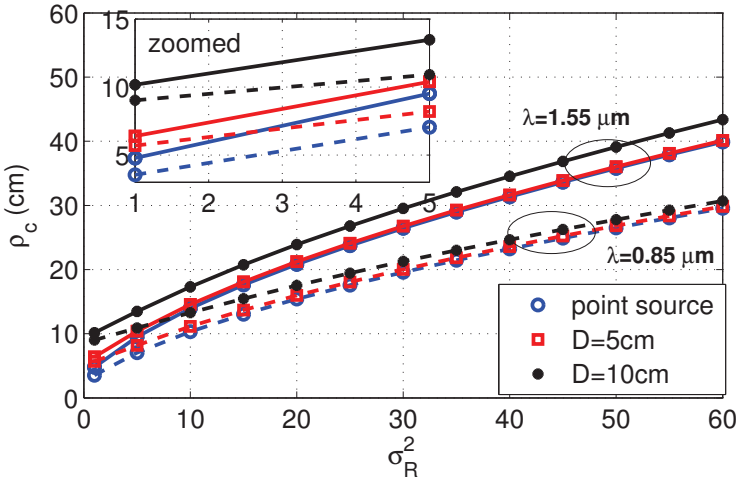

(a)

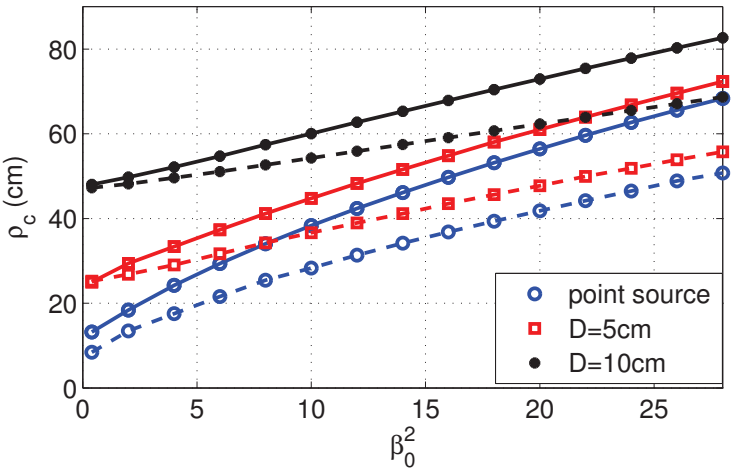

(b)

Figure 3.5. Correlation width ρ_c vs. Rytov variance for a link distance of $L = 1$ km (a) for plane waves and (b) for spherical waves. Dashed and solid curves are for $\lambda = 0.85\ \mu$m and $\lambda = 1.55\ \mu$m, respectively.

to a few kilometers under constant structure parameters.

Finally the effect of Rytov variance on the correlation width is given in Figure 3.5, Figure 3.6 and Figure 3.7 for $L = 1$ km, $L = 3$ km and $L = 5$ km, respectively considering various wavelengths and aperture sizes where the weak turbulence region for plane waves is zoomed for ease of observation. Notice that as the link distance increases the significance of the aperture size decreases.

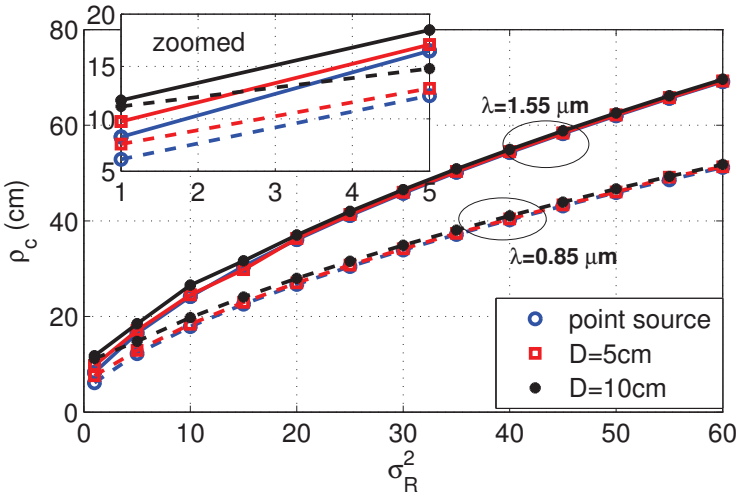

(a)

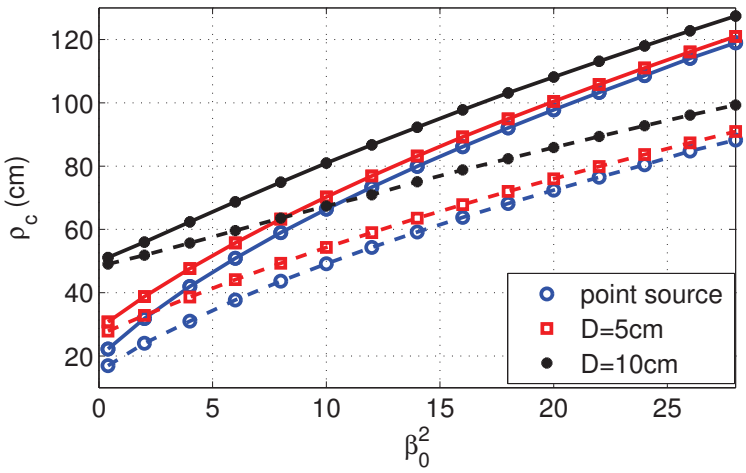

(b)

Figure 3.6. Correlation width ρ_c vs. Rytov variance for a link distance of $L = 3$ km (a) for plane waves and (b) for spherical waves. Dashed and solid curves are for $\lambda = 0.85\ \mu$m and $\lambda = 1.55\ \mu$m, respectively.

Correlation among the transmitted beams in multiple input single/multiple output FSO systems constitutes a key factor in determining the system performance. Although the correlation width obtained by the extended Rytov method is also used to determine the minimum transmitter separation in some studies in the FSO literature, alternatively there exist other studies such as [73] that deals with the transmitter separation problem numerically. In [73] it is shown that spatial correlation among the constituent beams of a MISO system depends on the link distance, receiver aperture

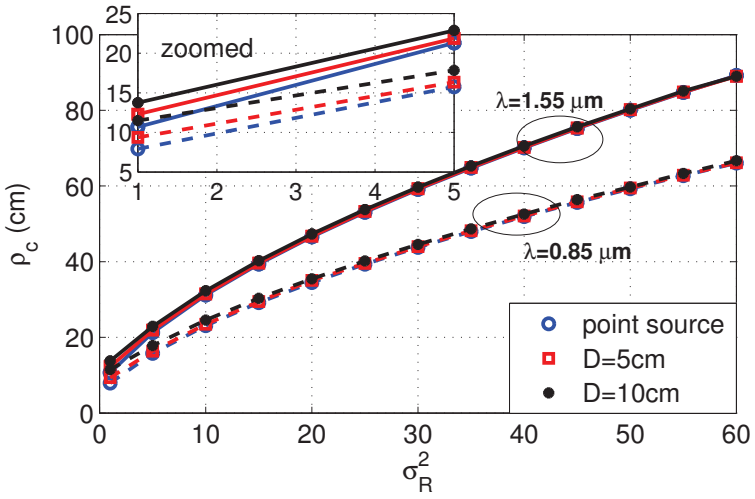

(a)

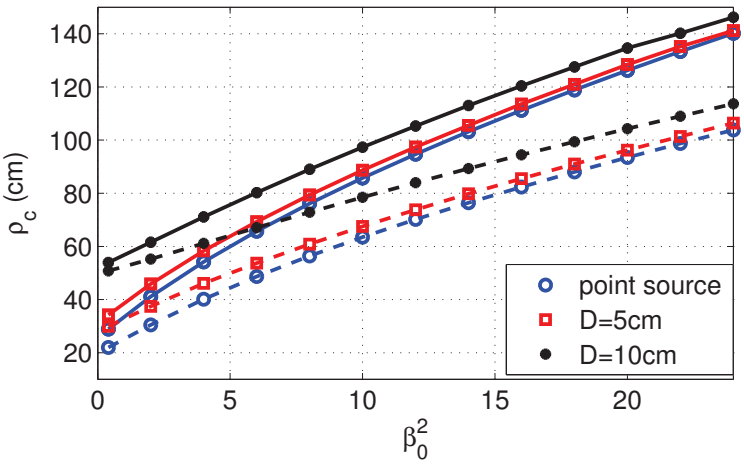

(b)

Figure 3.7. Correlation width ρ_c vs. Rytov variance for a link distance of $L = 5$ km (a) for plane waves and (b) for spherical waves. Dashed and solid curves are for $\lambda = 0.85\ \mu$m and $\lambda = 1.55\ \mu$m, respectively.

size, beam spacing and turbulence strength, where the turbulence strength has less impact than the other three. It is verified that spatial correlation is proportional to the link distance and receiver aperture size, and inversely proportional to the beam spacing.

The numerical analysis of [73] is based on a 4×1 system where correlation coefficient vs. beam separation or receiver aperture size curves are obtained through

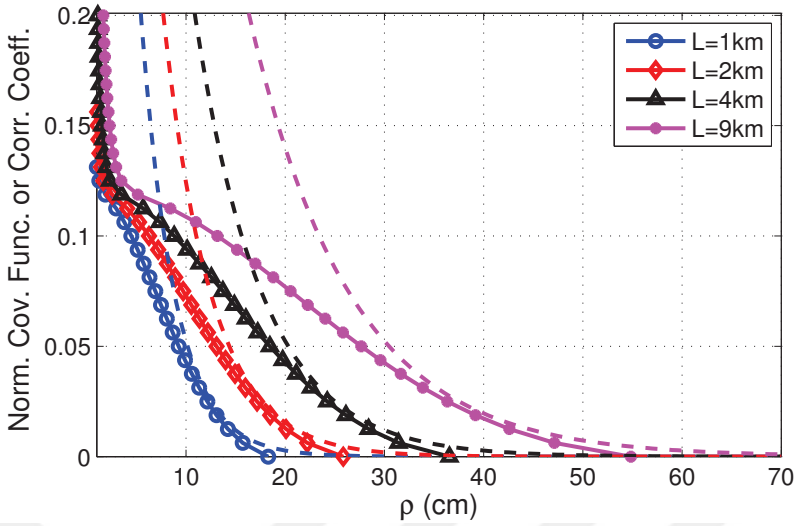

Figure 3.8. Comparison of theoretical and numerical approach for a fixed Rytov variance of $\sigma_R^2 = 16$ and for various link distances. Solid curves with markers show the theoretical results whereas dashed curves denote the curve fitting values from numerical results.

simulations for certain set of parameters. At least 15000 channel samples for each set of the used parameters are generated to have a value of correlation coefficient with a significance of at least 0.95. For all sets $\lambda = 1.55\ \mu$m, l_0 is 0.5 cm and L_0 is 10 m.

It is shown that for a specific Rytov variance, correlation at beam separation d_0 and propagation distance z_0 is equal to the correlation at beam separation $d = d_0\sqrt{z/z_0}$ and propagation distance z as long as average power is held constant by increasing receive aperture size for longer distances. An exponential is fit to the simulation data to approximate correlation coefficient with

$$r = \exp\left(\frac{-Cd}{\sqrt{z/z_0}}\right) \tag{3.10}$$

where $C = 0.295$ is a constant that minimizes the mean square error and $z_0 = 1$ km.

Notice that the numerical results of [73] are obtained assuming a strong turbulence and with a Rytov variance of $\sigma_R^2 = 16$. To compare these results with those

Table 3.1. Correlation widths for plane waves under various system configurations

			ρ_c(cm)		
L(km)	$\lambda(\mu$m)	σ_R^2	point source	$D = 5$ cm	$D = 10$ cm
1	0.85	0.02	2.97	4.71	8.66
		1.20	3.73	5.61	9.10
		2.80	5.27	6.75	9.84
	1.55	0.01	4.01	5.05	8.87
		0.59	4.32	5.82	9.25
		1.39	5.29	6.87	9.85
2	0.85	0.07	4.19	5.18	8.95
		4.29	9.20	10.09	12.41
		10.01	14.62	15.20	16.82
	1.55	0.04	5.67	6.28	9.34
		2.13	8.85	10.07	12.23
		4.97	13.42	14.05	15.80
3	0.85	0.15	5.15	5.71	9.30
		9.02	16.88	17.39	18.82
		21.05	27.52	27.82	28.74
	1.55	0.07	6.89	6.60	9.82
		4.48	15.55	16.09	17.65
		10.44	24.77	25.11	26.12
4	0.85	0.25	6.01	6.38	9.73
		15.29	26.37	26.69	27.64
		35.67	43.38	43.39	44.15
	1.55	0.13	8.03	7.38	10.34
		7.59	23.89	24.24	25.30
		17.70	38.78	38.98	39.64

			ρ_c(cm)		
L(km)	$\lambda(\mu$m)	σ_R^2	point source	$D = 5$ cm	$D = 10$ cm
5	0.85	0.38	6.82	7.08	10.28
		23.02	37.44	37.66	38.34
		53.70	61.84	61.96	62.33
	1.55	0.19	8.99	8.18	10.92
		11.42	33.65	33.90	34.65
		26.64	55.11	55.24	55.71

of the theoretical derivations based on the Rytov theory, we also set the same variance $\sigma_R^2 = 16$ and compute the correlation widths for various link distances as shown in Figure 3.8 assuming point sources (in this case point transmitters). The dashed curves are from curve fitting equation of (3.10) and the solid curves are according to the solution of (3.7). Although the simulation values obtained for correlation coefficient in [73] fall down to at most 0.01 level and that is why it is not appropriate to compare the theoretical results with the curve fitting values at 0 level, nevertheless the figure is helpful to observe that the theoretic and numerical results are compatible.

In conclusion it is seen that the theoretical calculations are in accordance with the simulation results of the numerical approach of [73] in terms of determining the correlation widths and therefore aperture separations for obtaining - nearly - uncorrelated paths.

3.4. Design Guidelines for Resolvable Channels

Using the results of Sections 3.2 and 3.3 we provide correlation widths, i.e. minimum aperture separations for resolvable paths, for various wavelengths ($\lambda \in \{0.85, 1.55\}\mu$m), link distances ($L \in \{1, 2, 3, 4, 5\}$ km) and aperture diameters ($D \in \{\sim 0, 5, 10\}$cm) for plane waves in Table 3.1 and for spherical waves in Table 3.2. Notice that each row of the σ_R^2/β_0^2 columns of both tables have three Rytov variances. These

Table 3.2. Correlation widths for spherical waves under various system configurations

			ρ_c(cm)		
L(km)	$\lambda(\mu$m)	β_0^2	point source	$D = 5$ cm	$D = 10$ cm
1	0.85	0.008	8.94	24.62	47.13
		0.56	10.24	25.14	47.41
		1.12	11.53	25.77	47.75
	1.55	0.003	12.20	25.65	47.68
		0.28	12.84	26.08	48.13
		0.56	13.69	27.00	48.88
2	0.85	0.02	12.76	26.56	47.84
		2.00	19.27	29.96	50.05
		4.00	25.39	34.27	52.67
	1.55	0.014	17.13	27.56	49.02
		0.99	21.41	30.91	50.81
		1.99	25.95	34.43	53.00
3	0.85	0.06	15.63	27.00	48.61
		4.21	31.81	39.22	56.10
		8.42	44.86	50.42	64.41
	1.55	0.03	21.05	29.14	50.24
		2.09	32.34	39.01	56.28
		4.18	42.81	48.41	63.00
4	0.85	0.10	18.22	28.13	49.36
		7.13	47.51	52.80	66.24
		14.27	69.07	72.81	83.15
	1.55	0.05	24.39	30.52	51.42
		3.54	45.92	50.93	65.00
		7.08	63.91	67.79	78.82

			ρ_c(cm)		
L(km)	$\lambda(\mu$m)	β_0^2	point source	$D = 5$ cm	$D = 10$ cm
5	0.85	0.15	20.63	29.25	50.19
		10.74	66.00	69.88	80.54
		21.48	97.40	100.07	107.81
	1.55	0.076	27.40	31.80	53.00
		5.32	61.98	65.79	77.22
		10.66	88.75	91.56	100.03

values correspond to the structure parameters of $C_n^2 = 5 \times 10^{-16}$, $C_n^2 = 3.5 \times 10^{-14}$ and $C_n^2 = 7 \times 10^{-14}$ m$^{-2/3}$, respectively. As seen from both tables, the required separations are at most a few tens of centimeters in most practical system configurations and link distances. Only, in the case of large link distances and/or aperture diameters the minimum separations reach up to a meter.

3.5. Conclusion

For MIMO FSO studies it is customary to assume uncorrelated paths among the transmitters and receivers. To ensure this the elements of the transmit and receive arrays should be placed sufficiently apart. In this chapter we discussed the methods to determine the inter-transmitter and inter-receiver separations rendering the independent channel statistics assumption valid. Using the theoretical approach based on the Rytov theory we evaluated the required separations at both transmit and receive sides. From another point of view we presented methods to determine how much channel correlation would be expected for a specific system configuration.

4. OPTICAL SPATIAL MODULATION OVER ATMOSPHERIC TURBULENCE CHANNELS

As mentioned in Chapter 1 the use multiple transmitters and/or receivers (i.e., diversity techniques) has been among the most effective ways of mitigating the effects of atmospheric turbulence [17–27]. Because the bandwidth is assumed to be practically unlimited, the spectral efficiency has not been a major design consideration. As a result, MIMO FSO systems are traditionally implemented with RC or space-time coding on the transmit side and diversity combining or aperture averaging features on the receiver side so as to combat scintillation effects. Furthermore, multiple transmitter/receiver use prevents the possible blockage of the beam and make it possible to cover longer distances. However, recently there has been a surge of interest in FSO systems which are also spectrally efficient. One approach to achieve higher spectral efficiency is to employ conventional pulse-based optical modulations with higher order constellations (such as PAM), however this brings higher PAPR and sensitivity to channel nonlinearities and noise as discussed in [1]. Since high PAPR values cause the transmitters to operate outside their linear region, large PAM constellations are not preferred. Recently, SIM as presented in [32, 80, 81] within single-input single-output (SISO) or MIMO architectures has emerged as another alternative. However, both the transmitter and receiver complexities of SIM systems are significantly higher than those of pulse-based optical communications. Another implementation difficulty of SIM systems is the requirement of adding a time-varying DC bias to prevent the transmitted signal from becoming negative. A final alternative is to use multiple transmit and receive apertures and employ spatial multiplexing methods with conventional modulation methods again as presented in [33] where a MIMO FSO transceiver is considered and different spatial multiplexing approaches are contrasted and compared with conventional MIMO FSO approaches. However, several drawbacks are also encountered in these systems such as ICI due to simultaneous transmissions, increased transceiver complexity to cancel/avoid ICI and large number of components to implement the MIMO transceivers.

In this context, we consider OSM as a feasible MIMO FSO communication method with high spectral efficiency and low hardware / implementation complexity. Notice that SM has been proposed in [34] as a novel MIMO transmission method where the information is conveyed simultaneously over both the signal and antenna spaces. In SM, part of the incoming bits is used to choose a transmit antenna to be activated while the rest is to select the modulation symbol to be sent. As shown extensively in the SM literature, this approach provides better multiplexing gains and error performances than conventional methods. Furthermore, because only one antenna is active during each signaling period, the transmit chain is simplified and the ICI is completely avoided. Remember that SSK [3] has also emerged as a special form of SM where only the transmitting antenna index is used to bear information.

SM/SSK based MIMO signaling has been considered for optical wireless communication before in [34–37] particularly for indoor visible light applications. Despite their advantages, existing optical SM/SSK systems have a few potential drawbacks. For instance, for optical SSK presented in [34, 35], every single bit increment in the spectral efficiency requires doubling the number of transmitters. In addition, introducing resilience against channel errors via coding automatically reduces the data rate. As an alternative, in [36] SM is implemented with PPM to provide performance and power gains but again by having the side effect of reduced spectral efficiency. Other schemes such as PAM in [37] would improve the spectral efficiency but at the cost of added power penalty. These observations signify the need to jointly use multiple modulations and for this reason, the first contribution of this dissertation is a novel OSM system, denoted by SPPAM, that combines the SSK principle with pulse amplitude and position modulations. Here, PAM is used to achieve a high spectral efficiency whereas PPM provides a power gain. This hybrid use of two different modulations having counteracting effects allow a flexible design according to the data rate and error performance requirements. Furthermore, by appropriately choosing the design parameters, the general formulation of SPPAM becomes applicable for implementations with only PAM, only PPM or even SSK, making a single framework valid for a wide range of scenarios.

In addition, the aforementioned optical SM/SSK works in [34–37] consider only indoor optical communication scenarios. As a consequence, the analysis and simulation results are provided only for deterministic channel models. On the other hand, we consider the proposed OSM scheme for FSO communications over atmospheric turbulence channels. In general, statistical models such as log-normal [11] and Gamma-Gamma [15] distributions are in good agreement with the experimental measurements for weak-to-moderate and moderate-to-strong atmospheric turbulence effects, respectively, as mentioned Chapter 1. That is why, we provide a theoretical error performance analysis for SPPAM and present a general ABEP upper bounding framework over both log-normal and Gamma-Gamma random fading environments. The theoretical error analysis is first presented for the uncoded systems and then also extended to their coded counterparts with convolutional encoding and maximum likelihood (ML) decoding assumptions. All theoretical derivations are validated by extensive simulations which indicate that the ABEP upper bounds are in good agreement with the simulated performances for both uncoded and coded systems. Finally, the theoretical upper bounding framework is also used to justify the robustness of the SPPAM performance against channel scintillation effects in both log-normal and Gamma-Gamma fading.

The rest of the chapter is organized as follows: In Section 4.1, optical SPPAM system and the received signal model is presented. In Section 4.2, the general ABEP upper bounding framework is described together with the ABEP analysis over weak-to-moderate and moderate-to-strong turbulence channels in subsections 4.2.2 and 4.2.3, respectively. Coded SPPAM analysis is given in Section 4.3. Simulation results are presented in Section 4.4 before the conclusive remarks in Section 4.5.

4.1. System Model

We consider an $N_t \times N_r$ MIMO FSO system employing SPPAM as shown in Figure 4.1 where N_t and N_r are the number of transmitters and receivers, respectively. The SPPAM system consists of PPAM and transmitter index mappers, a SPPAM modulator, transmitters (e.g. laser, LED), the atmospheric turbulence channel, receivers

(e.g. photodiode, photomultiplier), a joint optimum detector, and finally PPAM and transmitter index demappers, respectively. N_t is assumed to be an integer power of 2. At each time instant, the SPPAM modulator divides the incoming bit stream into blocks of $\log_2(N_t ML)$ bits where $\log_2(N_t)$, $\log_2(M)$ and $\log_2(L)$ bits are used to determine the indices of the active transmitter, the M-ary pulse position and the L-ary PAM amplitude to be transmitted at the designated pulse position, respectively. The transmitted signal belongs to an (L, M)-ary pulse position and amplitude modulation (PPAM) alphabet as presented in [82]. Due to the non-negativity constraint of the optical intensity channels, the zero amplitude is excluded from the constellation as in [83] so as to avoid the confusion between the cases of an active transmitter transmitting the "zero" signal and an inactive transmitter.

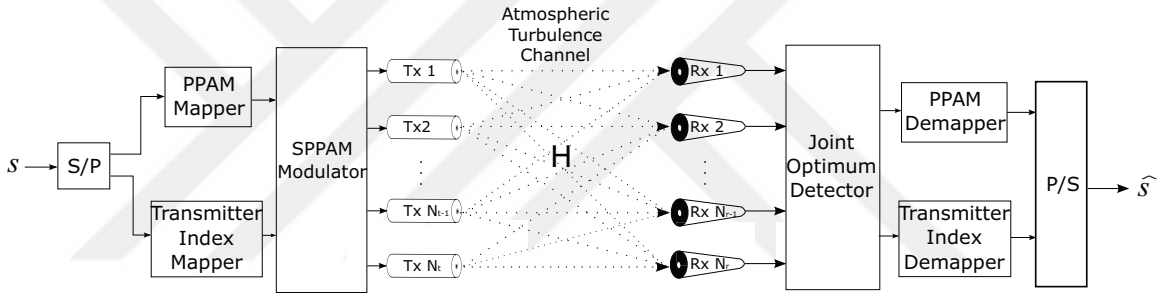

Figure 4.1. System model for SPPAM. Tx stands for transmitter and Rx stands for receiver. $\mathbf{s}$ and $\widehat{\mathbf{s}}$ are the input and estimated bitstreams, respectively.

$1 \times M$ dimensional PPAM signal vector $\mathbf{x}_{\ell m}$ is given by

$$\mathbf{x}_{\ell,m} = [\, 0 \cdots 0 \;\; A_\ell \;\; 0 \;\cdots\; 0 \,] \tag{4.1}$$

with the nonzero term being in the m-th position where $m = 1, \ldots, M$. A_ℓ denotes the ℓ-th pulse amplitude coming from the L-ary PAM constellation and each A_ℓ is described as $A_\ell = \ell\Delta$ with $\Delta = 2\sqrt{M}/(L+1)$ for $\ell = 1, \ldots, L$. A sample SPPAM index and symbol mapping is given in Table 4.1 for $N_t = 2$, $L = 2$ and $M = 2$.

The spectral efficiency of L-ary PAM is $r = \log_2 L$ b/s/Hz whereas that of M-ary PPM is $r = \log_2(M)/M$ b/s/Hz. In the latter, the denominator factor is due to

Table 4.1. A sample SM mapping for $N_t = 2$, $L = 2$ and $M = 2$

Input bit stream	Transmitter index	PPAM signal
0 0 0	1	$\Delta \begin{bmatrix} 0 & 1 \end{bmatrix}$
0 0 1	1	$\Delta \begin{bmatrix} 1 & 0 \end{bmatrix}$
0 1 0	1	$\Delta \begin{bmatrix} 0 & 2 \end{bmatrix}$
0 1 1	1	$\Delta \begin{bmatrix} 2 & 0 \end{bmatrix}$
1 0 0	2	$\Delta \begin{bmatrix} 0 & 1 \end{bmatrix}$
1 0 1	2	$\Delta \begin{bmatrix} 1 & 0 \end{bmatrix}$
1 1 0	2	$\Delta \begin{bmatrix} 0 & 2 \end{bmatrix}$
1 1 1	2	$\Delta \begin{bmatrix} 2 & 0 \end{bmatrix}$

the use of M time slots for PPM. Consequently SPPAM has a spectral efficiency of $r = \log_2(LMN_t)/M$ b/s/Hz, signifying that the use of multiple transmitters and L-ary PAM alleviates the spectral deficiency of PPM. This makes it possible to use a range of SPPAM modulation configurations according to the spectral efficiency or the error performance requirements of the system. Notice that the cases where $\{L = M = 1\}$, $\{L = 1, M > 1\}$ and $\{L > 1, M = 1\}$ correspond to SSK, spatial pulse position modulation (SPPM) and spatial pulse amplitude modulation (SPAM), respectively. Comparison of PAM, PPM, MUX, SSK and SPPAM in terms of their spectral efficiencies is given in Table 4.2. Based on Table 4.2 a sample selection with corresponding spectral efficiencies is shown in Table 4.3 for $N_t \in \{1, 2, 4, 8\}$, $L \in \{1, 2, 4, 8\}$, $M \in \{1, 2\}$ and $R \in \{1, 1/2, 2/3, 3/4\}$ where R is the code rate. As seen from the table, the spectral efficiency can be increased through either enlarging the PAM constellation size, increasing number of transmitters (utilizing SM) or both. Although PAM is capable of achieving high spectral efficiencies, increasing the alphabet size results in a higher number of different power levels, making the received signal sensitive to amplitude distortions - due to noise, interference and atmospheric conditions - [1] and having a large PAPR [84]. Therefore, allocation of some bits to the spatial domain in SPPAM also alleviates the alphabet size requirement on the PAM constellation.

Table 4.2. Spectral efficiency of modulation schemes

Modulation	Spectral efficiency (b/s/Hz)
L-PAM	$\log_2(L)$
M-PPM	$\log_2(M)/M$
L-PAM MUX	$N_t \log_2(L)$
M-PPM MUX	$N_t \log_2(M)/M$
N_t-SSK	$\log_2(N_t)$
(L, M)-SPPAM	$\log_2(LMN_t)/M$

The SPPAM signal vector is transmitted over the MIMO atmospheric turbulence channel that is described by the $N_r \times N_t$ dimensional channel matrix $\mathbf{H}$. The received noisy signal model is given by

$$\mathbf{Y} = P\mathbf{h}_{\mathrm{p}}\mathbf{x}_{\ell,\mathrm{m}} + \mathbf{N}$$

where $\mathbf{x}_{\ell,m}$ is the $1 \times M$ dimensional PPAM signal vector given in (4.1), $\mathbf{h}_p$ is the p-th column of the channel matrix $\mathbf{H}$ and P is the average emitted optical intensity. Here p and (ℓ, m) are the indices of the active transmitter and the transmitted PPAM symbol, respectively. $\mathbf{Y}$ is the $N_r \times M$ dimensional received signal matrix, $\mathbf{N}$ is the $N_r \times M$ dimensional noise matrix whose entries are described with independent and identically distributed (i.i.d.) additive white Gaussian variables, i.e., $n_{ij} = [N]_{ij} \sim \mathcal{N}(0, \sigma_n^2)$ and $\mathrm{E}[n_{ij}n_{uv}] = \sigma_n^2\delta_{ij,uv}$. Notice that ρ is defined as the electrical SNR on the transmitter side that is $\rho = P^2/\sigma_n^2$.

We assume that the elements of the channel matrix $\mathbf{H}$ represent i.i.d. channel fluctuations due to atmospheric turbulence. For the independence assumption to be valid, the transmitter-receiver paths need to be resolvable, i.e., each element in the transmit and receive arrays should be separated sufficiently or by at least the correlation width. The correlation width is dependent on factors such as the structure parameter, link distance, wavelength, wave type and turbulence regime, and can be

Table 4.3. Spectral efficiency of a sample selection of PAM, PPM, SSK, spatial multiplexing (MUX) and SPPAM

N_t	PAM index L	PPM index M	Modulation	Code Rate R	Spectral eff. r (b/s/Hz)
1	1	2	2-PPM	1	0.5
1	2	1	2-PAM	1	1
1	4	1	4-PAM	1/2	1
2	1	1	2-SSK	1	1
2	1	2	2-SPPM	1	1
2	2	1	2-SPAM	1/2	1
2	4	1	MUX 2-PPM	1	1
4	1	1	4-SSK	1/2	1
1	4	1	4-PAM	1	2
2	2	1	2-SPAM	1	2
2	4	1	4-SPAM	1/2	2
4	1	1	4-SSK	1	2
4	2	2	(2,2)-SPPAM	1	2
4	1	2	MUX 2-PPM	1	2
4	2	1	2-SPAM	2/3	2
1	8	1	8-PAM	1	3
3	2	1	MUX 2-PAM	1	3
2	4	1	4-SPAM	1	3
4	2	1	2-SPAM	1	3
4	2	1	MUX 2-PAM	3/4	3
8	1	1	8-SSK	1	3

computed by the extended Rytov model for wave propagation given in [6] as considered in Chapter 3. In this chapter, we consider a FSO system with wavelength of $\lambda = 1.55\ \mu$m, aperture diameter of $D = 2$ cm and link distance of $L = 2.5$ km considering spherical waves. The structure parameter C_n^2 is chosen as 1.4×10^{-14} and 7.4×10^{-14} m$^{-2/3}$ for weak and strong turbulence conditions, respectively. Under these circumstances the Rytov variances become 0.6 for weak turbulence and 3.16 for strong turbulence. Using the extended Rytov model of [6], the correlation widths or the required aperture separations for uncorrelated transmitter-receiver paths are computed as 9 cm and 12 cm for weak and strong turbulence conditions, respectively. That is to say, the proposed system model can be implemented with practical separations among the transmit and receive apertures.

At the receiver side the indices of the active transmitter and the PPAM symbol are determined by a joint ML detector and mapped back to the estimated bit stream. Assuming equally likely symbols, the joint optimum ML detection rule can be expressed for $p = 1, 2, \ldots, N_t$, $\ell = 1, 2, \ldots, L$, $m = 1, 2, \ldots, M$ as

$$(\widehat{p}, \widehat{\ell}, \widehat{m}) = \arg \min_{p,\ell,m} \|\mathbf{Y} - \mathbf{h}_p \mathbf{x}_{\ell,m} P\|^2$$

where $\widehat{p}$ and $(\widehat{\ell}, \widehat{m})$ are the estimated indices for active transmitter and transmitted PPAM symbol, respectively.

4.2. ABEP Analysis

We present here a theoretical ABEP analysis for log-normal and Gamma-Gamma distributed turbulence channels under the optimum ML decision rule given in the previous section. In general, deriving the exact ABEP for SM is computationally intractable but as shown in related SM works such as [85], a tight upper bound can

be expressed as

$$\begin{aligned} \text{ABEP} \;\leq\; & \frac{1}{2LMN_t} \sum_{p=1}^{N_t} \sum_{\widehat{p}=1}^{N_t} \sum_{\ell=1}^{L} \sum_{\widehat{\ell}=1}^{L} \sum_{m=1}^{M} \sum_{\widehat{m}=1}^{M} \\ & \text{APEP}(p, \ell, m, \widehat{p}, \widehat{\ell}, \widehat{m} | \mathbf{h}_p, \mathbf{h}_{\widehat{p}}, \mathbf{x}_{\ell,m}, \mathbf{x}_{\widehat{\ell},\widehat{m}}) \end{aligned} \tag{4.2}$$

where

$$\text{APEP}(p, \ell, m, \widehat{p}, \widehat{\ell}, \widehat{m} | \mathbf{h}_p, \mathbf{h}_{\widehat{p}}, \mathbf{x}_{\ell,m}, \mathbf{x}_{\widehat{\ell},\widehat{m}}) = \text{E}\left[\text{Q}\left(\frac{\sqrt{\rho S}}{2}\right)\right] \tag{4.3}$$

is the average conditional pairwise error probability (APEP) for deciding in favor of the index triplet $(\widehat{p}, \widehat{\ell}, \widehat{m})$ instead of (p, ℓ, m), ρ is the electrical SNR given by $\rho = P^2/\sigma_n^2$ as defined in Section 4.1 before and

$$S = ||\mathbf{h}_p \mathbf{x}_{\ell,m} - \mathbf{h}_{\widehat{p}} \mathbf{x}_{\widehat{\ell},\widehat{m}}||^2. \tag{4.4}$$

Notice that using Craig's formulation for Q-function [86] where

$$Q(x) = \frac{1}{\pi} \int_0^{\pi/2} \exp\left(-\frac{x^2}{2\sin^2\theta}\right) d\theta, \tag{4.5}$$

the APEP in (4.3) can be rewritten in terms of a single definite integral as

$$\text{APEP} \;=\; \frac{1}{\pi} \int_0^{\pi/2} M_S\left(-\frac{\rho}{8\sin^2\theta}\right) d\theta \tag{4.6}$$

where $M_S(t) = \int_0^\infty f_S(\Gamma) e^{\Gamma t} d\Gamma$ is the moment generating function (MGF) of the random variable S.

It is evident that the key to the computation of ABEP upper bound in (4.2) is to identify distinct error cases and to derive the corresponding APEP's as given in (4.3). Notice that there are LMN_t cases where both the active transmitter and also the transmitted PPAM symbol are correctly detected. All the other remaining cases correspond to an error event. However, a careful study of the PEP cases reveals that

there are only 4 distinct error events as summarized in the next subsection.

4.2.1. Error Types

As mentioned above in addition to LMN_t cases where all indices are detected correctly, there are 4 distinct error types which encompasses all error events as shown below:

- *Type-I error*: Neither the pulse positions nor the index of the active transmitter are correctly detected, i.e., $p \neq \widehat{p}, m \neq \widehat{m}$. This case corresponds to

$$\mathbf{h}_p\mathbf{x}_{l,m} - \mathbf{h}_{\widehat{p}}\mathbf{x}_{\widehat{\ell},\widehat{m}} = \begin{bmatrix} 0\cdots 0 & A_\ell h_{p1} & 0\cdots 0 & -A_{\widehat{\ell}} h_{\widehat{p}1} & 0\cdots 0 \\ 0\cdots 0 & A_\ell h_{p2} & 0\cdots 0 & -A_{\widehat{\ell}} h_{\widehat{p}2} & 0\cdots 0 \\ 0\cdots 0 & \vdots & 0\cdots 0 & \vdots & 0\cdots 0 \\ 0\cdots 0 & A_\ell h_{pN_r} & 0\cdots 0 & -A_{\widehat{\ell}} h_{\widehat{p}N_r} & 0\cdots 0 \end{bmatrix}$$

$$\uparrow \qquad\qquad \uparrow$$

$$\text{column } m \qquad\qquad \text{column } \widehat{m}$$

  which results in the error metric in (4.4) corresponding to type-I error, S_I, as

$$S_I = \sum_{r=1}^{N_r} \left(A_\ell^2 h_{pr}^2 + A_{\widehat{\ell}}^2 h_{\widehat{p}r}^2 \right) \tag{4.7}$$

  where there are $2N_r$ i.i.d. random variables coming from the channel fading terms. Notice that whether the pulse amplitudes are detected correctly or not does not affect the statistical description of S_I. So there are $L^2M(M-1)N_t(N_t-1)$ terms corresponding to type-I error in (4.2).
- *Type-II error*: The index of the transmitter and the pulse position are both correctly detected but the PAM symbol is not, i.e., $p = \widehat{p}, \ell \neq \widehat{\ell}, m = \widehat{m}$ and there are $L(L-1)MN_t$ terms corresponding to type II error. Notice that this

case corresponds to the $\mathbf{h}_p\mathbf{x}_{\ell,m} - \mathbf{h}_{\widehat{p}}\mathbf{x}_{\widehat{\ell},\widehat{m}}$ expression given as

$$\mathbf{h}_p\mathbf{x}_{\ell,m} - \mathbf{h}_{\widehat{p}}\mathbf{x}_{\widehat{\ell},\widehat{m}} = \begin{bmatrix} 0 & \cdots & 0 & (A_\ell - A_{\widehat{\ell}})h_{p1} & 0 & \cdots & 0 \\ 0 & \cdots & 0 & (A_\ell - A_{\widehat{\ell}})h_{p2} & 0 & \cdots & 0 \\ 0 & \cdots & 0 & \vdots & 0 & \cdots & 0 \\ 0 & \cdots & 0 & (A_\ell - A_{\widehat{\ell}})h_{pN_r} & 0 & \cdots & 0 \end{bmatrix}$$

$$\uparrow$$

$$\text{column } m = \widehat{m}$$

which results in the error metric in (4.4) corresponding to type-II error, S_{II}, as

$$S_{II} = \sum_{r=1}^{N_r} (A_\ell - A_{\widehat{\ell}})^2 h_{pr}^2 \tag{4.8}$$

where there are N_r i.i.d. random variables.

- *Type-III error*: The index of the transmitter is correctly detected but the pulse position is not, i.e., $p = \widehat{p}, m \neq \widehat{m}$. For this case

$$\mathbf{h}_p\mathbf{x}_{l,m} - \mathbf{h}_{\widehat{p}}\mathbf{x}_{\widehat{\ell},\widehat{m}}$$

$$= \begin{bmatrix} 0 \cdots & 0 & A_\ell h_{p1} & 0 & \cdots & 0 & -A_{\widehat{\ell}} h_{p1} & 0 & \cdots & 0 \\ 0 \cdots & 0 & A_\ell h_{p2} & 0 & \cdots & 0 & -A_{\widehat{\ell}} h_{p2} & 0 & \cdots & 0 \\ 0 \cdots & 0 & \vdots & 0 & \cdots & 0 & \vdots & 0 & \cdots & 0 \\ 0 \cdots & 0 & A_\ell h_{pN_r} & 0 & \cdots & 0 & -A_{\widehat{\ell}} h_{pN_r} & 0 & \cdots & 0 \end{bmatrix}$$

$$\uparrow \qquad\qquad\qquad \uparrow$$

$$\text{column } m \qquad\qquad \text{column } \widehat{m}$$

which results in the error metric in (4.4) corresponding to type-III error, S_{III}, as

$$S_{III} = \sum_{r=1}^{N_r} \left(A_\ell^2 + A_{\widehat{\ell}}^2\right) h_{pr}^2 \tag{4.9}$$

where there are N_r i.i.d. random variables. Similar to type-I error, whether the pulse amplitudes are detected correctly or not does not affect the statistical

description of S_{III}. That is why, in the summation of (4.2) there are $L^2M(M-1)N_t$ terms corresponding to type-III error.

- *Type-IV error*: The pulse position is correctly detected but the index of the transmitter is not, i.e., $p \neq \widehat{p}, m = \widehat{m}$. Again the pulse amplitude may or may not be detected correctly. There are $L^2MN_t(N_t-1)$ terms corresponding to type-IV error. This case has $\mathbf{h}_p\mathbf{x}_{\ell,m} - \mathbf{h}_{\widehat{p}}\mathbf{x}_{\widehat{\ell},\widehat{m}}$ given by

$$\mathbf{h}_p\mathbf{x}_{\ell,m} - \mathbf{h}_{\widehat{p}}\mathbf{x}_{\widehat{\ell},\widehat{m}} = \begin{bmatrix} 0 & \cdots 0 & A_\ell h_{p1} - A_{\widehat{\ell}} h_{\widehat{p}1} & 0 & \cdots 0 \\ 0 & \cdots 0 & A_\ell h_{p2} - A_{\widehat{\ell}} h_{\widehat{p}2} & 0 & \cdots 0 \\ 0 & \cdots 0 & \vdots & 0 & \cdots 0 \\ 0 & \cdots 0 & A_\ell h_{pN_r} - A_{\widehat{\ell}} h_{\widehat{p}N_r} & 0 & \cdots 0 \end{bmatrix}$$

$$\uparrow$$

$$\text{column } m = \widehat{m}$$

which results in the error metric in (4.4) corresponding to type-IV error, S_{IV}, as

$$S_{IV} = \sum_{r=1}^{N_r} (A_\ell h_{pr} - A_{\widehat{\ell}} h_{\widehat{p}r})^2. \tag{4.10}$$

where there are again N_r i.i.d. random variables.

As a result, the ABEP upper bound in (4.2) can be written in terms of 4 distinct APEP summations such that

$$\begin{aligned} \text{ABEP} \;\leq\; & \frac{(M-1)(N_t-1)}{2L} \sum_{\ell=1}^{L} \sum_{\widehat{\ell}=1}^{L} \text{APEP}_I(\ell,\hat{\ell}) + \frac{1}{2L} \sum_{\ell=1}^{L} \sum_{\widehat{\ell}=1,\widehat{\ell}\neq\ell}^{L} \text{APEP}_{II}(\ell,\hat{\ell}) \\ + \;& \frac{M-1}{2L} \sum_{\ell=1}^{L} \sum_{\widehat{\ell}=1}^{L} \text{APEP}_{III}(\ell,\hat{\ell}) + \frac{N_t-1}{2L} \sum_{\ell=1}^{L} \sum_{\widehat{\ell}=1}^{L} \text{APEP}_{IV}(\ell,\hat{\ell}) \end{aligned} \tag{4.11}$$

where APEP_i's are the APEPs corresponding to type $i \in \{I, II, III, IV\}$ errors respectively. Therefore the number of terms to be calculated to evaluate the ABEP reduces from $LMN_t(LMN_t-1)$ to only $4L^2 - L$. For example for a $N_t = 4$, $L = 4$ and $M = 4$ system 60 terms are calculated instead of 4032. Even further simplifica-

tion is possible in the special cases. For instance, for $M = 1$ the bound given in (4.11) corresponds to SSK or SPAM, where there is no type-I and III errors while for $L = 1$ it corresponds to SPPM or SSK where there is no type-II error.

4.2.2. APEP Analysis Under Weak-to-Moderate Turbulence

Under weak-to-moderate turbulence conditions type-I, II and III errors require the distribution of weighted sum of squared log-normal random variables. If X_i are i.i.d. normal random variables with $\sim \mathcal{N}(\mu_X, \sigma_X^2)$, then $h_i = e^{X_i}$ are log-normal random variables with parameters (μ_X, σ_X^2).

Considering (4.7), (4.8) and (4.9) for type-I, II and III errors, respectively, S can be expressed as $S = \sum_{i=1}^{N} c_i h_i^2$ where c_i are constants and N is the number of i.i.d. random variables. Following [87] mean μ_S and variance σ_S^2 of S can be expressed as

$$\begin{aligned} \mu_S &= N_r \exp(2\mu_X + 2\sigma_X^2)(c_1 + c_2), \\ \sigma_S^2 &= N_r(\exp(4\sigma_X^2) - 1)\exp(4\mu_X + 4\sigma_X^2)(c_1^2 + c_2^2), \end{aligned}$$

for type-I error where $c_1 = A_\ell^2$ and $c_2 = A_{\widehat{\ell}}^2$, and as

$$\begin{aligned} \mu_S &= N_r \exp(2\mu_X + 2\sigma_X^2)c, \\ \sigma_S^2 &= N_r(\exp(4\sigma_X^2) - 1)\exp(4\mu_X + 4\sigma_X^2)c^2 \end{aligned}$$

for both type-II and III errors where $c = (A_\ell - A_{\widehat{\ell}})^2$ for type-II error and $c = A_l^2 + A_{\widehat{\ell}}^2$ for type-III error.

Although closed form expressions for the log-normal sum PDF are not available, as shown in [88] the weighted sum of log-normal random variables, whether correlated or uncorrelated, can be approximated by a single log-normal random variable $S \approx e^U$ where U is normal with $\sim \mathcal{N}(\mu_U, \sigma_U^2)$. Therefore S is approximately a lognormal

random variable with the PDF given by

$$f_S(s) = \frac{1}{\sqrt{2\pi}\sigma_U s} \exp\left(-\frac{(\log s - \mu_U)^2}{2\sigma_U^2}\right) \tag{4.12}$$

with its mean and variance given as $\mu_U = \log\left(\mu_S/\sqrt{1+\frac{\sigma_S^2}{\mu_S^2}}\right)$ and $\sigma_U^2 = \log\left(1+\frac{\sigma_S^2}{\mu_S^2}\right)$, respectively. As a result the approximate MGF of the sum of log-normal random variables can be written as

$$M_S(t) = \int_0^\infty \exp(ts)\frac{1}{s\sigma\sqrt{2\pi}} \exp\left(-\frac{(\log s - \mu_S)^2}{2\sigma_U^2}\right). \tag{4.13}$$

Notice that even though (4.13) does not have a closed form expression, it can be tightly approximated by the Gauss-Hermite expansion as in ([88], eq 9) for independent random variables such that

$$M_S(t) \approx \sum_{n=1}^{N_{GH}} \frac{w_n}{\sqrt{\pi}} \exp\left[t \exp\left(\sqrt{2}\sigma_U a_n + \mu_U\right)\right] \tag{4.14}$$

where w_n and a_n are weight and abscissa factors for Gauss-Hermite integration, respectively and N_{GH} is the number of terms used in the expansion. Finally, using (4.14) in equation (4.6), the ABEP expressions corresponding to type-I, II and III errors can be written as

$$\text{APEP}_{\text{I,II,III}} \approx \sum_{n=1}^{N_{GH}} \frac{w_n}{\sqrt{\pi}} Q\left(\sqrt{\frac{\rho}{4} e^{\sqrt{2}\sigma_U a_n + \mu_U}}\right). \tag{4.15}$$

Contrary to type-I, II, and III errors, type-IV error comprises of the sum of N_r square terms each of which appears as the weighted difference of two log-normal random variables. Even though linear combinations of log-normals (log-normal squares) can be described by an approximate log-normal distribution, a closed forms distribution does not exist for the weighted difference of log-normals. As a result direct computation of the APEP corresponding to type IV error is not possible. Instead, the probability distribution for this error event is approximated numerically using the kernel density

estimation (KDE) method of [89] such that

$$\widehat{f}_S(s) = \frac{1}{N}\sum_{i=1}^{N}\frac{1}{b}K\left(\frac{s-S_i}{b}\right) \tag{4.16}$$

where S is the random variable, K is the known kernel function, b is the bandwidth controlling the degree of smoothing, S_i are the samples of S and N is the number of available samples. The MGF of S can be approximated in terms of the MGF of kernel density as $\widehat{M}_S(t) \approx \frac{1}{n}\sum_{i=1}^{N} M_{K_i}(t)$ where K_i are the random variables with the given kernel as their density such that $K_i(s) = \frac{1}{b}K\left(\frac{s-S_i}{b}\right)$ and $M_{K_i}(t)$ is the MGFs of K_i for $i = 1, \ldots, N$. As a result, (4.6) for type-IV error can be expressed as

$$\text{APEP}_{\text{IV}} \approx \sum_{i=1}^{N}\frac{1}{\pi}\int_0^{\pi/2} M_{K_i}\left(-\frac{\rho}{8\sin^2\theta}\right)d\theta. \tag{4.17}$$

Finally, APEP_i terms for $i = I, \ldots, IV$ in (4.15) and (4.17) are placed in equation (4.11) to compute the ABEP upper bound.

4.2.3. APEP Analysis Under Moderate-to-Strong Turbulence

Under moderate-to-strong turbulence conditions type-I, II and III errors require the distribution of sum of squared Gamma-Gamma random variables. As in the log-normal distribution case we express the S variable as $S = \sum_{i=1}^{N} c_i h_i^2$, where h_i are Gamma-Gamma variables and c_i are constants. A Gamma-Gamma variable is derived from the product of two independent Gamma variables [90]. Suppose X_1, X_2 are Gamma distributed random variables with PDF

$$f_{X_i}(x_i) = \frac{1}{n_i^{m_i}\Gamma(m_i)}x_i^{m_i-1}\exp\left(-\frac{x_i}{n_i}\right),\ i = 1, 2$$

and parameters $(m_{X_1} = \alpha, n_{X_1} = 1/\alpha)$ and $(m_{X_2} = \beta, n_{X_2} = 1/\beta)$, respectively. $h_i = X_1X_2$ is a Gamma-Gamma variable with PDF given in (2.2).

Using the MGF of the squared Gamma-Gamma random variable given in [91], MGF of $Y_i = h_i^2$ is written as

$$M_{Y_i}(t) = \frac{\sqrt{\alpha\beta}^{\alpha+\beta} t^{-\frac{\alpha+\beta}{4}}}{4\pi\Gamma(\alpha)\Gamma(\beta)} \times \mathrm{G}_{1,4}^{4,1}\left[\frac{(\alpha\beta)^2}{16t}\middle|\begin{matrix}1-\frac{\alpha+\beta}{4}\\ \frac{\alpha-\beta}{4}, \frac{\alpha-\beta+2}{4}, \frac{-\alpha+\beta}{4}, \frac{-\alpha+\beta+2}{4}\end{matrix}\right]$$

where $G[\cdot]$ denotes the Meijer's G function given as

$$\mathrm{G}_{p,q}^{m,n}\left[z\middle|\begin{matrix}a_1, a_2, \cdots, a_p\\ b_1, b_2, \cdots, b_q\end{matrix}\right] = \frac{1}{2\pi j}\int \frac{\prod_{k=1}^{m}\Gamma(b_k - s)\prod_{k=1}^{n}\Gamma(1-a_k+s)}{\prod_{k=m+1}^{q}\Gamma(1-b_k+s)\prod_{k=n+1}^{p}\Gamma(a_k-s)} z^s ds$$

with j being $j = \sqrt{-1}$.

The MGF of sum of N independent scaled random variables can be expressed as

$$M_S(t) = \prod_{i=1}^{N} M_{c_i Y_i}(t) = \prod_{i=1}^{N} M_{Y_i}(c_i t)$$

where c_i are constants. Following the steps of MGF analysis for the log-normal distribution, the integral in (4.6) becomes for type-I error

$$\begin{aligned}\mathrm{APEP_I} = \frac{1}{\pi}\int_0^{\pi/2}\prod_{i=1}^{2}\Bigg(&\frac{\sqrt{\alpha\beta}^{\alpha+\beta}\left(\frac{\rho}{8\sin^2\theta}\right)^{-\frac{\alpha+\beta}{4}}}{4\pi\Gamma(\alpha)\Gamma(\beta)} \times \\ &\mathrm{G}_{1,4}^{4,1}\left[\frac{(\alpha\beta\sin\theta)^2}{2c_i^2\rho}\middle|\begin{matrix}1-\frac{\alpha+\beta}{4}\\ \frac{\alpha-\beta}{4}, \frac{\alpha-\beta+2}{4}, \frac{-\alpha+\beta}{4}, \frac{-\alpha+\beta+2}{4}\end{matrix}\right]\Bigg)^{N_r} d\theta, \end{aligned} \tag{4.18}$$

where $c_1 = A_l^2$ and $c_2 = A_{\widehat{l}}^2$. For type-II and III errors the ABEP expressions can be written as

$$\begin{aligned}\mathrm{APEP_{II,III}} = \frac{1}{\pi}\int_0^{\pi/2}\Bigg(&\frac{\sqrt{\alpha\beta}^{\alpha+\beta}\left(\frac{\rho}{8\sin^2\theta}\right)^{-\frac{\alpha+\beta}{4}}}{4\pi\Gamma(\alpha)\Gamma(\beta)} \times \\ &\mathrm{G}_{1,4}^{4,1}\left[\frac{(\alpha\beta\sin\theta)^2}{2c^2\rho}\middle|\begin{matrix}1-\frac{\alpha+\beta}{4}\\ \frac{\alpha-\beta}{4}, \frac{\alpha-\beta+2}{4}, \frac{-\alpha+\beta}{4}, \frac{-\alpha+\beta+2}{4}\end{matrix}\right]\Bigg)^{N_r} d\theta, \end{aligned} \tag{4.19}$$

where $c = (A_l - A_{\widehat{l}})^2$ for type-II error and $c = A_l^2 + A_{\widehat{l}}^2$ for type-III error.

As in the case of log-normal distribution, a closed form distribution for the difference of two Gamma-Gamma random variables does not exist. For this reason an approximate distribution and the APEP bound corresponding to type-IV error is numerically calculated by KDE as in equation (4.17). Then APEP_i terms for $i = I, \ldots, IV$ are placed in equation (4.11) to compute the ABEP upper bound.

4.3. ABEP Bound with Coded SPPAM

The performance of the uncoded SPPAM system can be further improved by a convolutional encoder/decoder pair as shown in Figure 4.2. Here, input bitstream $\mathbf{u}$ is first encoded by a convolutional encoder. Encoded bitstream $\mathbf{c}$ is then interleaved by a random block interleaver whose output, $\mathbf{s}$, is the input to the SPPAM modulator. At the receiver side, the output of the SPPAM demodulator $\widehat{\mathbf{s}}$ is deinterleaved into $\widehat{\mathbf{c}}$ that is decoded to obtain the estimated information bits.

The error upper bound for the coded SPPAM system (ABEP^{C}) assuming perfect interleaving is given by [92]

$$\text{ABEP}^{\text{C}} \leq \sum_{d=d_{free}}^{\infty} \frac{1}{k} B_d P_d \tag{4.20}$$

where d is the Hamming distance, d_{free} is the minimum free distance of the rate k/n convolutional code, B_d is the weighting coefficients. P_d is expressed as

$$P_d = \begin{cases} \sum\limits_{e=\frac{d+1}{2}}^{d} \binom{d}{e} p^e (1-p)^{d-e}, & d \text{ odd} \\ \frac{1}{2}\binom{d}{d/2} p^{d/2}(1-p)^{d/2} + \sum\limits_{e=\frac{d}{2}+1}^{d} \binom{d}{e} p^e (1-p)^{d-e}, & d \text{ even} \end{cases} \tag{4.21}$$

where p is binary symmetric channel (BSC) transition probability which is the ABEP given in (4.11) for the uncoded system.

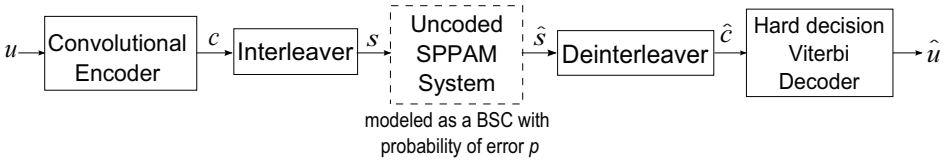

Figure 4.2. System model for coded SPPAM

4.4. Simulation Results

We present the simulation results on the error performance of SPPAM over FSO channels for various configurations. As mentioned in Section 4.1, the FSO system is simulated with a wavelength of $\lambda = 1.55\ \mu$m, a link distance of $L = 2.5$ km and a receive aperture diameter of $D = 2$ cm, unless otherwise is stated, considering spherical waves. The structure parameter C_n^2 is chosen as 1.4×10^{-14} and 7.4×10^{-14} m$^{-2/3}$ for weak and strong turbulence conditions, respectively. These values correspond to $\sigma_I^2 = 0.5$ and spherical Rytov variance of 0.6 for weak turbulence, and $\sigma_I^2 = 1.09$ with $\alpha = 2.1$, $\beta = 2.4$ and spherical Rytov variance of 3.16 for strong turbulence. Assuming the inter-transmitter and inter-receiver separations are at least the correlation length, which is 9 cm for weak and 12 cm for strong turbulence conditions, we consider all the transmitter-receiver paths are distinct. The mean emitted power is the same for all scenarios to ensure comparability. For this reason BER performance results are evaluated with regard to transmit power against noise power with the electrical SNR defined as $\rho = P^2/\sigma_n^2$.

Using the error analysis framework in Sections 4.2 and 4.3 the ABEP upper bounds expressed in equations (4.2) and (4.20) for the uncoded and coded SPPAM systems, respectively, are derived and compared with the corresponding simulated performances. All simulation and analysis curves for SPPAM are obtained using $N_r = 4$ receivers, unless otherwise is stated. The ABEP bounds are obtained for different values of PAM symbol index set size $L \in \{1, 2, 4\}$, PPM alphabet size $M \in \{1, 2, 4\}$, coding rate $R \in \{1, 1/2, 2/3, 3/4\}$ and number of transmitters $N_t \in \{2, 4, 8\}$. In both theoretical derivations and simulated performances, Gray mapping is assumed

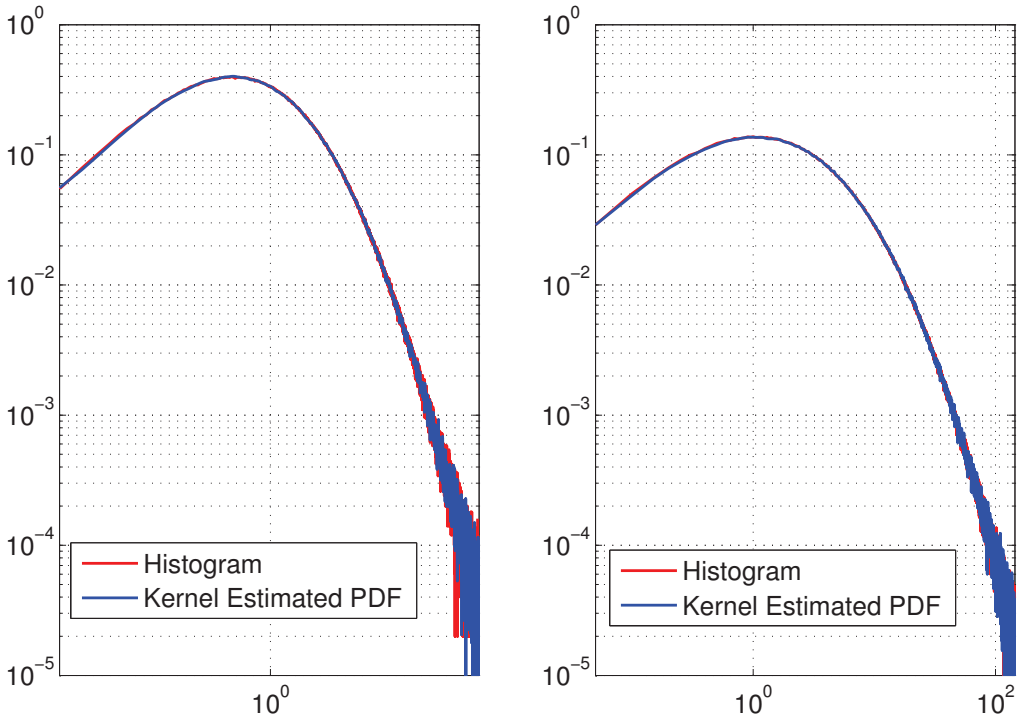

(a) (b)

Figure 4.3. Accuracy of Kernel density estimates for (a) log-normal and (b) Gamma-Gamma distributions.

for bit to symbol mappings. For weak-to-moderate turbulence condition $N_{GH} = 20$ variables are used for Gauss-Hermite integration. For coded SPPAM, the rate 1/2 convolutional code with generator $(5, 7)_8$ in octal representation is employed. The 2/3 and 3/4 codes are generated from the rate 1/2 code via puncturing using the puncturing matrices given in [93]. The code rates, puncturing patterns, d_{free}, d and B_d values are summarized in Table 4.4.

In log-normal fading channels the ABEP bounds corresponding to type I-III errors can be computed using the MGF and approximate Gauss-Hermite expansion approaches in equations (4.13)-(4.15). In the case of Gamma-Gamma fading, the ABEP upper bounds can be computed using (4.18) and (4.19) for type I and type II/III errors, respectively. In both channel cases, for the type-IV error, a Gaussian kernel is used to estimate the distribution for the variable in (4.10) and to evaluate

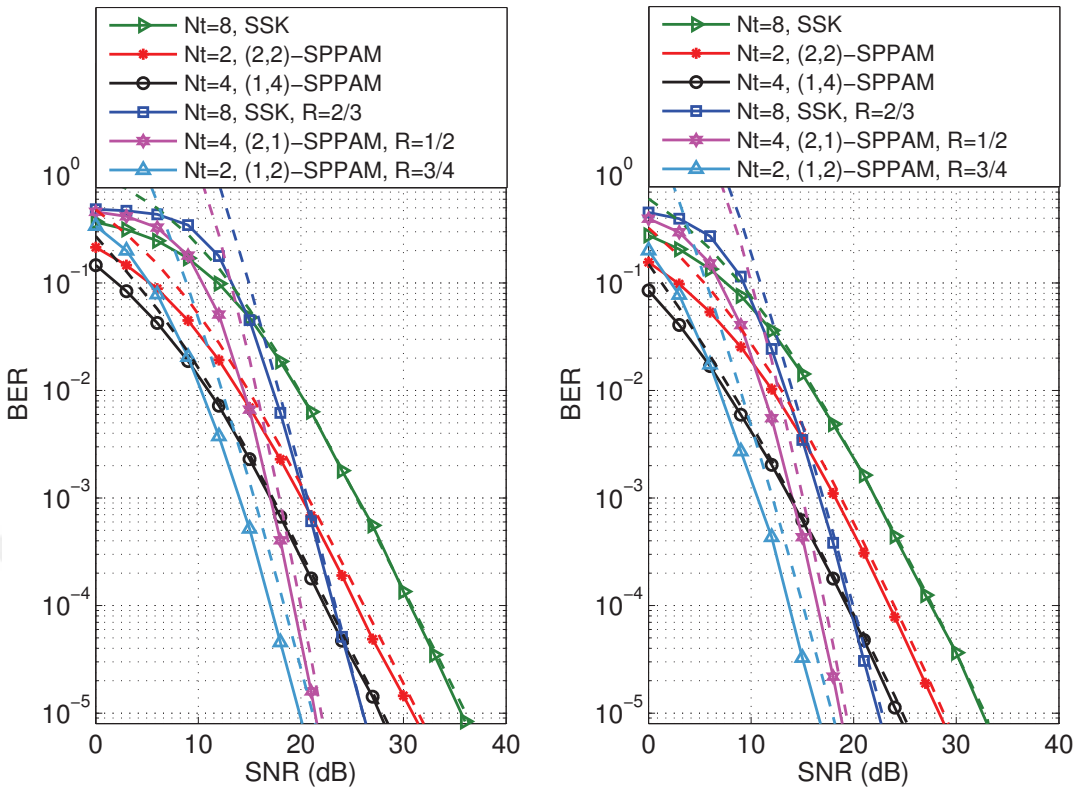

Figure 4.4. Performance results and theoretical upper bounds for the uncoded and coded SPPAM systems under (a) log-normal fading with $\sigma_I^2 = 0.5$ and (b) Gamma-Gamma fading with $\sigma_I^2 = 1.09$.

the ABEP bound using (4.17) with $M_{K_i}(t) = \exp\left(\mu_i t + \frac{1}{2}b^2t^2\right)$ where μ_i are the mean of the Gaussian distributed variables. For the simulations a kernel size of $N = 2 \times 10^6$ samples is used with a kernel estimator bandwidth b of 1/5000.

Figure 4.3 shows the sample KDE results of S for type-IV error given in (4.10) for the log-normal and Gamma-Gamma distributions for $N_t = 2$, $L = 1$ and $M = 2$. The dashed curves show PDF obtained from the histogram of 1×10^6 randomly generated samples of S and the solid curves denote the kernel estimated density of again 1×10^6 random samples. As seen in the figure, the estimated PDF's formed by KDE provide good approximations to the true PDF's for both log-normal and Gamma-Gamma distributions. That is why, the approximate composite PDF obtained using the KDE approach can be used in the theoretical error analysis to evaluate the ABEP

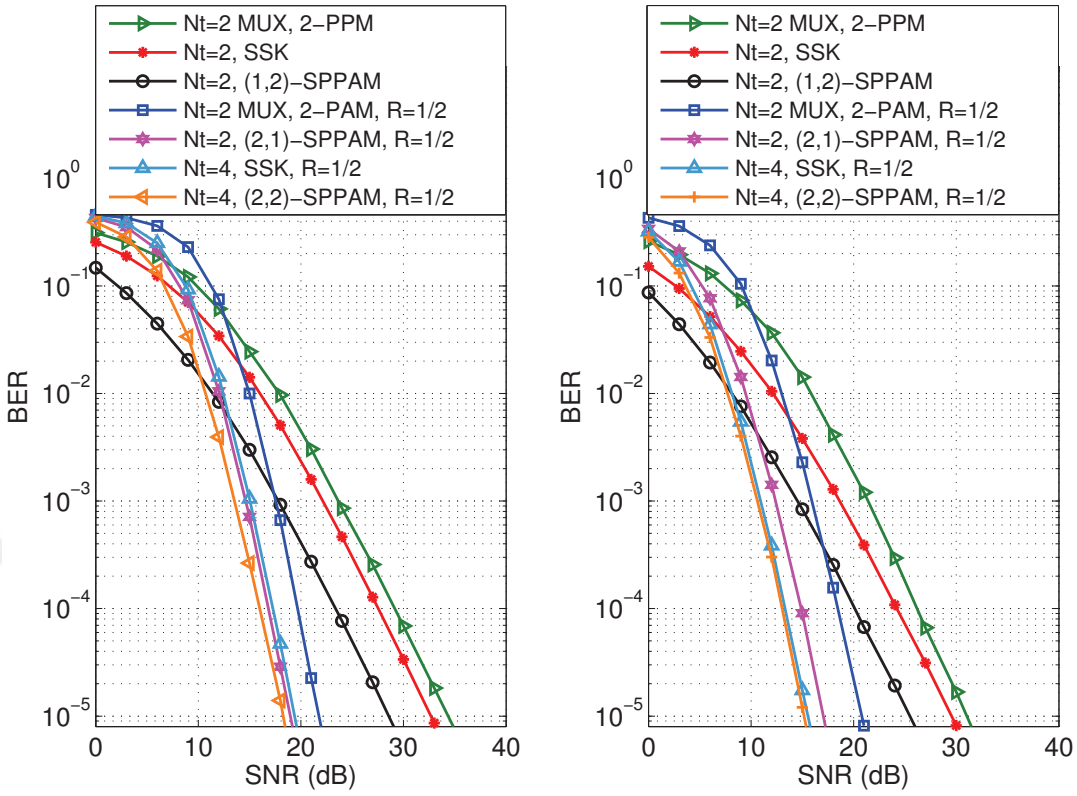

Figure 4.5. Simulation results at 1 b/s/Hz for (a) log-normal and (b) Gamma-Gamma distributed channels

corresponding to the type-IV error event, which makes it also possible to evaluate the full ABEP upper bound in (4.2).

The comparison of the theoretical ABEP upper bounds and the simulated performances for both log-normal and Gamma-Gamma fading channels are presented in Figure 4.4 for the uncoded and coded SPPAM systems. In the figures, the theoretical upper bounds are plotted with dashed curves. All curves (theoretical and simulated) are drawn down to at least 1×10^{-5} BER levels. As seen from all the plots theoretical performance curves are in agreement with the simulation results and indeed form relatively tight bounds.

Simulation results showing the comparative performances of 1, 2 and 3 b/s/Hz spectral efficiencies are given in Figure 4.5, Figure 4.6 and Figure 4.7, respectively.

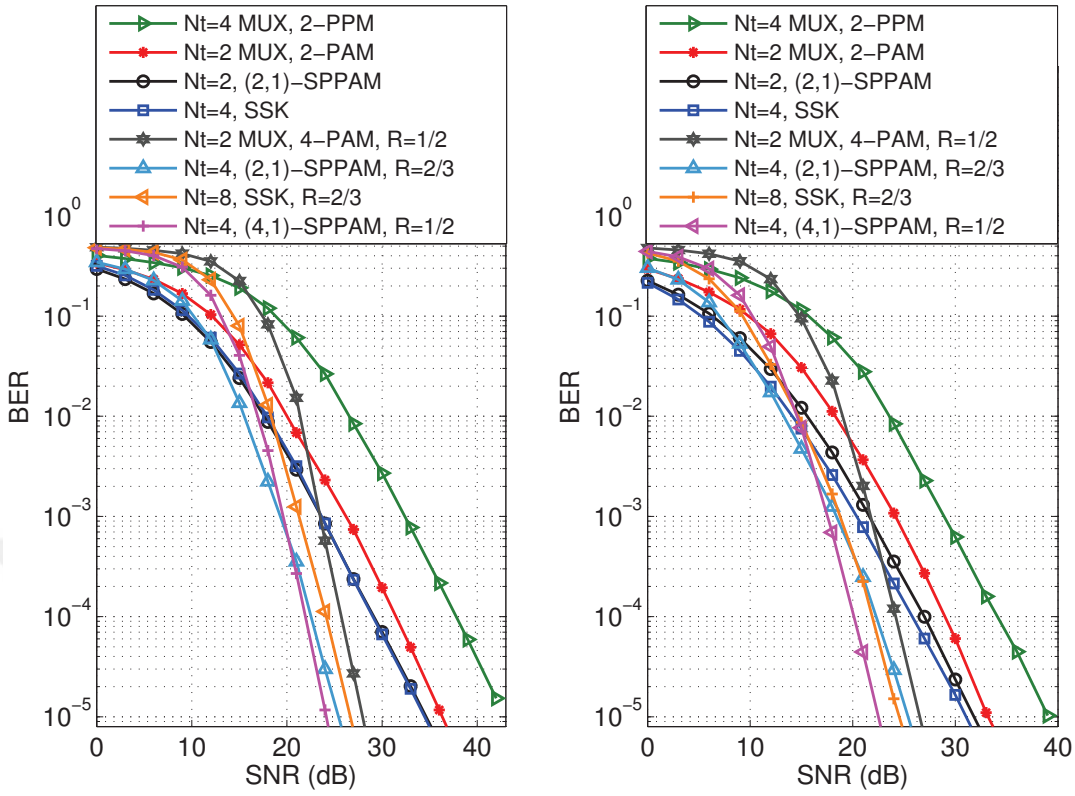

Figure 4.6. Simulation results at 2 b/s/Hz for (a) log-normal and (b) Gamma-Gamma distributed channels

Notice that 1 b/s/Hz spectral efficiency can be achieved by uncoded SSK with $N_t = 2$ or rate 1/2 coded SSK with $N_t = 4$. As seen in Figure 4.5, uncoded $(1, 2)$-SPPAM system performs 5 (4) dB better than the uncoded SSK system at 1×10^{-4} BER level for log-normal (Gamma-Gamma) channels. In fact, in both channels the coded $(2, 1)$-SPPAM with $N_t = 2$ and rate 1/2 performs slightly better than rate 1/2 coded SSK with $N_t = 4$. These observations validate the fact that SPPAM can be used to attain the same or sometimes better performances compared to those of SSK/SPPM systems with smaller number of transmitters. These benefits are particularly visible when the spectral efficiency requirement is high. However as seen from the example of rate 1/2 coded $(2, 2)$-SPPAM with $N_t = 4$ in Figure 4.5, the added benefit of using SPPAM at lower spectral efficiencies is not very significant. SPPAM is also compared with MUX. At 1×10^{-4} BER level and with rate 1/2 coding, $N_t = 2$ $(2, 1)$-SPPAM performs about 4dB better than $N_t = 2$ 2-PAM with MUX for both log-normal and

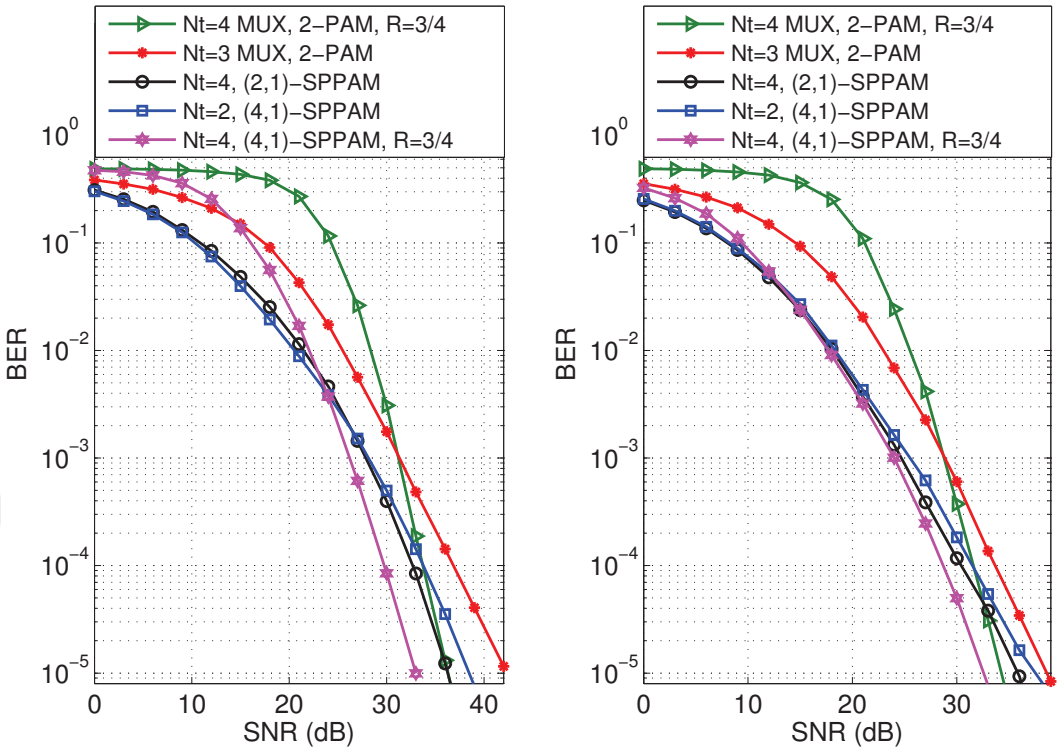

Figure 4.7. Simulation results at 3 b/s/Hz for (a) log-normal and (b) Gamma-Gamma distributed channels

Gamma-Gamma distributed channels.

Similary, as seen in Figure 4.6 $N_t = 4$ transmitters are needed in order for SSK to operate at 2 b/s/Hz spectral efficiency. On the other hand, $(2, 1)$-SPPAM with $N_t = 2$ operates with the same spectral efficiency with 1 dB performance gain in log-normal fading and only with a 1 dB performance loss in Gamma-Gamma fading in comparison to 4 transmitter SSK. In addition, contrary to SSK, it is possible to implement coded SPPAM schemes for better error performance at the same spectral efficiency. For instance, coded $(4, 1)$-SPPAM with $N_t = 2$ and rate 2/3 coding still has 2 b/s/Hz spectral efficiency and performs 5 (3) dB better than SSK with $N_t = 4$ at 1×10^{-4} BER level in log-normal (Gamma-Gamma) fading. When $(4, 1)$-SPPAM is used with $N_t = 4$ and rate 1/2 coding, an additional 2.5 (3.5) dB gain is possible. Similar to results for 1 b/s/Hz, SSK performs worse than SPPAM even with coding at 2

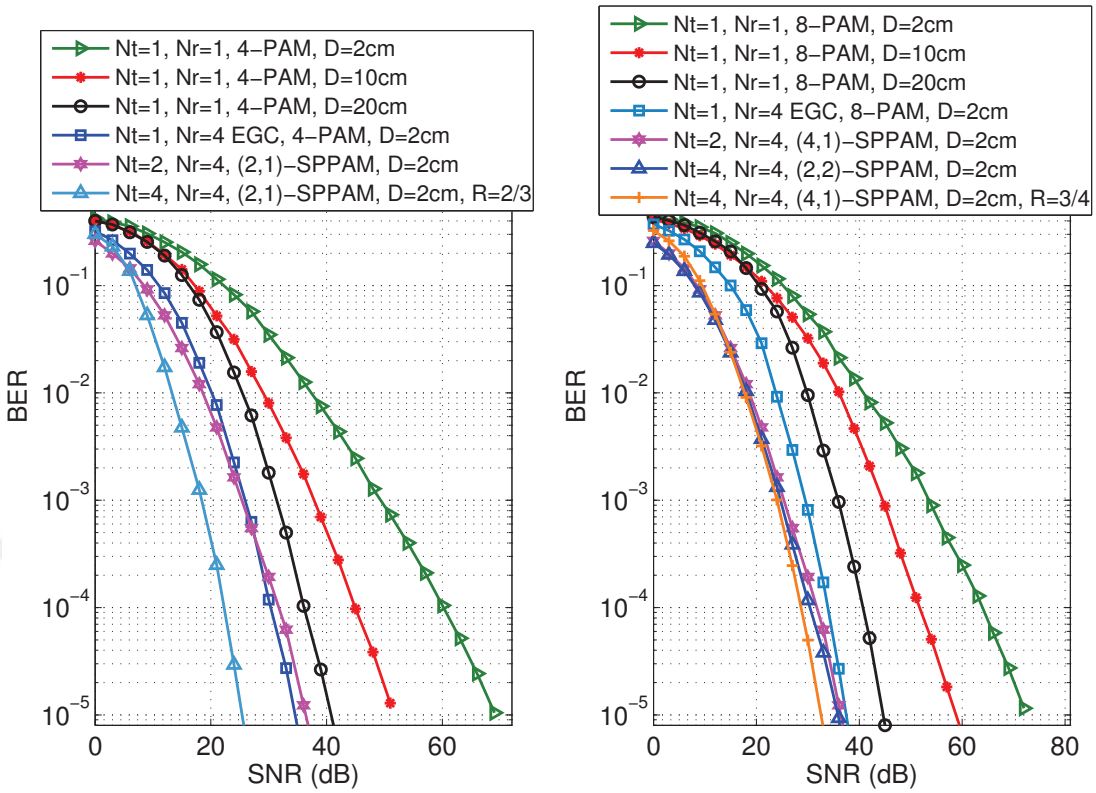

(a) (b)

Figure 4.8. Simulation results for the uncoded and coded SPPAM systems (a) at 2 b/s/Hz and (b) 3 b/s/Hz for Gamma-Gamma fading with scintillation indices $\sigma_I^2 = 1.09$ for $D = 2$ cm, $\sigma_I^2 = 0.42$ for $D = 10$ cm and $\sigma_I^2 = 0.22$ for $D = 20$ cm.

b/s/Hz. For log-normal (Gamma-Gamma) distributed channels with rate 2/3, $N_t = 4$ $(2,1)-$SPPAM performs about 3 (1) dB better than $N_t = 8$ SSK at 1×10^{-4} BER level. As seen from these examples, depending on the BER and SNR requirements of the system different SPPAM configurations with or without coding can be tailored while SSK lacks such flexibility. Again SPPAM is superior to MUX; at 1×10^{-4} BER level and with rate 1/2 coding, $N_t = 4$ $(4,1)$-SPPAM performs about 4dB better than $N_t = 2$ 4-PAM with MUX for both channel distributions.

As seen in Figure 4.7 with rate 3/4 coding, $N_t = 4$ $(4,1)$-SPPAM performs about 4dB better than $N_t = 4$ 2-PAM with MUX at 1×10^{-4} BER level for both log-normal and Gamma-Gamma distributed channels. The results show that for all spectral efficiencies a SPPAM scheme that is better than MUX schemes in terms of

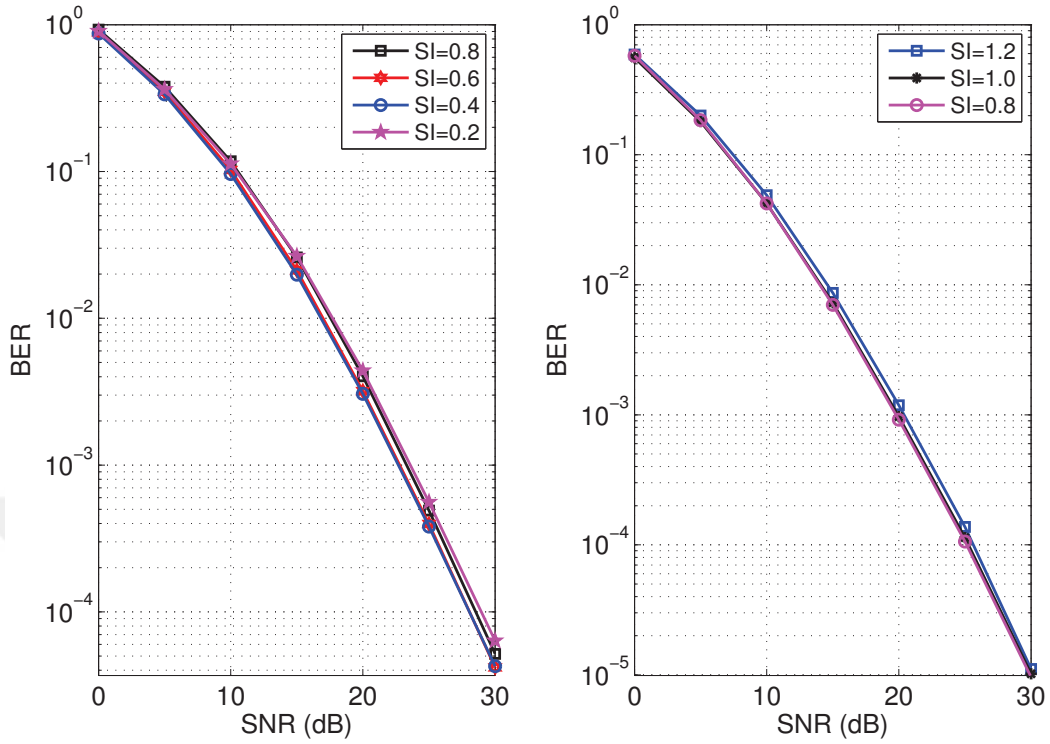

(a) (b)

Figure 4.9. Effect of SI on the performance of the SPPAM system for (a) log-normal and (b) Gamma-Gamma distributed channels

BER performance can be designed. Additionally, since ICI is completely avoided, SPPAM has reduced demultiplexing complexity compared to MUX.

As mentioned before, the true advantage of SPPAM is the ability to compensate for the power penalty of PAM and to obtain better performance gains via coding without changing the system configurations. On the other hand, the only way to employ coding with SSK without decreasing the spectral efficiency is to increase the number of transmitters whereas in SPPAM, arbitrary coding rates can be employed without any increase in the number of transmitters.

In the FSO literature generally either a single aperture is used to benefit from aperture averaging through reduction in the SI or multiple point apertures are used to exploit diversity through equal gain combining (EGC). For this reason we also

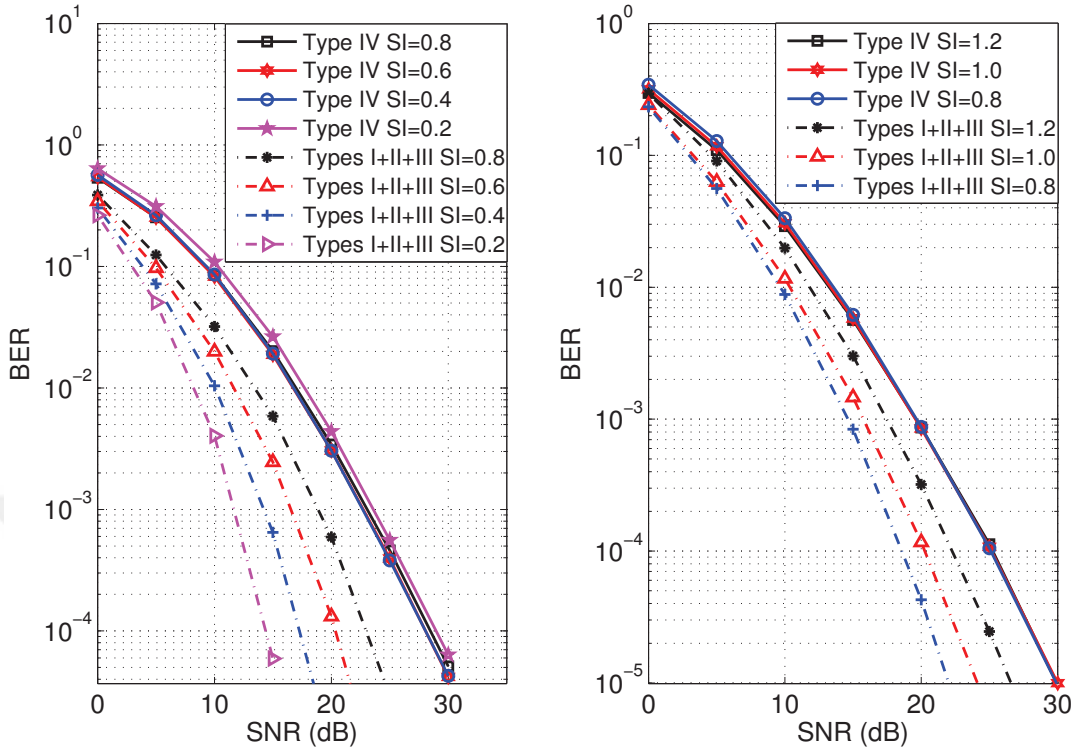

(a) (b)

Figure 4.10. Effect of SI on the performance of type-IV and sum of type-I, II and III errors for (a) log-normal and (b) Gamma-Gamma distributed channels

compare the performance of SPPAM with classical systems using aperture averaging and EGC for Gamma-Gamma distributed channels in Figure 4.8. At 2 b/s/Hz the performance of $N_t = 2$ $(2,1)-$SPPAM at 1×10^{-4} BER level is about 5dB better than that of 4-PAM exploiting aperture averaging with $D = 20$ cm and almost the same with the performance of 4-PAM using EGC with $N_r = 4$ receivers each having aperture diameter of $D = 2$ cm. With increased number of transmitters and coding the performance gains can be further improved as seen from the $N_t = 4$ $(2,1)-$SPPAM rate 2/3 curve. Similarly, at 3 b/s/Hz $N_t = 2$ $(4,1)-$SPPAM or $N_t = 4$ $(2,2)-$SPPAM performs about 10dB and 4 dB better than 8-PAM exploiting aperture averaging with $D = 20$ cm and 8-PAM using EGC with 4 $D = 2$ cm apertures, respectively at 1×10^{-4} BER level. Again with coding better performances can be obtained as $N_t = 4$ $(4,1)-$SPPAM with rate 3/4 has an additional 2dB performance gain compared to the other SPPAM configurations in the figure.

Table 4.4. Codes used in simulations

Rate	Puncturing pattern	d_{free}	d	B_d
1/2	-	5	[5 6 7]	[1 4 12]
2/3	[1 1 0 1]	3	[3 4 5]	[1 10 54]
3/4	[1 1 1 0 0 1]	3	[3 4 5]	[15 104 540]

Finally, we evaluate the impact of SI on the SPPAM performance. As shown in Figure 4.9 for both turbulence cases for the $N_t = 4$, $(2, 2)$-SPPAM system, the performance does not change significantly with increasing SI which can be justified again by the theoretical framework. For type-I,II and III errors, the S_I, S_{II} and S_{III} terms all appear as weighted sums of identically distributed - log-normal or Gamma-Gamma - random variables. This makes these error metrics to be described by an approximate log-normal or Gamma-Gamma random variable whose variation with the SI effects is in parallel to that of the original channel distribution. On the other hand, for type IV error in equation (4.10), the weighed difference of two random variables appear in the summation of S_{IV} which, unlike other error events, does not vary rapidly with SI as shown in Figure 4.10 for various scintillation indices. Moreover, this error is also more dominant than even the sum of all other error events, and thus determines the overall ABEP. Therefore SPPAM retains a certain degree of robustness against the variations in the channel turbulence effects.

4.5. Conclusion

In this chapter SPPAM is presented as a novel optical communication scheme offering spectral/power/performance efficiencies and a design flexibility over conventional optical communication systems. Furthermore, both theoretical analysis and simulation results show that when it is used in FSO systems, SPPAM also offers robustness against the performance degrading scintillation effects of the atmospheric turbulence channels. Although classical modulation schemes like PAM and PPM are widely used in optical communications PPM suffers from spectral efficiency and PAM

is not power efficient. Additionally high power levels can cause the optical device to work in the nonlinear region and thus must be avoided. Spatial multiplexing on the other hand is not very effective due to high channel correlation nature of the optical communication systems. SPPAM offers a compromise between spectral and power efficiencies. By distributing some of the bits to the spatial domain SPPAM provides reduction in the required PAM modulation level. This benefit comes at the expense of increased computational complexity at the receiver side in comparison to classical systems employing diversity combining or aperture averaging. On the other hand, because only one of the transmitters is active during each transmission slot, the ICI is avoided and the demultiplexing complexity is reduced. As a result, SPPAM is a more feasible than other spectrally efficient schemes employing spatial multiplexing in terms of receiver complexity.

5. POLARIZATION DIVERSITY IN MIMO COMMUNICATION OVER ATMOSPHERIC TURBULENCE CHANNELS

Selection of the right modulation scheme is very important for scintillation mitigation in FSO communications as mentioned in Chapter 1. The widely used intensity based modulations such as OOK and PPM are sensitive to atmospheric turbulence effects whereas phase modulation schemes such as PSK and DPSK suffer from phase noise as discussed in [2]. On the other hand, as shown in [38], SOP is much less sensitive to the turbulence induced fading than amplitude and phase. That is why, POLSK proposed in [39] forms a feasible alternative to optical intensity and phase modulation techniques because of its immunity to phase noise and efficiency for operation over long distances as shown in [40] and [41], respectively. Based on this idea the authors of [42] propose a non-coherent BPOLSK scheme that relies on using the SOP of a fully polarized beam having two orthogonal channels as the information bearing parameter.

The turbulence induced scintillation can also be reduced substantially through the redundancy provided by the use of multiple transmitters and/or receivers. For this reason POLSK is also utilized with MIMO FSO systems as shown in [43–45]. In all these systems coherent BPOLSK or coherent multilevel MPOLSK systems are investigated. On the other hand the non-coherent BPOLSK system of [42] has not been considered in a MIMO architecture. For this reason, the first contribution of this chapter is a novel non-coherent MIMO optical modulation method, denoted by PPM-BPOLSK, which combines the implementation simplicity and the performance gains of non-coherent BPOLSK with the power efficiency of PPM. We show by both theoretical analysis and simulation results that the proposed method provides improved error performances over atmospheric turbulence channels compared to systems employing only BPOLSK or PPM and thus constitutes a feasible alternative to other direct detection intensity modulation techniques in terms of power efficiency.

On the other hand, because the bandwidth has been assumed to be practically unlimited, the main design consideration in FSO systems has been power efficiency rather than spectral efficiency. However as mentioned in Chapter 1, recently there has been a surge of interest in systems which are also spectrally efficient. To achieve higher spectral efficiencies several approaches such as multilevel modulation schemes, SIM, spatial multiplexing and OSM are offered. Among these approaches the error performance of OSM is shown to be superior to other MIMO transmission techniques operating at the same spectral efficiency as discussed in Chapter 4. The required number of constellation levels for a selected spectral efficiency can be decreased by the use of OSM without sacrificing power efficiency and with less receiver complexity compared to MIMO spatial multiplexing techniques. This constellation level requirement can be further decreased with the inclusion of the polarization dimension. From another perspective, the use of polarization in addition to the transmitter index and symbolling dimensions may help implement an equivalent MIMO system with half as many transmitters/receivers and therefore achieve space efficiency. Thus the second contribution of this chapter is a novel coherent MIMO OSM architecture combining the SM principle with MPOLSK, denoted by SM-MPOLSK. Because one bit is allocated to the additional polarization dimension, the proposed OSM method requires smaller constellations or less number of transmit apertures than previously proposed OSM approaches of [13, 34, 46, 47]. As validated by both theoretical analysis and simulation results, because of the inherent robustness of POLSK to channel scintillation effects, the proposed OSM method utilizing polarization dimension as well as multiple transmit/receive apertures also provides improved error performances over atmospheric turbulence channels.

Notice that the proposed POLSK schemes convey information through multiple signalling dimensions, i.e., SOP and symbol dimensions for PPM-BPOLSK, and transmitter index, SOP and symbol dimensions for SM-MPOLSK. In both approaches, we evaluate the upper bounds for the ABEP corresponding to each bit group and show that bits belonging to different dimensions are affected unequally from the channel impairments. This makes it necessary for each signalling dimension to be protected with a different level of error control coding that is compatible with the rate of vulnerability

to the scintillation effects. For this reason, as a third contribution we also propose a simple yet effective UEP scheme for both PPM-BPOLSK and SM-MPOLSK systems. We show via both theoretical analysis and extensive simulations that the proposed UEP scheme is effective not only in removing the differences in ABEP's for individual signalling dimensions but also in improving the overall system performances.

The organization of the chapter is as follows: The analysis of PPM-BPOLSK and SM-MPOLSK systems are given in sections 5.1 and 5.2, respectively and coded architectures for both systems are investigated in Section 5.3. Simulation results are presented in Section 5.4 before the conclusive remarks in Section 5.5.

5.1. Non-Coherent Polarization Shift Keying with Pulse Position Modulation

As mentioned earlier, the first contribution of this chapter is a non-coherent MIMO optical modulation method, denoted by PPM-BPOLSK, that offers both power efficiency due to the use of PPM and also spectral efficiency with the utilization of BPOLSK. In the following we first describe the system model and then present the corresponding performance analysis.

5.1.1. System Model

We consider an $N_t \times N_r$ MIMO FSO system employing PPM-BPOLSK where N_t and N_r are the number of transmitters and receivers, as shown in Figure 5.1. The transmitter and receiver block diagrams of the proposed system are given in Figure 5.2. As seen in Figure 5.2-a after the beam is polarized into two orthogonal components denoted by p and p' by a polarization beam splitter (PBS), an M-ary PPM signal is transmitted from one of the directions while no signal is transmitted on the other. Then the two is combined with a polarization beam combiner (PBC) and transmitted through the atmosphere. As seen in Figure 5.2-b in the receiver, the outputs of the photodiodes (PD) are subtracted before being combined with the subtracted outputs from the other receivers and then sent to the matched filter (MF).

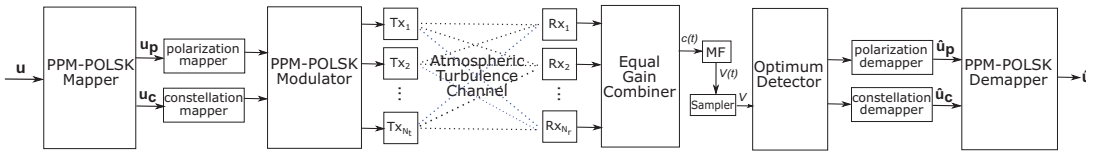

Figure 5.1. System model for PPM-BPOLSK. Tx stands for transmitter and Rx stands for receiver. $\mathbf{u}$ and $\widehat{\mathbf{u}}$ are the input and estimated bitstreams, respectively.

For the PPM-BPOLSK system at each time instant, the incoming bit stream is divided into blocks of $\log_2(2M)$ bits, of which 1 bit is used to select a polarization state and the remaining $\log_2(M)$ bits are mapped onto the position of the pulse to be transmitted in the selected SOP. Therefore the spectral efficiency of the system is $r = \log_2(2M)/M$ b/s/Hz. Notice that for the classic PPM system the spectral efficiency is $r = \log_2(M)/M$ b/s/Hz, thus using polarization dimension in conjunction with PPM brings an additional $1/M$ b/s/Hz spectral efficiency.

The PPM-BPOLSK signal is transmitted over the atmospheric turbulence channel that is described by the $N_r \times N_t$ dimensional channel matrices $\mathbf{H}_p$ and $\mathbf{H}_{p'}$ corresponding to each SOP. The signal is transmitted from one of the polarizations while the other is left idle.

Therefore the output of the j-th photodiode corresponding to the input from the i-th transmitter $c_{ji}(t) = c_{x,ji}(t) - c_{y,ji}(t)$ is given as

$$c_{ji}(t) \;=\; \begin{cases} \Re^2 P m(t)\mathbf{H}_{p,ij}/2 + n_j(t), & \text{for } \wp = p \\ -\Re^2 P m(t)\mathbf{H}_{p',ij}/2 + n_j(t), & \text{for } \wp = p' \end{cases} \tag{5.1}$$

where $\wp \in \{p, p'\}$ denotes the active SOP, and $\Re$ is the photodiode responsivity, P is the transmitted power, $m(t)$ is the transmitted PPM signal, $\mathbf{H}_{\wp,ij} = [\mathbf{H}_\wp]_{ji}$ and $n_j(t)$ is zero mean Gaussian noise with variance $\sigma_n^2/2$. As shown in [33, 61] since RC outperforms other MIMO transmission schemes in terms of performance, we employ RC at the transmitter side, that is all the transmitters send the same information. On the other hand at the receiver side the received signal can be processed as vector information by using joint ML detection as done in [11] or as a single metric using

aperture averaging or diversity combining as considered in [21] and [27], respectively. As shown in [27] the loss of performance when using EGC is negligible compared to optimal combining and for this reason we use EGC at the receiver side, which has less receiver complexity. The signal at the output of the EGC block $c(t)$ is first applied to a MF with impulse response $h_{MF}(t)$ yielding $V(t) = c(t) * h_{MF}(t)$ and the output of the MF is then sampled at the end of one symbol duration to obtain the decision variable $\mathbf{V}$. As a result the input to the detector becomes

$$\mathbf{V} = \begin{cases} \frac{\Re^2 P}{2\sqrt{N_r}} \sum_{i=1}^{N_t} \sum_{j=1}^{N_r} \mathbf{H}_{p,ij}\mathbf{x}_m + \mathbf{n}, & \text{for } \wp = p \\ -\frac{\Re^2 P}{2\sqrt{N_r}} \sum_{i=1}^{N_t} \sum_{j=1}^{N_r} \mathbf{H}_{p',ij}\mathbf{x}_m + \mathbf{n}, & \text{for } \wp = p' \end{cases} \tag{5.2}$$

where $\mathbf{x}_m = [0 \ldots 0 \sqrt{M} 0 \ldots 0]$ (the non-zero term is in the m-th position) and $1 \times M$ dimensional $\mathbf{n}$ is formed by i.i.d. entries with zero mean and $\sigma_n^2/2$ variance.

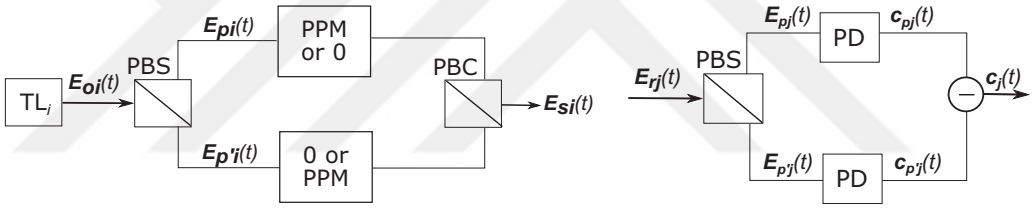

(a) (b)

Figure 5.2. PPM-BPOLSK transceiver model. (a) Transmitter model for the i-th transmitter and (b) receiver model for the j-th receiver. TL, PD, PBS and PBC stand for transmitting laser, photodiode, polarization beam splitter and polarization beam combiner, respectively.

The SOP and the POLSK symbol are determined by an ML detector using $\mathbf{V}$. Assuming equally likely symbols, the optimum ML detection rule can be expressed for $\wp \in \{p, p'\}$, $m = 1, 2, \ldots, M$ as

$$(\ \widehat{\wp}, \widehat{m}\ ) = \arg\min_{\wp,m} \|\mathbf{V} - \mathbf{s}_{\wp,m}\|^2 \tag{5.3}$$

where $\mathbf{s}_{\wp,m}$ is the transmitted signal when m-th PPM signal is transmitted from the

SOP $\wp$ given as

$$\mathbf{s}_{\wp,m} = \frac{\Re^2 P}{2\sqrt{N_r}} \sum_{i=1}^{N_t} \sum_{j=1}^{N_r} \mathbf{H}_{\wp,ij} \mathbf{x}_m \tag{5.4}$$

and $\widehat{\wp}$ and $\widehat{m}$ are the estimated SOP and transmitted PPM symbol, respectively.

5.1.2. ABEP Analysis

We present here an ABEP analysis under the optimum ML decision rule given in (5.3) similar to the ABEP analysis performed in Chapter 4. In general deriving the exact ABEP is computationally intractable because optimal detection requires a joint detection of the polarization states and symbols, however a tight upper bound can be expressed by using the union bounding approach given in [94] as

$$\begin{aligned} \text{ABEP} \;\leq\; & \frac{1}{2M} \sum_{\wp \in \{p,p'\}} \sum_{\widehat{\wp} \in \{p,p'\}} \sum_{m=1}^{M} \sum_{\widehat{m}=1}^{M} \frac{N_e}{\log_2(2M)} \\ & \times \text{APEP}(\wp, m, \widehat{\wp}, \widehat{m} | \mathbf{H}_{\wp}, \mathbf{H}_{\widehat{\wp}}, \mathbf{x}_m, \mathbf{x}_{\widehat{m}}) \end{aligned} \tag{5.5}$$

where N_e is the number of bits in error and $\text{APEP}(\wp, m, \widehat{\wp}, \widehat{m} | \mathbf{H}_{\wp}, \mathbf{H}_{\widehat{\wp}}, \mathbf{x}_m, \mathbf{x}_{\widehat{m}})$ is the APEP for deciding in favor of the index pair $(\wp, m)$ instead of the ML optimum pair $(\widehat{\wp}, \widehat{m})$. Using the approximation $N_e / \log_2(2M) \approx 1/2$ given in [94], this expression can also be simplified as

$$\text{ABEP} \;\leq\; \frac{1}{4M} \sum_{\wp \in \{p,p'\}} \sum_{\widehat{\wp} \in \{p,p'\}} \sum_{m=1}^{M} \sum_{\widehat{m}=1}^{M} \text{APEP}(\wp, m, \widehat{\wp}, \widehat{m} | \mathbf{H}_{\wp}, \mathbf{H}_{\widehat{\wp}}, \mathbf{x}_m, \mathbf{x}_{\widehat{m}}). \tag{5.6}$$

The APEP in (5.6) can be expressed as

$$\text{APEP}(\wp, m, \widehat{\wp}, \widehat{m} | \mathbf{H}_{\wp}, \mathbf{H}_{\widehat{\wp}}, \mathbf{x}_m, \mathbf{x}_{\widehat{m}}) = \text{E}_{\mathbf{H}_{\wp}, \mathbf{H}_{\widehat{\wp}}} \left[\text{Q}\left(\sqrt{\frac{\rho S}{2}} \right) \right] \tag{5.7}$$

after some algebraic manipulations, where ρ is the electrical SNR expressed as $\rho = \Re^2 P/N_t^2 2\sigma_n^2$ and

$$S = ||\mathbf{h}_{\wp}^T \mathbf{x}_m + \mathbf{h}_{\widehat{\wp}}^T \mathbf{x}_{\widehat{m}})||^2 \tag{5.8}$$

with $\mathbf{h}_{\wp} = \sum_{j=1}^{N_r} \mathbf{H}_{\wp,j}/\sqrt{N_r}$ and $\mathbf{h}_{\widehat{\wp}} = \sum_{j=1}^{N_r} \mathbf{H}_{\widehat{\wp},j}/\sqrt{N_r}$.

Notice that using Craig's formulation in (4.5) the APEP in (5.7) can be rewritten in terms of a single definite integral as

$$\text{APEP} \;=\; \frac{1}{\pi}\int_0^{\pi/2} M_S\left(-\frac{\rho}{4\sin^2\theta}\right) d\theta \tag{5.9}$$

where $M_S(t) = \int_0^{\infty} f_S(\Gamma) e^{\Gamma t} d\Gamma$ is again the MGF of the random variable S.

Similar to the ABEP analysis approach mentioned in Chapter 4 the key to the computation of ABEP upper bound in (5.6) is to identify distinct error cases and to derive the corresponding APEPs as given in (5.7). Notice that there are $2M$ cases where both the SOP and the transmitted PPM symbol are correctly detected. All the other remaining cases correspond to an error event. However, a careful study of the cases reveals that there are only three distinct error events as summarized in the next subsection.

5.1.2.1. Error Types. As mentioned above in addition to $2M$ cases where all indices are detected correctly, there are three distinct error types which encompasses all error events as shown below:

i) *Type-I error*: Neither the pulse positions nor SOP are correctly detected, i.e., $\wp \neq \widehat{\wp}, m \neq \widehat{m}$. which results in the error metric in (5.8) corresponding to type-I error, S_I, as

$$S_I = M\sum_{i=1}^{N_t}\left(\mathbf{h}_{\wp,i}^2 + \mathbf{h}_{\widehat{\wp},i}^2\right) = \frac{M}{N_r}\sum_{i=1}^{N_t}\left[\left(\sum_{j=1}^{N_r}\mathbf{H}_{\wp,ij}\right)^2 + \left(\sum_{j=1}^{N_r}\mathbf{H}_{\widehat{\wp},ij}\right)^2\right] \tag{5.10}$$

and there are $2M(M-1)$ terms corresponding to type-I error in (5.6).

ii) *Type-II error*: The SOP is correctly detected but the PPM symbol is not, i.e., $\wp = \widehat{\wp}, m \neq \widehat{m}$ and there are $2M(M-1)$ terms corresponding to type II error. The error metric in (5.8) corresponding to type-II error, S_{II}, is given as

$$S_{II} = 2M \sum_{i=1}^{N_t} \mathbf{h}_{\wp,i}^2 = \frac{2M}{N_r} \sum_{i=1}^{N_t} \left(\sum_{j=1}^{N_r} \mathbf{H}_{\wp,ij} \right)^2. \tag{5.11}$$

iii) *Type-III error*: The pulse position is correctly detected but the SOP is not, i.e., $\wp \neq \widehat{\wp}, m = \widehat{m}$. There are $2M$ terms corresponding to type-III error. The error metric in (5.8) corresponding to type-III error, S_{III}, is given as

$$S_{III} = M \sum_{i=1}^{N_t} (\mathbf{h}_{\wp,i} + \mathbf{h}_{\widehat{\wp},i})^2 = \frac{M}{N_r} \sum_{i=1}^{N_t} \left[\left(\sum_{j=1}^{N_r} \mathbf{H}_{\wp,ij} \right) + \left(\sum_{j=1}^{N_r} \mathbf{H}_{\widehat{\wp},ij} \right) \right]^2. \tag{5.12}$$

As a result, the ABEP upper bound in (5.6) can be written in terms of 3 distinct APEP summations such that

$$\text{ABEP} \leq \frac{1}{2}[(M-1)(\text{APEP}_I + \text{APEP}_{II}) + \text{APEP}_{III}] \tag{5.13}$$

where APEP_i's are the APEPs in (5.7) corresponding to type $i \in \{I, II, III\}$ errors, respectively.

5.1.2.2. APEP Analysis Under Weak-to-Moderate Turbulence. Under weak-to-moderate turbulence conditions the evaluation of the error types require the distribution of sum of squared log-normal random variables, which is shown to be log-normal in Chapter 4. Following the same approach used in Chapter 4 for determining the parameters of $S \approx e^U$ we find μ_U and σ_U as

$$\begin{aligned} \mu_U &= \log\left(\mu_S / \sqrt{1 + \sigma_S^2/\mu_S^2} \right) \\ \sigma_U^2 &= \log\left(1 + \sigma_S^2/\mu_S^2\right), \end{aligned} \tag{5.14}$$

where

$$\begin{aligned}
\mu_S &= c_2(M/N_r)\exp(2\mu_V + 2\sigma_V^2)c_3N_t \\
\sigma_S^2 &= c_2^2(M/N_r)^2(\exp(4\sigma_V^2) - 1)\exp(4\mu_V + 4\sigma_V^2)c_3N_t \\
\mu_V &= \log\left(\mu_T/\sqrt{1+\sigma_T^2/\mu_T^2}\right) \\
\sigma_V^2 &= \log\left(1+\sigma_T^2/\mu_T^2\right) \\
\mu_T &= c_1N_r\exp(\mu_X + 2\sigma_X^2/2) \\
\sigma_T^2 &= c_1N_r(\exp(\sigma_X^2) - 1)\exp(2\mu_X + \sigma_X^2). \qquad (5.15)
\end{aligned}$$

The constant triple (c_1, c_2, c_3) are $(1, 1, 2)$, $(1, 2, 1)$ and $(2, 1, 1)$ for type-I, II and III errors, respectively. Finally, using (4.14) in equation (5.9), the ABEP expressions corresponding to type-I, II and III errors can be written as

$$\text{APEP}_{\text{I,II,III}} \approx \sum_{n=1}^{N_{GH}} \frac{w_n}{\sqrt{\pi}} Q\left(\sqrt{\frac{\rho}{4}e^{\sqrt{2}\sigma_U a_n + \mu_U}}\right). \qquad (5.16)$$

5.1.2.3. APEP Analysis Under Moderate-to-Strong Turbulence. Under moderate-to-strong turbulence conditions the error types require the distribution of sum of squared Gamma-Gamma random variables. A Gamma-Gamma variable is derived from the product of two independent Gamma variables [90]. Suppose X_i, Y_i are Gamma distributed random variables with parameters $(m_{X_i} = \alpha, n_{X_i} = 1/\alpha)$ and $(m_{Y_i} = \beta, n_{Y_i} = 1/\beta)$, respectively. Then $h_i = X_iY_i$ is a Gamma-Gamma variable with PDF given in (2.2). It is proven in [90] that sum of Gamma-Gamma random variables, that is $S = \sum_i^N h_i$ are approximately Gamma-Gamma distributed with parameters $(m_X = N\alpha + \epsilon_N, n_X = 1/(N\alpha + \epsilon_N))$ and $(m_Y = L\beta, n_Y = 1/\beta)$ where $S \approx XY$ and ϵ_N is the adjustment parameter given by

$$\epsilon_N = (N-1)\frac{-0.127 - 0.95\alpha - 0.0058\beta}{1 + 0.00124\alpha + 0.98\beta}. \qquad (5.17)$$

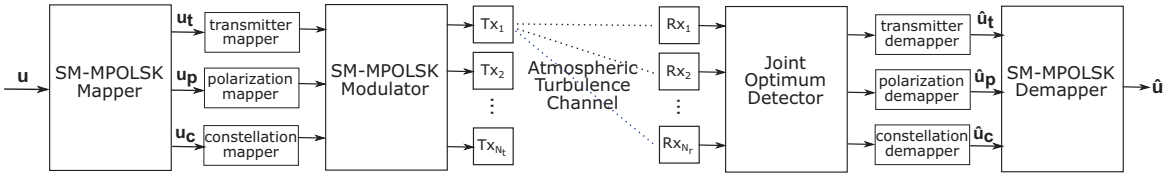

Figure 5.3. System model for SM-MPOLSK. Tx stands for transmitter and Rx stands for receiver. $\mathbf{u}$ and $\widehat{\mathbf{u}}$ are the input and estimated bitstreams, respectively.

Therefore if $\mathbf{H}_{\widehat{p},ij}$ are Gamma-Gamma distributed with parameters $(\alpha, 1/\alpha)$ and $(\beta, 1/\beta)$ then $\mathbf{h}_{p,i}$ are approximately Gamma-Gamma distributed with parameters $(N_r\alpha + \epsilon_{N_r}, 1/(N_r\alpha + \epsilon_{N_r}))$ and $(N_r\beta, 1/\beta)$.

Using the MGF approach of Chapter 4 the integral in (5.9) becomes

$$\text{APEP} = \frac{1}{\pi}\int_0^{\pi/2}\left(\frac{\sqrt{\alpha_T\beta_T}^{\alpha_T+\beta_T}\left(\frac{\rho}{4\sin^2\theta}\right)^{-\frac{\alpha_T+\beta_T}{4}}}{4\pi\Gamma(\alpha_T)\Gamma(\beta_T)}\times \mathrm{G}_{1,4}^{4,1}\left[\frac{(\alpha_T\beta_T\sin\theta)^2}{4(c_2M/N_r)\rho}\middle|\begin{matrix}1-\frac{\alpha_T+\beta_T}{4}\\ \frac{\alpha_T-\beta_T}{4},\frac{\alpha_T-\beta_T+2}{4},\frac{-\alpha_T+\beta_T}{4},\frac{-\alpha_T+\beta_T+2}{4}\end{matrix}\right]\right)^{c_3N_t} d\theta, \tag{5.18}$$

with $\alpha_T = c_1Nr\alpha + \epsilon_{c_1N_r}$, $\beta_T = c_1Nr\beta$ where the (c_1, c_2, c_3) constants triple are again $(1, 1, 2)$, $(1, 2, 1)$ and $(2, 1, 1)$ for type-I, II and III errors, respectively.

5.2. Coherent Polarization Shift Keying with Spatial Modulation

The second contribution of this chapter is the proposal of a spectrally efficient non-coherent MIMO OSM method, denoted by SM-MPOLSK, which combines the two spectrally efficient principles, SM and MPOLSK. In the following we first describe the system model and then again present the corresponding performance analysis.

5.2.1. System Model

Similar to the PPM-BPOLSK system we consider an $N_t \times N_r$ MIMO FSO system employing SM-MPOLSK as shown in Figure 5.3 where N_t and N_r are again the number of transmitters and receivers, respectively. Notice that each transmitter and receiver block in Figure 5.3 is as given in Figure 5.4 and N_t is assumed to be an integer power of 2. Using the polarization dimension virtually duplicates the number of channels available in the MIMO setup compared to the OSM system in Chapter 4. At each time instant, the SM-MPOLSK modulator divides the incoming bit stream into blocks of $\log_2(N_t M)$ bits. Of these bits, $\log_2(N_t)$ and $\log_2(M) - 1$ bits are used to determine the indices of the active transmitter and the $M/2$-ary amplitude level, respectively and the the remaining single bit is used to determine the SOP. Therefore the spectral efficiency of the system is $r = \log_2(MN_t)$ b/s/Hz. Notice the ordinary MPOLSK system has a spectral efficiency of $r = \log_2(M)$ b/s/Hz, therefore introduction of SM to the MPOLSK system increases the spectral efficiency by $\log_2(N_t)$ b/s/Hz. By this way some of the bits can be distributed to the spatial domain to decrease the required number of amplitude levels of MPOLSK.

As seen in Figure 5.4 the wave from the transmitting laser is decomposed by the PBS into two orthogonally polarized p and p' components. The amplitude and phase of the p component is are modulated with amplitude and phase modulators while the p' component is used as a reference carrier. Then these two components are combined with a PBC and transmitted through the atmosphere. At the receiver side, the received wave is split into p and p' components by a PBS, which are then mixed with p and p' components of the signal generated by the local oscillator (LO). These optical signals are detected by PD's and the resulting electrical signals are passed through BPF's to reject the constant term and limit the noise. Then the electrical currents at the output of BPF's are multiplied and integrated over one symbolling period at the MF and finally sampled to obtain $\mathbf{V}$, which is the input to the detector.

The MPOLSK signal is transmitted over the MIMO atmospheric turbulence channel that is described by the $N_r \times N_t$ dimensional channel matrix $\mathbf{H}$. Following

the system in [2] the output of the demodulators $\mathbf{V}$ is given as

$$\mathbf{V} = \sqrt{\frac{\mathbf{h}_t \Re^2 P_r P_{lo}}{8}} \left[\sqrt{\frac{\mathbf{h}_t \Re^2 P_r P_{lo}}{2}} \varepsilon_m \cos(\beta_m) + \mathbf{n}_{pb}^{'} + \mathbf{n}_{p'b}^{'} \right]$$

where $\Re$, P_r, P_{lo}, $\varepsilon_m \in [1, 3, 5 \ldots, M/2 - 1]$ and $\beta_m \in [0, \pi]$ are the photodetector responsivity, the power of the received optical signal, the optical power from the local oscillator, and the amplitude and the phase modulation parameters corresponding to the m-th symbol from the MPOLSK constellation, respectively. Here $\mathbf{h}_t$ is the t-th column of the channel matrix $\mathbf{H}$ with t denoting the active transmitter, and $\{[\mathbf{n}_{pb}^{'}]_i, [\mathbf{n}_{p'b}^{'}]_i\} \sim \mathcal{N}(0, \sigma_n^2/2)$, $i \in \{1, 2, \ldots N_r\}$ are the noise variances from the orthogonally polarized components of the optical signal denoted by p and p' with σ_n^2 being the variance of the noise components at the output of the photodetector. The electrical SNR at the input of the demodulator is defined as $\rho = P_{av}/2\sigma_n^2$ where P_{av} is the average power per bit given as

$$P_{av} = \frac{\Re^2 P_r P_{lo}}{M \log_2(M N_t)} \sum_{m=0}^{M/2-1} [1 + (1 + 2m)^2].$$

The average optical signal power $E[\Re^2 P_r P_{lo}]$ is normalized to 1 for all schemes considered to make fair comparisons possible. Sample OSM and SM-MPOLSK mappings are given in Table 5.1 for 3 b/s/Hz spectral efficiency. Notice the OSM scheme considered here is the SPPAM of Chapter 4.

At the receiver side the indices of the active transmitter and the MPOLSK symbol are determined by a joint ML detector and mapped back to the estimated bit stream. Assuming equally likely symbols, the joint optimum ML detection rule can be expressed for $t = 1, 2, \ldots, N_t$, $m = 1, 2, \ldots, M$ as

$$(\, \widehat{t}, \widehat{m}\,) = \arg \min_{t,m} \|\mathbf{V} - \mathbf{x}_{t,m}\|^2 \tag{5.19}$$

where $\mathbf{x}_{t,m}$ is the transmitted signal when m-th MPOLSK symbol is transmitted by

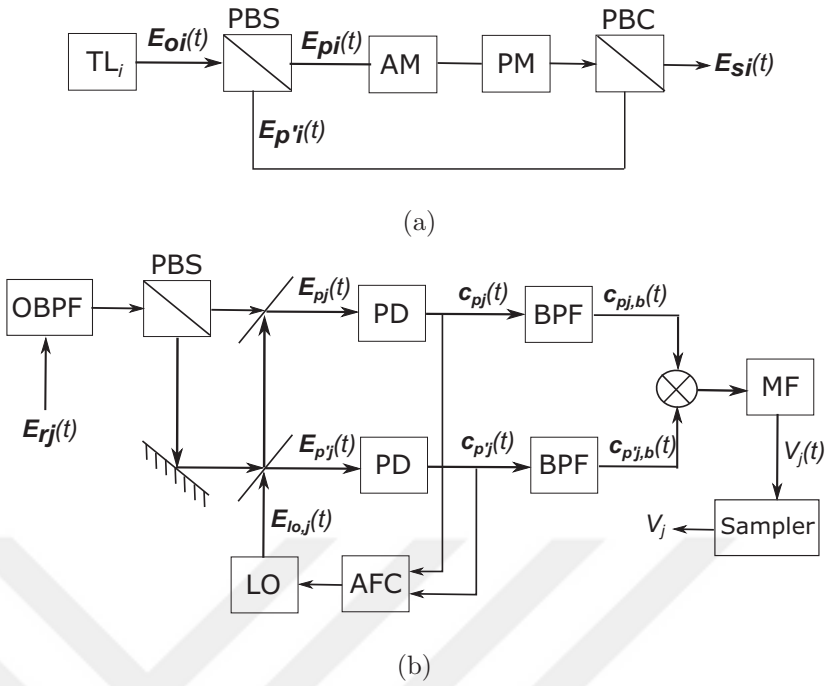

Figure 5.4. SM-MPOLSK transceiver model. (a) Transmitter model for the i-th transmitter and (b) receiver model for the j-th receiver. TL, PBS, PBC, PM, AM, OBPF, BPF, LO, AFC, PD and MF stand for transmitting laser, polarization beam splitter, polarization beam combiner, phase modulator, amplitude modulator, optical band pass filter, band pass filter, local oscillator, automatic frequency controller, photodiode and matched filter, respectively.

the t-th transmitter given as

$$\mathbf{x}_{t,m} = \frac{\mathbf{h}_t \Re^2 P_r P_{lo}}{4} \varepsilon_m \cos(\beta_m) \tag{5.20}$$

and $\widehat{t}$ and $\widehat{m}$ are the estimated indices for active transmitter and transmitted MPOLSK symbol, respectively.

5.2.2. ABEP Analysis

We present here an ABEP analysis under the optimum ML decision rule given in equation (5.19). Similar to the PPM-BPOLSK system a tight upper bound can be

Table 5.1. A sample OSM and SM-MPOLSK mapping for 3 b/s/Hz spectral efficiency

	$N_t = 2$ (4,1)-SPPAM mapping			$N_t = 2$ SM-2POLSK mapping				
Input bitstream	Tx bit	Symbol bits	ε_m	Tx bit	SOP bit	β_m	Symbol bit	ε_m
0 0 0	0	0 0	1	0	0	0	0	1
0 0 1	0	0 1	3	0	0	π	1	3
0 1 0	0	1 0	5	0	1	0	0	1
0 1 1	0	1 1	7	0	1	π	1	3
1 0 0	1	0 0	1	1	0	0	0	1
1 0 1	1	0 1	3	1	0	π	1	3
1 1 0	1	1 0	5	1	1	0	0	1
1 1 1	1	1 1	7	1	1	π	1	3

expressed as

$$\text{ABEP} \leq \frac{1}{2MN_t} \sum_{t=1}^{N_t} \sum_{\widehat{t}=1}^{N_t} \sum_{m=1}^{M} \sum_{\widehat{m}=1}^{M} \text{APEP}(t, m, \widehat{t}, \widehat{m} | \mathbf{h}_t, \mathbf{h}_{\widehat{t}}, \varepsilon_m, \varepsilon_{\widehat{m}}, \beta_m, \beta_{\widehat{m}}). \quad (5.21)$$

Here $\text{APEP}(t, m, \widehat{t}, \widehat{m} | \mathbf{h}_t, \mathbf{h}_{\widehat{t}}, \varepsilon_m, \varepsilon_{\widehat{m}}, \beta_m, \beta_{\widehat{m}})$ is the APEP for deciding in favor of the index couple $(\widehat{t}, \widehat{m})$ instead of (t, m) given by

$$\text{APEP}(t, m, \widehat{t}, \widehat{m} | \mathbf{h}_t, \mathbf{h}_{\widehat{t}}, \varepsilon_m, \varepsilon_{\widehat{m}}, \beta_m, \beta_{\widehat{m}}) = \text{E}_{\mathbf{h}_t, \mathbf{h}_{\widehat{t}}} \left[\text{Q} \left(\frac{2\sqrt{\rho} ||\mathbf{s}||^2}{\sqrt{P_{av}} ||\sqrt{\mathbf{h}_t} \mathbf{s}||} \right) \right] \quad (5.22)$$

after some algebraic manipulations, where ρ is the electrical SNR expressed as $\rho = P_{av}/2\sigma_n^2$ and $\mathbf{s} = \mathbf{h}_t \varepsilon_m \cos(\beta_m) - \mathbf{h}_{\widehat{t}} \varepsilon_{\widehat{m}} \cos(\beta_{\widehat{m}})$. To evaluate the APEP in (5.22) the performance analysis mentioned in Chapter 4 or Monte Carlo simulations can be utilized since the derivation of a closed form expression for this equation is not straightforward.

5.3. Coded architectures

The respective performances of the proposed schemes in the preceding two sections can further be improved via the use of coding. In this regard, the conventional approach in optical system design is to pair an encoder-decoder pair to the transmit/receive chain and to distribute the redundancy provided by coding to all input bits without any discrimination. This approach, also denoted by EEP, is suitable for systems where the information is homogeneous. However for many communication scenarios where the scintillation vulnerability of the information bits is not homogeneous, applying the same amount of protection to all the data may be feasible but wasteful. For these scenarios the so-called UEP approach, which is proposed first in [95], becomes more effective where each group of information is protected proportional to their susceptibility to scintillation.

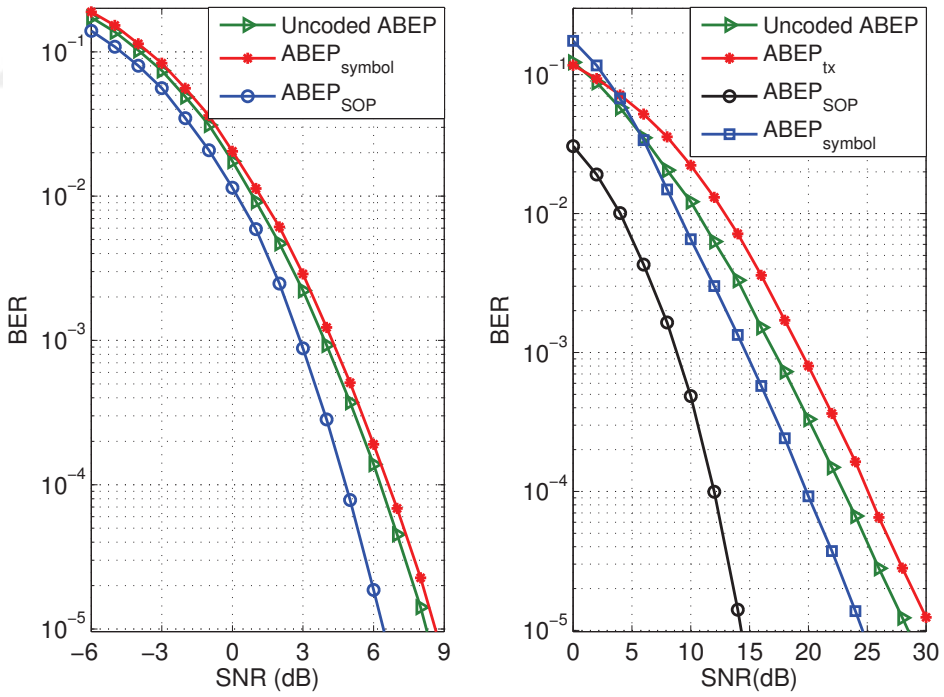

(a) (b)

Figure 5.5. Performance results for the uncoded (a) 4PPM-BPOLSK and (b) $N_t = 4$ SM-8POLSK systems under Gamma-Gamma fading with $\sigma_I^2 = 1.122$.

Upon close investigation of ABEP results for PPM-BPOLSK in atmospheric turbulence channels we observe that for certain configurations symbol bits are more vulnerable to scintillation effects than SOP bits as shown in Figure 5.5-a. For this reason for such configurations we may apply coding with UEP and protect symbol bits more than SOP bits or even only symbol bits can be protected while SOP bits are left unprotected. The SOP and symbol ABEPs in the figure are given respectively by

$$\begin{aligned} \mathrm{ABEP_{SOP}} \;\leq\; & \frac{1}{2M} \sum_{\wp \in \{p,p'\}} \sum_{\widehat{\wp} \in \{p,p'\}} \sum_{m=1}^{M} \sum_{\widehat{m}=1}^{M} N^{e}_{SOP} \\ & \mathrm{APEP}(\wp, m, \widehat{\wp}, \widehat{m} | \mathbf{H}_{\wp}, \mathbf{H}_{\widehat{\wp}}, \mathbf{x}_{m}, \mathbf{x}_{\widehat{m}}), \end{aligned} \tag{5.23}$$

where N^{e}_{SOP} is 0 if the SOP is detected correctly or 1 otherwise, and

$$\begin{aligned} \mathrm{ABEP_{symbol}} \;\leq\; & \frac{1}{2M} \sum_{\wp \in \{p,p'\}} \sum_{\widehat{\wp} \in \{p,p'\}} \sum_{m=1}^{M} \sum_{\widehat{m}=1}^{M} \frac{N^{e}_{symbol}}{\log_2 M} \\ & \mathrm{APEP}(\wp, m, \widehat{\wp}, \widehat{m} | \mathbf{H}_{\wp}, \mathbf{H}_{\widehat{\wp}}, \mathbf{x}_{m}, \mathbf{x}_{\widehat{m}}), \end{aligned} \tag{5.24}$$

where N^{e}_{symbol} is the number of symbol bits in error.

For the coded UEP PPM-BPOLSK system we add a convolutional encoder and an ML decoder to the transmitter and receiver sides of the original system as seen in Figure 5.6. For this UEP system the input bitstream is first encoded by a convolutional encoder, then the encoded bits are taken to the PPM-BPOLSK modulator before the mapped SOP and symbol bits are interleaved separately. At the receiver side we consider both hard input decoding (HID) and soft input decoding (SID). For the HID system, bit groups belonging to SOP and symbol dimensions are first demapped and deinterleaved separately and then decoded to obtain the estimated information bits. For the SID on the other hand, first log-likelihood ratios (LLR) corresponding to each demapped bit group are calculated as done in [96], then these LLR values are deinterleaved and decoded by the ML decoder.

The upper bound for the ABEP of the coded PPM-BPOLSK system with HID

assuming perfect interleaving is given by (4.20) where p is BSC transition probability which is the ABEP given in (5.6) for the uncoded system.

Notice for the UEP coded system the upper bounds $\text{ABEP}^{\text{C}}_{\text{SOP}}$ and $\text{ABEP}^{\text{C}}_{\text{symbol}}$ of the coded system can be evaluated using the same approach by substituting (5.23) and (5.24) for p in (4.21), respectively for HID.

For SID the LLRs for both SOP and symbol dimensions should be evaluated. LLR for the polarization dimension is given by

$$\begin{aligned} L(\check{p}) &= \log \frac{\text{Prob}(\check{p}=1|\mathbf{V})}{\text{Prob}(\check{p}=0|\mathbf{V})} \\ &= \log \frac{\sum_{m=1}^{M} \exp\left(-||\mathbf{V}-\mathbf{s}_{p,m}||^2/\sigma_n^2\right)}{\sum_{m=1}^{M} \exp\left(-||\mathbf{V}-\mathbf{s}_{p',m}||^2/\sigma_n^2\right)}, \end{aligned} \tag{5.25}$$

where we assume $\check{p}=1$ and $\check{p}=0$ correspond to $\wp=p$ and $\wp=p'$ states, respectively. On the other hand LLRs for the symbol dimension can be written as

$$\begin{aligned} L(m^j) &= \log \frac{\text{Prob}(m^j=1|\mathbf{V})}{\text{Prob}(m^j=0|\mathbf{V})} \\ &= \log \frac{\sum_{\wp\in\{p,p'\}} \sum_{\mathbf{m}^j\in\mathbf{m}_1^j} \exp\left(-||\mathbf{V}-\mathbf{s}_{\wp,m}||^2/\sigma_n^2\right)}{\sum_{\wp\in\{p,p'\}} \sum_{\mathbf{m}^j\in\mathbf{m}_0^j} \exp\left(-||\mathbf{V}-\mathbf{s}_{\wp,m}||^2/\sigma_n^2\right)}, \end{aligned} \tag{5.26}$$

where $\mathbf{m}_1^j$ and $\mathbf{m}_0^j$ represent vectors of symbols that have 1 and 0 at the j-th bit position, respectively.

The overall coded ABEP upper bound becomes

$$\text{ABEP}^{\text{C}} = \frac{\text{ABEP}^{\text{C}}_{\text{SOP}} + \log_2(M/2)\text{ABEP}^{\text{C}}_{\text{symbol}}}{\log_2(M)}, \tag{5.27}$$

and the effective code rate is given by

$$R = \frac{R_{SOP} + \log_2(M/2)R_s}{\log_2(M)}, \tag{5.28}$$

where R_{SOP} and R_s are the error protection rates of the SOP and symbol bits, respectively.

The simulation results for the $R = 7/10$ UEP with HID coded 4PPM-BPOLSK system is given in Figure 5.7-a where SOP and symbol bits are protected with $R_{SOP} = 3/4$ and $R_s = 2/3$, respectively. It is seen that there is almost no performance gap between the coded SOP and coded symbol BER curves.

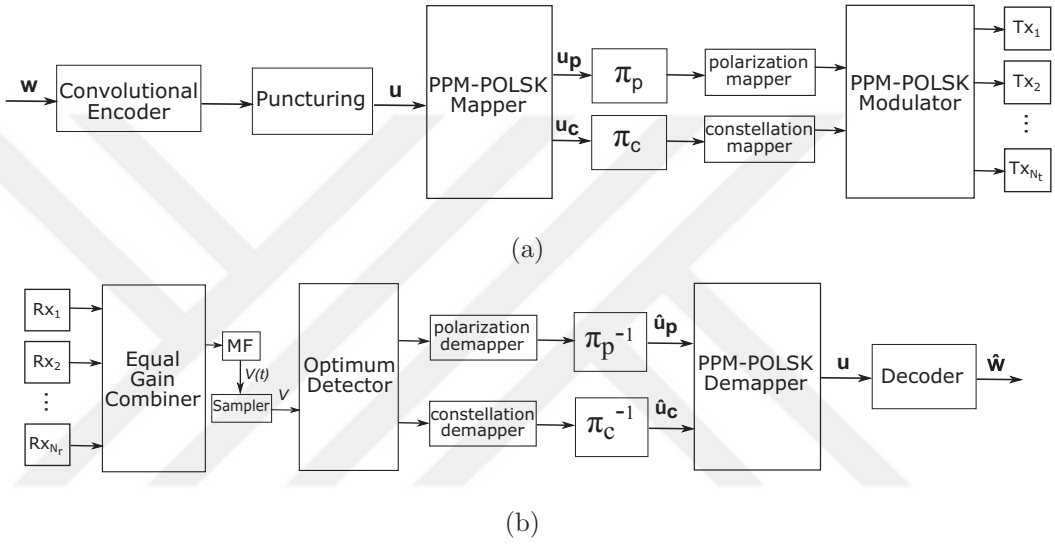

Figure 5.6. Transceiver model for the UEP coded PPM-BPOLSK system. (a) Transmitter model and (b) receiver model.

On the other hand the SM-MPOLSK system has 3 signalling dimensions (transmitter, SOP, constellation), and thus the redundancy of coding can be distributed to the dimension which is more vulnerable to turbulence effects.

For the SM-MPOLSK system the trasnmitter index, SOP and symbol ABEPs are given respectively by

$$\begin{aligned} \mathrm{ABEP_{tx}} \quad \leq \quad & \frac{1}{MN_t} \sum_{t=1}^{N_t} \sum_{\widehat{t}=1}^{N_t} \sum_{m=1}^{M} \sum_{\widehat{m}=1}^{M} \frac{N_{tx}^{e}}{\log_2 N_t} \\ & \mathrm{APEP}(t, m, \widehat{t}, \widehat{m} | \mathbf{h}_t, \mathbf{h}_{\widehat{t}}, \varepsilon_m, \varepsilon_{\widehat{m}}, \beta_m, \beta_{\widehat{m}}), \end{aligned} \tag{5.29}$$

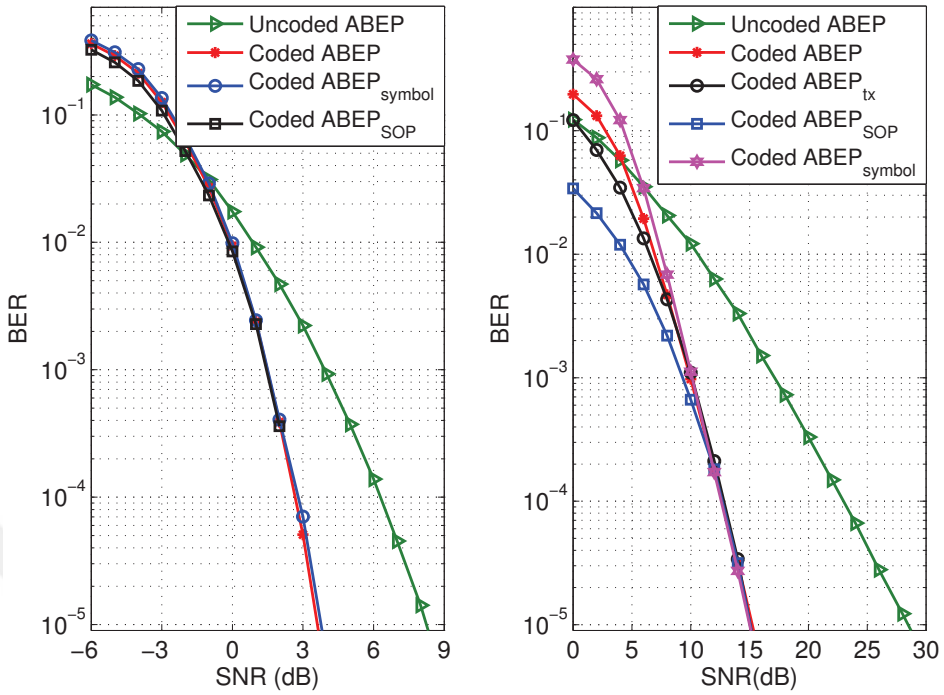

(a) (b)

Figure 5.7. Performance results for the coded (a) $R = 7/10$ UEP 4PPM-BPOLSK and (b) $R = 2/3$ UEP $N_t = 4$ SM-8POLSK systems under Gamma-Gamma fading with $\sigma_I^2 = 1.122$.

where N_{tx}^e is the number of transmitter index bits in error,

$$\text{ABEP}_{\text{SOP}} \leq \frac{1}{MN_t} \sum_{t=1}^{N_t} \sum_{\widehat{t}=1}^{N_t} \sum_{m=1}^{M} \sum_{\widehat{m}=1}^{M} N_{SOP}^e \text{APEP}(t, m, \widehat{t}, \widehat{m} | \mathbf{h}_t, \mathbf{h}_{\widehat{t}}, \varepsilon_m, \varepsilon_{\widehat{m}}, \beta_m, \beta_{\widehat{m}}), \tag{5.30}$$

where N_{SOP}^e is 0 if the SOP is detected correctly or 1 otherwise, and

$$\text{ABEP}_{\text{symbol}} \leq \frac{1}{MN_t} \sum_{t=1}^{N_t} \sum_{\widehat{t}=1}^{N_t} \sum_{m=1}^{M} \sum_{\widehat{m}=1}^{M} \frac{N_{symbol}^e}{\log_2(M/2)} \text{APEP}(t, m, \widehat{t}, \widehat{m} | \mathbf{h}_t, \mathbf{h}_{\widehat{t}}, \varepsilon_m, \varepsilon_{\widehat{m}}, \beta_m, \beta_{\widehat{m}}), \tag{5.31}$$

where N_{symbol}^e is the number of symbol bits in error.

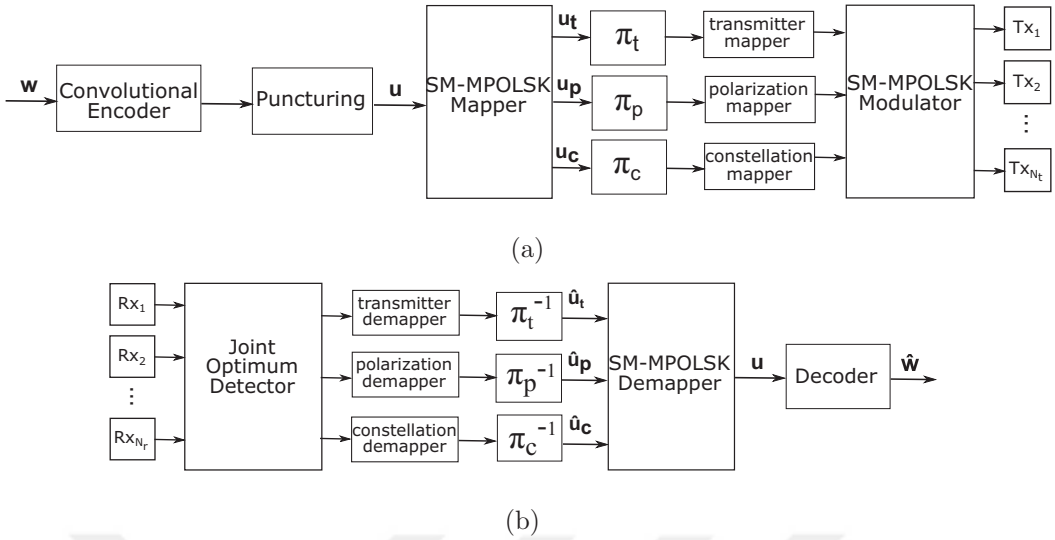

Figure 5.8. Transceiver model for the UEP coded SM-MPOLSK system. (a) Transmitter model and (b) receiver model.

For the SM-MPOLSK system for certain configurations such as $N_t = 4$ SM-8POLSK as seen in Figure 5.5-b, transmitter bits are more vulnerable to scintillation effects than SOP and symbol bits and SOP bits are the least effected bits. For this reason for such configurations we may apply coding with UEP and protect the more scintillation vulnerable bits more than other bits or even only the most vulnerable bits can be protected while the others are left unprotected.

For the coded UEP SM-MPOLSK system we add a convolutional encoder and an ML decoder to the transmitter and receiver sides of the original SM-MPOLSK system as seen in Figure 5.8. In this system after the input bitstream is encoded by a convolutional encoder the encoded bits are taken to the SM-MPOLSK modulator before the mapped transmitter index, SOP and symbol bits are interleaved separately. At the receiver side again both HID and SID are considered. For the HID system, bit groups belonging to each dimension are first demapped and deinterleaved separately and then decoded by the ML decoder to obtain the estimated information bits. For the SID on the other hand, first LLRs corresponding to each demapped bit group are calculated as done in [96], then these LLR values are deinterleaved and decoded again by the ML decoder.

The upper bound for the ABEP of the coded SM-MPOLSK system is given by (4.20) where p is the ABEP given in (5.21) for the uncoded system. Notice the upper bounds for $\text{ABEP}^{\text{C}}_{\text{tx}}$, $\text{ABEP}^{\text{C}}_{\text{SOP}}$ and $\text{ABEP}^{\text{C}}_{\text{symbol}}$ of the coded system can be evaluated by substituting (5.29), (5.30) and (5.31) for p in (4.21), respectively. For SID the LLRs for each dimension should be evaluated. LLR of the i-th constellation bit when t-th transmitter is active is computed by

$$\begin{aligned} L(t^i) &= \log \frac{\text{Prob}(t^i = 1|\mathbf{V})}{\text{Prob}(t^i = 0|\mathbf{V})} \\ &= \log \frac{\sum_{\mathbf{t}\in\mathbf{t}_1^i} \sum_{m=1}^{M} \exp\left(-||\mathbf{V} - \mathbf{x}_{t,m}||^2/\sigma_n^2\right)}{\sum_{\mathbf{t}\in\mathbf{t}_0^i} \sum_{m=1}^{M} \exp\left(-||\mathbf{V} - \mathbf{x}_{t,m}||^2/\sigma_n^2\right)} \end{aligned} \tag{5.32}$$

where $\mathbf{t}_1^i$ and $\mathbf{t}_0^i$ represent vectors of transmitter indices that have 1 and 0 at the i-th bit position, respectively. Similarly LLR for the polarization dimension is given by

$$\begin{aligned} L(m^1) &= \log \frac{\text{Prob}(m^1 = 1|\mathbf{V})}{\text{Prob}(m^1 = 0|\mathbf{V})} \\ &= \log \frac{\sum_{t=1}^{N_t} \sum_{\mathbf{m}^1\in\mathbf{m}_1^1} \exp\left(-||\mathbf{V} - \mathbf{x}_{t,m}||^2/\sigma_n^2\right)}{\sum_{t=1}^{N_t} \sum_{\mathbf{m}^1\in\mathbf{m}_0^1} \exp\left(-||\mathbf{V} - \mathbf{x}_{t,m}||^2/\sigma_n^2\right)} \end{aligned} \tag{5.33}$$

where $\mathbf{m}_1^1$ and $\mathbf{m}_0^1$ represent vectors of symbols that have 1 and 0 at the first bit position, respectively and LLRs for the symbol dimension can be written as

$$\begin{aligned} L(m^j) &= \log \frac{\text{Prob}(m^j = 1|\mathbf{V})}{\text{Prob}(m^j = 0|\mathbf{V})} \\ &= \log \frac{\sum_{t=1}^{N_t} \sum_{\mathbf{m}^j\in\mathbf{m}_1^j, j\neq 1} \exp\left(-||\mathbf{V} - \mathbf{x}_{t,m}||^2/\sigma_n^2\right)}{\sum_{t=1}^{N_t} \sum_{\mathbf{m}^j\in\mathbf{m}_0^j, j\neq 1} \exp\left(-||\mathbf{V} - \mathbf{x}_{t,m}||^2/\sigma_n^2\right)} \end{aligned} \tag{5.34}$$

where $\mathbf{m}_1^j$ and $\mathbf{m}_0^j$ represent vectors of symbols that have 1 and 0 at the j-th bit position with $j \neq 1$, respectively.

The overall coded ABEP upper bound becomes

$$\text{ABEP}^{\text{C}} = \frac{\log_2(N_t)\text{ABEP}^{\text{C}}_{\text{tx}} + \text{ABEP}^{\text{C}}_{\text{SOP}} + \log_2(M/2)\text{ABEP}^{\text{C}}_{\text{symbol}}}{\log_2(N_t M)}, \tag{5.35}$$

and the effective code rate is given by

$$R = \frac{\log_2(N_t)R_{tx} + R_{SOP} + \log_2(M/2)R_s}{\log_2(N_t M)} \tag{5.36}$$

where R_{tx}, R_{SOP} and R_s are the error protection rates of the transmitter index, SOP and symbol bits, respectively.

For this coded UEP system instead of generating bits with separate code generators for each dimension we can use a mother code generator and puncture it to satisfy a certain rate R. By appropriate punctured bit mapping for the transmitter index, SOP and symbol dimensions we can obtain miscellaneous code rates for each dimension. A sample mapping for a $R = 5/8$ coded $N_t = 4$ 16POLSK system is given in Table 5.2 for demonstration purposes where the transmission is assumed to be in 2400 bits length packets. For this system 1500 input bits are passed through a rate-1/2 encoder to obtain 3000 bits, 600 of which are cleared with puncturing.

Table 5.2. A sample bit mapping for $R = 5/8$ coded $N_t = 4$ 16POLSK system obtained with rate-1/2 encoder and puncturing

	Tx	SOP	Symbol	Total
Number of input bits	400	300	800	1500
Number of output bits	800	600	1600	3000
Number of cleared bits	0	200	400	600
Number of transmitted bits	800	400	1200	2400
Code rate	1/2	3/4	2/3	5/8

A sample selection with corresponding spectral efficiencies is shown in Table 5.3 for $N_t \in \{1, 2, 4, 8\}$, $M \in \{1, 2, 4, 8, 16\}$ and $R \in \{1, 1/2, 2/3, 3/4, 3/5\}$.

In Figure 5.7-b $R = 2/3$ UEP with HID performance results are given for the

same system considered in Figure 5.5-b where transmitter index and symbol bits are protected with $R_{tx} = 1/2$ and $R_s = 2/3$, respectively and SOP bits are not coded ($R_{SOP} = 1$). As seen the performance gap between results belonging to different bit groups are almost vanished with UEP.

Table 5.3. Spectral efficiency of a sample selection of POLSK [2], SSK [3] and SM-MPOLSK

N_t	Modulation	Coding Type	Code Rate R	R_{tx}	R_{SOP}	R_{symbol}	Spectral eff. r (b/s/Hz)
1	2POLSK	-	1	-	-	-	1
2	SSK	-	1	-	-	-	1
1	8POLSK	EEP	1/2	-	1/2	1/2	1.5
2	SM-4POLSK	EEP	1/2	1/2	1/2	1/2	1.5
1	4POLSK	-	1	-	-	-	2
2	SM-2POLSK	-	1	-	-	-	2
2	SM-4POLSK	EEP	2/3	-	-	-	2
2	SM-4POLSK	UEP	2/3	1/2	1	1/2	2
4	SSK	-	1				2
4	SM-2POLSK	UEP	2/3	1/2	1	1	2
8	SSK	-	1	-	-	-	3
4	SM-2POLSK	-	1	-	-	-	3
4	SM-4POLSK	EEP	3/4	3/4	3/4	3/4	3
1	16POLSK	EEP	3/4	-	3/4	3/4	3
4	SM-8POLSK	UEP	3/5	1/2	3/4	2/3	3
4	SM-4POLSK	-	1	-	-	-	4
8	SM-2POLSK	-	1	-	-	-	3

5.4. Simulation Results

We present in this section the simulation results on the error performance of PPM-BPOLSK and SM-MPOLSK systems over log-normal and Gamma-Gamma distributed FSO channels for various configurations. The FSO system is simulated with a wavelength of $\lambda = 1.55\ \mu$m, a link distance of $L = 2.5$ km and a receive aperture diameter of $D = 1$ cm, considering spherical waves. The structure parameter C_n^2 is chosen as 1.26×10^{-14} and 4.76×10^{-14} m$^{-2/3}$ for weak and strong turbulence conditions, respectively. These values correspond to $\sigma_I^2 = 0.5$ for weak turbulence, and $\sigma_I^2 = 1.22$ with $\alpha = 2.21$, $\beta = 1.89$ for strong turbulence.

For coded systems, a simple convolutional code with constraint length 2, rate 1/2 and generator $(5, 7)_8$ in octal representation is employed at the transmitter side and Viterbi algorithm is used for the ML decoding. The 2/3 and 3/4 codes are generated by puncturing the rate-1/2 code according to the puncturing matrices given in [93]. The code rates, puncturing patterns, d_{free}, d and B_d values are given in Table 4.4. For the SID we use 3 bits of quantization.

5.4.1. Non-coherent PPM-BPOLSK system

The comparison of the theoretical ABEP upper bounds and the simulated performances for both log-normal and Gamma-Gamma fading channels are presented in Figure 5.9 for the PPM-BPOLSK system where the coded results are obtained by HID. In the figures, the theoretical upper bounds are plotted with dashed curves and all curves are drawn down to at least 1×10^{-5} BER levels. As seen from all the plots theoretical performance curves are in agreement with the simulation results and indeed form relatively tight bounds. The simulation results for PPM-BPOLSK system is given in Figure 5.10 for log-normal and Gamma-Gamma distributed channels. As seen by adding PPM to BPOLSK we can achieve lower BER values compared to BPOLSK. In addition PPM-BPOLSK, compared to PPM with the same number of pulse position levels, achieves the same or slightly better performance results for weak and strong turbulence conditions, respectively with an additional $1/M$ spectral efficiency.

However this benefit comes at the cost of increased computational complexity at the receiver side, because as the number of position levels increase the required number of mathematical operations in the ML detection process grows rapidly.

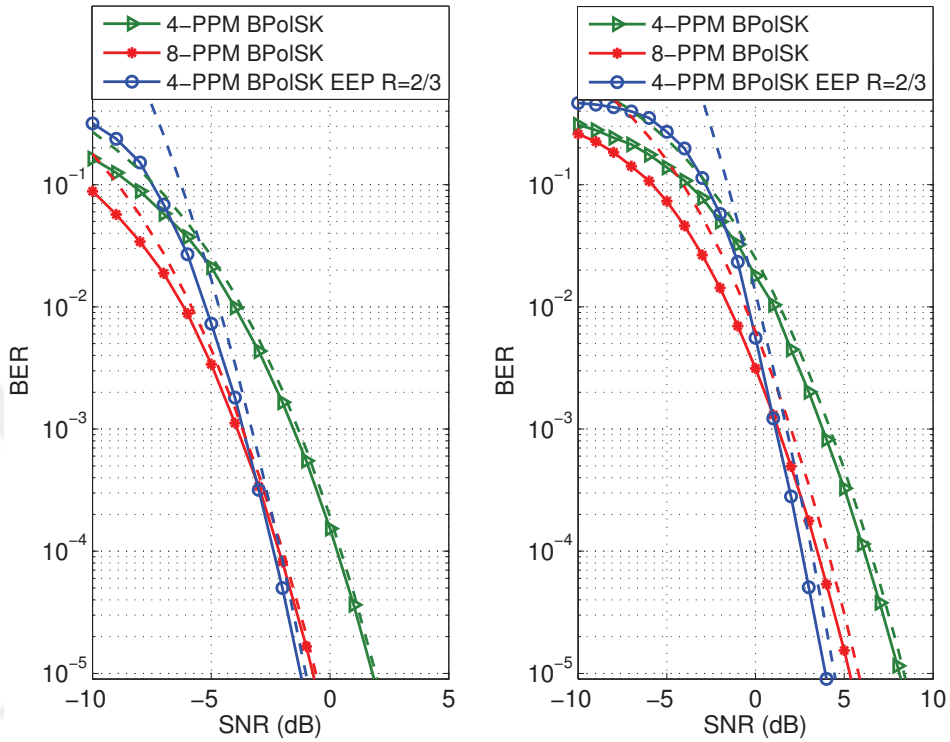

(a) (b)

Figure 5.9. Performance results and theoretical upper bounds for the uncoded and coded PPM-BPOLSK systems under (a) log-normal fading with $\sigma_I^2 = 0.5$ and (b) Gamma-Gamma fading with $\sigma_I^2 = 1.22$.

5.4.2. Coherent SM-POLSK system

The comparison of the numerical ABEP upper bounds and the simulated performances for both log-normal and Gamma-Gamma fading channels are presented in Figure 5.11 for the SM-MPOLSK system where the coded results are obtained by HID. Again in the figures, the upper bounds are plotted with dashed curves and all curves are drawn down to 1×10^{-5} BER levels. As seen from all the plots numerical performance curves are in agreement with the simulation results and indeed form relatively tight bounds.

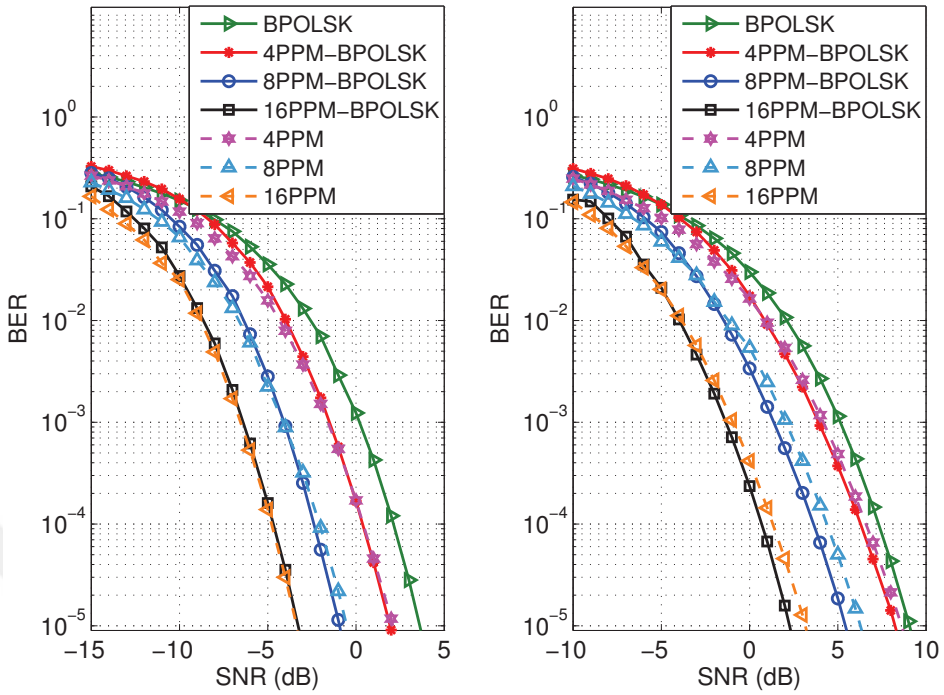

(a) (b)

Figure 5.10. Performance results for the PPM-BPOLSK system under (a) log-normal fading with $\sigma_I^2 = 0.5$ and (b) Gamma-Gamma fading with $\sigma_I^2 = 1.22$.

Simulation results showing the comparative performances of 2 and 3 b/s/Hz spectral efficiencies are given in Figure 5.12 and Figure 5.13, respectively. For the ease of illustration we only show the results for Gamma-Gamma fading and consider configurations including all MPOLSK, OSM (SPPAM or SSK) and SM-MPOLSK schemes and both uncoded and coded performances for comparison purposes. In these figures the EEP and UEP coded results are obtained with SID.

It is seen in Figure 5.12 for 2 b/s/Hz that the required SNR at 1×10^{-4} BER level is about 12dB for 4POLSK, whereas those for $N_t = 4$ SM-2POLSK with $R = 2/3$ UEP and $N_t = 4$ $(2, 1)$-SPPAM with $R = 2/3$ UEP are 7 and 18dB, respectively. That is the performance of $Nt = 4$ SM-2POLSK with $R = 2/3$ UEP, in which transmitter bits are protected with $R_{tx} = 1/2$ while the other bits are left unprotected ($R_{SOP} = 1, R_s = 1$), is better than those of the remaining MPOLSK, SSK and SPPAM schemes.

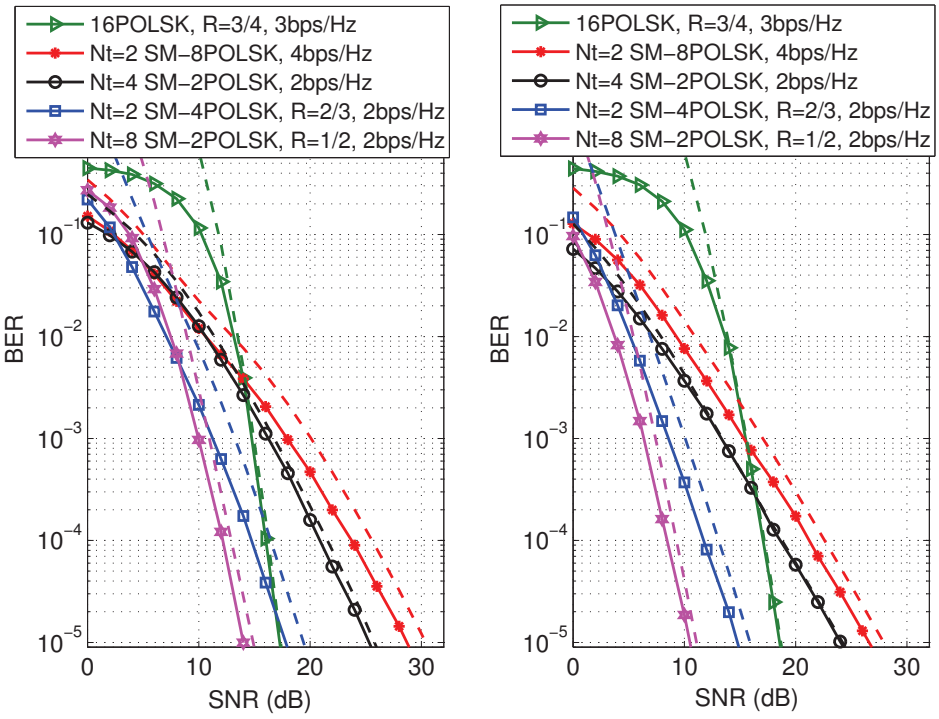

(a) (b)

Figure 5.11. Performance results and numerical upper bounds for the uncoded and coded SM-MPOLSK systems under (a) log-normal fading with $\sigma_I^2 = 0.5$ and (b) Gamma-Gamma fading with $\sigma_I^2 = 1.22$.

Additionally we observe the importance of UEP in this figure. With $N_t = 4$ we have to use 2 amplitude levels for $R = 1/2$ EEP (that is the $N_t = 4$ SM-4POLSK $R = 1/2$ EEP curve) to achieve 2 b/s/Hz spectral efficiency. On the other hand as seen from the $N_t = 4$ SM-2POLSK $R = 2/3$ UEP curve if we protect the most scintillation vulnerable transmitter bits with $R_{tx} = 1/2$ while leaving the SOP bit unprotected we can achieve the same performance using only a single amplitude level instead of 2.

Similar interpretations exist for the 3 b/s/Hz spectral efficiency results. As seen in Figure 5.13 at 1×10^{-4} BER level the performances of $N_t = 4$ SM-8POLSK with $R = 3/5$ UEP, $N_t = 8$ SM-4POLSK with $R = 3/5$ UEP, in which UEPs are attained by (R_{tx}, R_{SOP}, R_s) triple of $(1/2, 1, 1/2)$, and $N_t = 8$ SM-8POLSK with $R = 1/2$ EEP are all better than those of both 8POLSK and $R = 3/4$ 16POLSK. Apart from the performance gains attained, utilization of SM can reduce the required amplitude

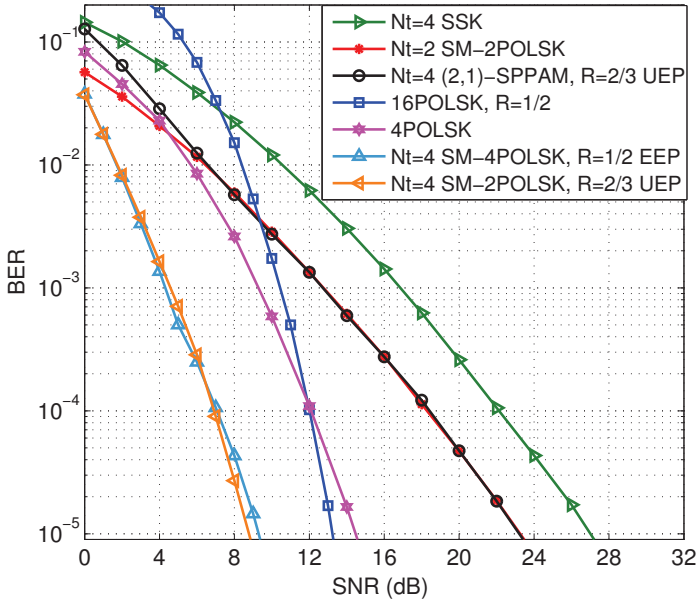

Figure 5.12. Performance results at 2 b/s/Hz under Gamma-Gamma fading with $\sigma_I^2 = 1.22$.

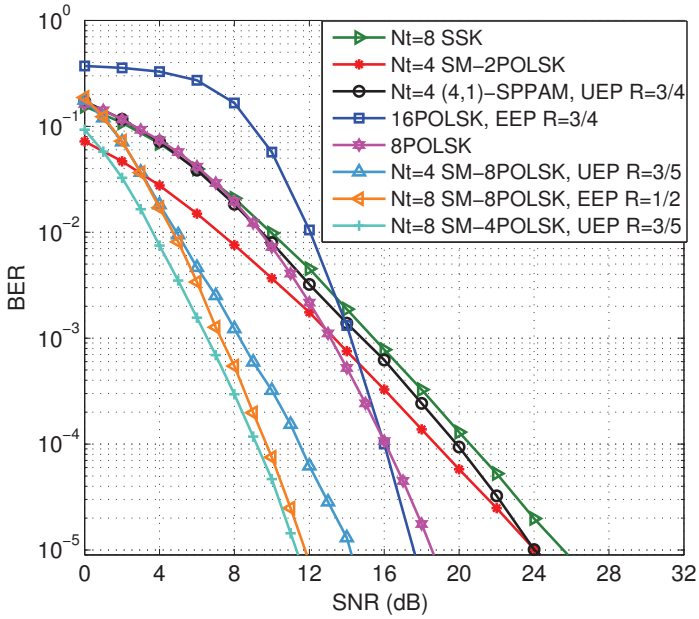

Figure 5.13. Performance results at 3 b/s/Hz under Gamma-Gamma fading with $\sigma_I^2 = 1.22$.

levels. Notice $N_t = 8$ SM-4POLSK with $R = 3/5$ UEP, which is the best performing scheme in the figure, uses only 2 constellation levels while 8POLSK and 16POLSK with $R = 3/4$ EEP schemes require 4 and 8 levels, respectively. Remember using high order constellation levels cause higher PAPR's and sensitivity to channel nonlinearities and noise, and thus must be avoided. By distributing some of the bits to the spatial and polarization domains the required number of constellation levels for a certain spectral efficiency can be decreased. Again the importance of UEP is apparent in this figure. For the $N_t = 8$ SM-4POLSK with $R = 3/5$ UEP configuration both the required SNR and the used amplitude levels are reduced compared to $N_t = 8$ SM-8POLSK with $R = 1/2$ EEP.

5.5. Conclusion

We proposed two POLSK based optical MIMO communication techniques. The first technique, PPM-BPOLSK, offers power efficiency over conventional optical communication systems. By combining the power efficiency property of PPM and POLSK, PPM-BPOLSK provides reduction in the required number of positions of PPM. The other technique, SM-MPOLSK on the other hand offers spectral/power/performance efficiencies over conventional systems. By distributing some of the bits to the spatial and SOP domains SM-MPOLSK provides reduction in the required number of amplitude levels which in turn reduces the risk of optical device's working in its nonlinear region. We also demonstrated for both systems that different bit groups may be effected by the scintillation at different levels and thus offering UEP for each bit group not only closes the gap between individual BER performances of each group but also improves overall performance significantly in comparison to the cases where conventional EEP is employed for all signalling dimensions.

6. CONCLUSION AND FUTURE WORK

FSO applications, with their potential in providing high data rate and cost effective communications, are among the most promising technologies to overcome the limitations of contemporary communication systems and satisfy the ever increasing demand for higher speed data sharing. For this reason, development of novel FSO systems and improvement of the existing ones have been a very popular research area in the last decades. Within this context, the objective of this dissertation has been to study the design and performance analysis of MIMO FSO communication systems over atmospheric turbulence channels in order to contribute to the field of research and fill the existing research gaps.

With this motivation we first provided the background material in Chapter 2 to permit the readers to understand the dissertation statement and prepare them for what would be argued in the dissertation. The attractive aspects and challenges of FSO systems as well as the importance of atmospheric effects such as attenuation and turbulence are discussed and an overview regarding to the optical modulation and detection methods along with the techniques used for scintillation mitigation is also provided in this chapter.

Then in Chapter 3 we mentioned to the issue of inter-aperture separation in MIMO FSO links and presented a unified framework that provides design guidelines for resolvable paths in these links. The channel correlation is dependent on several parameters including link distance, aperture size, wavelength, turbulence strength and also the wave's being a plane or a spherical wave. Considering all these parameters and using Rytov and extended Rytov theories we provided expressions to evaluate the correlation length and thus the aperture separations. Results show that the required separations ensuring independent paths are on the order of a few ten centimeters for practical FSO configurations working at ranges up to a few kilometers even when zero correlation condition is satisfied. The proposed framework can also be used to determine the amount of channel correlation for specific system configurations.

Chapter 4 introduced a novel spectrally efficient optical modulation method, denoted by SPPAM, which applies the famous SM approach to the FSO atmospheric turbulence channels for the first time in the literature. We provided an upper bounding framework for the evaluation of ABEP of the proposed SPPAM system considering both log-normal and Gamma-Gamma distributed channels. We first compared the performance of SPPAM with those of other spectrally efficient modulation techniques and showed that SPPAM can attain better performance results compared to both spatial multiplexing and SSK with smaller number of transmitters. Additionally when error control coding is exploited we can use arbitrary coding rates for SPPAM with neither decreasing the spectral efficiency nor increasing the number of transmitters, whereas SSK lacks such flexibility since the only way to increase the spectral efficiency is to at least double the number of transmitters. We then showed the performance superiority of SPPAM over the classical diversity systems exploiting aperture averaging and EGC, however this superiority comes at the expense of increased receiver computational complexity. Finally we investigated the effect of turbulence severity on the performance of the SPPAM system and showed that SM brings a certain degree of robustness against the variations in the channel turbulence effects. In summary this chapter proposed and modeled a novel FSO SM system offering design flexibility over conventional optical communication systems in terms of power and spectral efficiencies.

In Chapter 5 first POLSK was considered in a non-coherent MIMO architecture to offer power efficiency. We showed that by transmitting PPM signals through the polarization dimension the power efficiency of the standard non-coherent BPOLSK system can be substantially increased at the cost of increased decoding complexity. So we deduced that the proposed PPM-BPOLSK system offers a compromise between spectral and power efficiencies of standard uses of BPOLSK and PPM schemes, respectively. In this chapter we also developed the SM principle of Chapter 4 further to include the polarization dimension as an additional signalling dimension introducing a novel POLSK based coherent SM system that offers especially spectral efficiency advantages over other spectrally efficient optical modulation schemes. By distributing some of the bits to the spatial and SOP domains SM-MPOLSK provides reduction

in the required number of amplitude levels, which is very important for optical communication systems in terms of preventing high PAPR's and so reducing the risk of optical device's working in its nonlinear region. We finally evaluated the error ratios corresponding to each signalling dimension of these POLSK based MIMO systems separately and showed that bits belonging to different dimensions are affected unequally from the channel impairments. So the final contribution of both Chapter 5 and the dissertation was the introduction of UEP to the POLSK based MIMO FSO systems in order to optimize the performance gains obtained by error control coding.

Although we have completed the research objectives listed in Chapter 1, the following future work might extend the contributions of the dissertation:

- We offered UEP for PPM-BPOLSK and SM-MPOLSK systems, which have multiple signalling dimensions. However, the SPPAM, MPOLSK, coherent OSM and indoor OSM techniques offered in Chapter 4, [43], [13] and [34], respectively also possess multiple dimensions. For this reason the benefits of UEP can be investigated for these systems, too.
- For the ease of demonstration we used simple convolutional codes for the UEP systems considered in Chapter 5. Therefore implementation of more complex codes such as LDPC and spatially coupled codes for the UEP framework constitutes a future work. Additionally the optimization of code rates corresponding to each separate dimension to maximize the performance gains is still an open problem.
- The benefits of the coherent OSM method of [13] can be further increased by incorporating the benefits of the MPOLSK scheme considered in Chapter 5.
- The influence of pointing and channel estimation errors can be considered for the proposed SPPAM, PPM-BPOLSK and SM-MPOLSK systems.

Bibliography

1. Ghassemlooy, Z., W. Popoola and S. Rajbhandari, *Optical Wireless Communications: System and Channel Modelling with MATLAB*, CRC Press, Inc, Boca Raton, FL, USA, 2012.

2. Tang, X., Z. Ghassemlooy, S. Rajbhandari, W. O. Popoola and C. G. Lee, "Coherent Polarization Shift Keying Modulated Free Space Optical Links over a Gamma-Gamma Turbulence Channel", *American Journal of Engineering and Applied Sciences*, Vol. 4, No. 4, pp. 520–530, 2011.

3. Jeganathan, J., A. Ghrayeb, L. Szczecinski and A. Ceron, "Space Shift Keying Modulation for MIMO Channels", *IEEE Transactions on Wireless Communications*, Vol. 8, No. 7, pp. 3692–3703, 2009.

4. Bouchet, O., H. Sizun, C. Boisrobert, F. D. Fornel and P. N. Favennec, *Free-Space Optics: Propagation and Communication*, ISTE Ltd., London, UK, 2006.

5. Ghassemlooy, Z. and W. O. Popoola, *Mobile and Wireless Communications: Network Layer and Circuit Level Design*, InTech, Rijeka, Croatia, 2010.

6. Andrews, L. C. and R. L. Phillips, *Laser Beam Propagation Through Random Media*, SPIE Press, Bellingham, WA, USA, 2005.

7. Shieh, W. and I. Djordjevic, *OFDM for Optical Communications*, Academic Press, New York, NY, USA, 2010.

8. Henniger, H. and O. Wilfert, "An Introduction to Free-Space Optical Communications", *Radioengineering*, Vol. 19, No. 2, pp. 203–212, 2010.

9. Garlington, T., J. Babbitt and G. Long, *Analysis of Free Space Optics as a Transmission Technology*, Technical Report, US Army Informations Systems Engineer-

ing Command (UAISEC) 5, 2005.

10. Kedar, D. and S. Arnon, "Urban Optical Wireless Communication Networks: The Main Challenges and Possible Solutions", *IEEE Communications Magazine*, Vol. 42, No. 5, pp. S2–S7, 2004.

11. Zhu, X. and J. M. Kahn, "Free-Space Optical Communication through Atmospheric Turbulence Channels", *IEEE Transactions on Communications*, Vol. 50, No. 8, pp. 1293–1300, 2002.

12. Nistazakis, H. E., T. A. Tsiftsis and G. S. Tombras, "Performance Analysis of Free-Space Optical Communication Systems over Atmospheric Turbulence Channels", *IET Communications*, Vol. 3, No. 8, pp. 1402–1409, 2009.

13. Peppas, K., H. E. Nistazakis, V. D. Assimakopoilos and G. S. Tombras, "Performance Analysis of SISO and MIMO FSO Communication Systems Over Turbulent Channels", *INTECH Open Access Publisher*, pp. 415–438, 2012.

14. Kahn, J. M., "Modulation and Detection Techniques for Optical Communication Systems", *Proceedings of Coherent Optical Technologies and Applications*, 2006.

15. Uysal, M., J. Li and M. Yu, "Error Rate Performance Analysis of Coded Free-Space Optical Links over Gamma-Gamma Atmospheric Turbulence Channels", *IEEE Transactions on Wireless Communications*, Vol. 5, No. 6, pp. 1229–1233, 2006.

16. Zhu, X. and J. M. Kahn, "Performance Bounds for Coded Free-Space Optical Communications through Atmospheric Turbulence Channels", *IEEE Transactions on Communications*, Vol. 51, No. 8, pp. 1233–1239, 2003.

17. Letzepis, N. and A. G. Fabregas, "Outage Probability of the Gaussian MIMO Free-Space Optical Channel with PPM", *IEEE Transactions on Communications*, Vol. 57, No. 12, pp. 3682–3690, 2009.

18. Bayaki, E., R. Schober and R. K. Mallik, "Performance Analysis of MIMO Free-Space Optical Systems in Gamma-Gamma Fading", *IEEE Transactions on Communications*, Vol. 57, No. 11, pp. 3415–3424, 2009.

19. Navidpour, S. M., M. Uysal and M. Kavehrad, "BER Performance of Free-Space Optical Transmission with Spatial Diversity", *IEEE Transactions on Wireless Communications*, Vol. 6, No. 8, pp. 2813–2819, 2007.

20. Lee, E. and V. Chan, "Part 1: Optical Communication over the Clear Turbulent Atmospheric Channel Using Diversity", *IEEE Journal on Selected Areas in Communications*, Vol. 22, No. 9, pp. 1896–1906, 2004.

21. Vetelino, F. S., C. Young, L. C. Andrews and J. Recolons, "Aperture Averaging Effects on the Probability Density of Irradiance Fluctuations in Moderate-to-Strong Turbulence", *Applied Optics*, Vol. 46, No. 11, pp. 2099–2108, 2007.

22. Simon, M. K. and V. Vilnrotter, "Alamouti-Type Space-Time Coding for Free-Space Optical Communication with Direct Detection", *IEEE Transactions on Wireless Communications*, Vol. 4, No. 1, pp. 35–39, 2005.

23. Abou-Rjeily, C. and W. Fawaz, "Space-Time Codes for MIMO Ultra-Wideband Communications and MIMO Free-Space Optical Communications with PPM", *IEEE Journal on Selected Areas in Communications*, Vol. 26, No. 6, pp. 938–947, 2008.

24. Bayaki, E. and R. Schober, "On Space-Time Coding for Free-Space Optical Systems", *IEEE Transactions on Communications*, Vol. 58, No. 1, pp. 58–62, 2010.

25. Abaza, M., R. Mesleh, A. Mansour and E. M. Aggoune, "Diversity Techniques for a Free-Space Optical Communication System in Correlated Log-normal Channels", *Optical Engineering*, Vol. 53, No. 1, pp. 016102–016102, 2014.

26. Wilson, S. G., M. Brandt-Pearce, Q. Cao and J. Leveque, "Free-Space Optical

MIMO Transmission with Q-ary PPM", *IEEE Transactions on Communications*, Vol. 53, No. 8, pp. 1402–1412, 2005.

27. Letzepis, N., I. Holland and W. Cowley, "The Gaussian Free Space Optical MIMO Channel with Q-ary Pulse Position Modulation", *IEEE Transactions on Wireless Communications*, Vol. 7, No. 5, pp. 1744–1753, 2008.

28. Tyson, R. K., "Bit Error Rate for Free Space Adaptive Optics Laser Communications", *Journal of the Optical Society of America A.*, Vol. 19, No. 4, pp. 753–758, 2002.

29. Zhu, X. and J. M. Kahn, "Markov Chain Model in Maximum-Likelihood Sequence Detection for Free-Space Optical Communication through Atmospheric Turbulence Channels", *IEEE Transactions on Communications*, Vol. 51, No. 3, pp. 509–516, 2003.

30. H.H. Refai, P. L., "Switched Diversity Approach for Multireceiving Optical Wireless Systems", *IEEE Transactions on Communications*, Vol. 5, pp. 5606–5614, 2011.

31. Abaza, M., R. Mesleh, A. Mansour and E. M. Aggoune, "Performance Analysis of MISO Multi-hop FSO Links over Log-normal Channels with Cog and Beam Divergence Attenuations", *Optics Communications*, Vol. 334, No. 3, pp. 247–252, 2015.

32. Cheng, Y. and S. Hwang, "Subcarrier Intensity Modulation/Spatial Modulation for Optical Wireless Communications", *IEICE Transactions on Commununications*, Vol. 97, No. 5, pp. 1086–1093, 2014.

33. Yang, G., M. Khalighi, T. Virieux, S. Bourennane and Z. Ghassemlooy, "Contrasting Space-Time Schemes for MIMO FSO Systems with Non-Coherent Modulation", *IEEE International Workshop on Optical Wireless Communications*, pp. 1–3, 2012.

34. Mesleh, R., H.Elgala and H. Haas, "Optical Spatial Modulation", *Journal of Optical Commununications and Networking*, Vol. 3, No. 3, pp. 234–244, 2011.

35. Mesleh, R., H. Elgala, R. Mehmood and H. Haas, "Performance of Optical Spatial Modulation with Transmitters-Receivers Alignment", *IEEE Communications Letters*, Vol. 15, No. 1, pp. 79–81, 2011.

36. Popoola, W., E. Poves and H. Haas, "Spatial Pulse Position Modulation for Optical Communications", *Journal of Ligthwave Technology*, Vol. 30, No. 18, pp. 2948–2954, 2012.

37. Fath, T., H. Haas, M. D. Renzo and R. Mesleh, "Spatial Modulation Applied to Optical Wireless Communications in Indoor LOS Environments", *Proceedings of IEEE Global Telecommunications Conference*, Vol. 15, No. 1, pp. 1–5, 2011.

38. Zhao, X., Y. Yao, Y. Sun, and C. Liu, "Circle Polarization Shift Keying with Direct Detection for Free-Space Optical Communication", *Journal of Optical Commununications and Networking*, Vol. 1, No. 4, pp. 307–312, 2009.

39. Benedetto, S. and P. Poggiolini, "Theory of Polarization Shift Keying Modulation", *IEEE Transactions on Commununications*, Vol. 40, No. 4, pp. 708–721, 1992.

40. Karbassian, M. M. and H. Ghafouri-Shiraz, "Transceiver Architecture for Incoherent Optical CDMA Network Based on Polarization Modulation", *Journal of Lightwave Technology*, Vol. 26, No. 24, pp. 3820–3828, 2008.

41. Sugianto, T. and C. Davis, "Performance of Free Space Optical Communication Systems Using Polarization Shift Keying Modulation", *Proceedings of SPIE International Society for Optics and Photonics*, pp. 63040V–63040V, 2006.

42. Tang, X., Z. Ghassemlooy and S. Rajbhandari, "Experimental Investigation of Polarisation Modulated Free Space Optical Communication with Direct Detection

in a Turbulence Channel", *IET Communications*, Vol. 6, No. 11, pp. 1489–1494, 2012.

43. Tang, X., Z. Ghassemlooy, S. Rajbhandari, W. O. Popoola and C. G. Lee, "Coherent Heterodyne Multilevel Polarization Shift Keying with Spatial Diversity in a Free-Space Optical Turbulence Channel", *Journal of Lightwave Technology*, Vol. 30, No. 16, pp. 2689–2695, 2012.

44. Tang, X., Z. Xu and Z. Ghassemlooy, "Coherent Polarization Modulated Transmission through MIMO Atmospheric Optical Turbulence Channel", *Journal of Lightwave Technology*, Vol. 31, No. 20, pp. 3221–3228, 2013.

45. Prabu, K. and D. S. Kumar, "MIMO Free-Space Optical Communication Employing Coherent BPOLSK Modulation in Atmospheric Optical Turbulence Channel with Pointing Errors", *Optics Communications*, Vol. 343, pp. 188–194, 2015.

46. Özbilgin, T. and M. Koca, "Optical Spatial Modulation over Atmospheric Turbulence Channels", *Journal of Lightwave Technology*, Vol. 33, No. 11, pp. 2313–2323, 2015.

47. Hwang, S.-H. and Y. Cheng, "SIM/SM-Aided Free-Space Optical Communication with Receiver Diversity", *Journal of Lightwave Technology*, Vol. 32, No. 14, pp. 2443–2450, 2014.

48. Bloom, S. and W. S. Harley, "The Last-Mile Solution: Hybrid FSO Radio", *AirFiber Inc.*, pp. 1–20, 2002.

49. Douik, A., H. Dahrouj, T. Y. Al-Naffouri and M. S. Alouini, "Hybrid Radio/Free-Space Optical Design for Next Generation Backhaul Systems", *arXiv preprint arXiv:1502.00137*, 2015.

50. Hanson, F. and S. Radi, "High Bandwidth Underwater Optical Communication", *Applied Optics*, Vol. 47, No. 2, pp. 277–283, 2008.

51. Hemmati, H., *Near-Earth Laser Communications*, CRC Press, Inc, Boca Raton, FL, USA, 2009.

52. Ramirez-Iniguez, R., S. M. Idrus and Z. Sun, *Optical Wireless Communications: IR for Wireless Commectivity*, CRC Press, Inc, Boca Raton, FL, USA, 2008.

53. Muhammad, S. S., B. Flecker, E. Leitgeb and M. Gebhart, "Characterization of Fog Attenuation in Terrestrial Free Space Optical Links", *Optical Engineering*, Vol. 46, No. 6, pp. 066001–066001, 2007.

54. Strohbehn, J. W., *Laser Beam Propagation in the Atmosphere*, Springer-Verlag, Berlin-Heidelberg-New York, 1978.

55. Hill, R. J. and R. G. Frehlich, "Probability Distribution of Irradiance for the Onset of Strong Scintillation", *Journal of the Optical Society of America A.*, Vol. 14, No. 7, pp. 1530–1540, 1997.

56. Jakeman, E., "On the Statistics of K-distributed Noise", *Journal of Physics A: Mathematics and General*, Vol. 13, pp. 31–48, 1980.

57. Farid, A. A. and S. Hranilovic, "Outage Capacity Optimization for Free-Space Optical Links with Pointing Errors", *Journal of Lightwave Technology*, Vol. 25, No. 7, pp. 1702–1709, 2002.

58. Popoola, W. O. and Z. Ghassemlooy, "BPSK Subcarrier Intensity Modulated Free-Space Optical Communications in Atmospheric Turbulence", *Journal of Lightwave Technology*, Vol. 27, No. 8, pp. 967–973, 2009.

59. Gappmair, W., S. Hranilovic, and E. Leitgeb, "Performance of PPM on Terrestrial FSO Links with Turbulence and Pointing Errors", *IEEE Communication Letters*, Vol. 14, No. 5, pp. 468–470, 2010.

60. Fried, D. L., "Optical Heterodyne Detection of an Atmospherically Distorted Sig-

nal Wave Front", *Proceedings of the IEEE*, Vol. 55, No. 1, pp. 57–77, 1967.

61. Safari, M. and M. Uysal, "Do We Really Need OSTBCs for Free-Space Optical Communication with Direct Detection?", *IEEE Transactions on Wireless Communications*, Vol. 7, No. 11, pp. 4445–4448, 2008.

62. Djordjevic, I., W. Ryan and B. Vasic, *Coding for Optical Channels*, Springer Science & Business Media, New York, Dordrecht, Heidelberg, London, 2010.

63. Chan, V. W. S., "Coding for the Turbulent Atmospheric Optical Channel", *IEEE Transactions on Communications*, Vol. 30, No. 1, pp. 269–275, 1982.

64. Davidson, F. M. and Y. T. Koh, "Interleaved Convolutional Coding for the Turbulent Atmospheric Optical Communication Channel", *IEEE Transactions on Communications*, Vol. 36, No. 9, pp. 993–1003, 1988.

65. Xu, F., M. A. Khalighi and S. Bourennane, "Coded PPM and Multipulse PPM and Iterative Detection for Free-Space Optical Links", *Journal of Optical Communications and Networking*, Vol. 1, No. 5, pp. 404–415, 2009.

66. Djordjevic, I. B., S. Denic, J. Anguita, B. Vasic and M. A. Neifeld, "LDPC-Coded MIMO Optical Communication over the Atmospheric Turbulence Channel", *Journal of Lightwave Technology*, Vol. 26, No. 5, pp. 478–487, 2008.

67. Anguita, J. A., M. A. Neifeld and B. Hildner, "Rateless Coding on Experimental Temporally Correlated FSO Channels", *Journal of Lightwave Technology*, Vol. 28, No. 7, pp. 990–1002, 2010.

68. Grave, J. E. and S. Drenker, "Advancing Free Space Optical Communication with Adaptive Optics", *Lightwaveonline*, Vol. 19, pp. 105–113, 2002.

69. Loyka, S. L., "Channel Capacity of MIMO Architecture Using the Exponential Correlation Matrix", *IEEE Communications Letters*, Vol. 5, No. 9, pp. 369–371,

2001.

70. Kazemi, H., Z. Mostaani, M. Uysal and Z. Ghassemlooy, "Outage Performance of MIMO Free-Space Optical Systems in Gamma-Gamma Fading Channels", *IEEE 18th European Conference on Networking and Optical Communications*, pp. 275–280, 2013.

71. Khalighi, M., N. Schwartz, N. Ataimer and S. Bourennane, "Fading Reduction by Aperture Averaging and Spatial Diversity in Optical Wireless Systems", *Journal of Optical Communications and Networking*, Vol. 1, No. 6, pp. 580–593, 2009.

72. Louthain, J. A. and J. D. Schmidt, "Anisoplanatism in airborne laser communication", *Optics Express*, Vol. 16, No. 14, pp. 10769–10785, 2008.

73. Anguita, J. A., M. A. Neifeld and B. V. Vasic, "Spatial Correlation and Irradiance Statistics in a Multiple-Beam Terrestrial Free-Space Optical Communication Link", *Journal of Applied Optics*, Vol. 46, No. 26, pp. 6561–6571, 2007.

74. Yang, G., M. A. Khalighi, S. Bourennane and Z. Ghassemlooy, "Fading Correlation and Analytical Performance Evaluation of the Space-Diversity Free-Space Optical Communications System", *Journal of Optics*, Vol. 16, No. 3, pp. 1–10, 2014.

75. Farid, A. A. and S. Hranilovic, "Diversity Gain and Outage Probability for MIMO Free-Space Optical Links with Misalignment", *IEEE Transactions on Communications*, Vol. 60, No. 2, pp. 479–487, 2012.

76. Garcia-Zambrana, A., B. Castillo-Vazquez and C. Castillo-Vazquez, "Asymptotic Error-Rate Analysis of FSO Links Using Transmit Laser Selection over Gamma-Gamma Atmospheric Turbulence Channels with Pointing Errors", *Optics Express*, Vol. 20, No. 3, pp. 2096–2109, 2012.

77. Farid, A. A. and S. Hranilovic, "Outage Capacity for MISO Intensity-Modulated Free-Space Optical Links with Misalignment", *Journal of Optical Commununica-*

tions and Networking, Vol. 3, No. 10, pp. 780–789, 2011.

78. Kazemlou, S., S. Hranilovic and S. Kumar, "All-Optical Multihop Free-Space Optical Communication Systems", *Journal of Lightwave Technology*, Vol. 29, No. 18, pp. 2663–2669, 2011.

79. Chen, Z., S. Yu, T. Wang, G. Wu, S. Wang and W. Gu, "Channel Correlation in Aperture Receiver Diversity Systems for Free-Space Optical Communication", *Journal of Optics*, Vol. 14, No. 12, pp. 1–7, 2012.

80. Ghassemlooy, Z., W. O. Popoola, V. Ahmadi and E. Leitgeb, "MIMO Free-Space Optical Communication Employing Subcarrier Intensity Modulation in Atmospheric Turbulence Channels", *LNICST: Commununications Infrastructure*, Vol. 16, pp. 61–73, 2009.

81. Song, X. and J. Cheng, "Subcarrier Intensity Modulated MIMO Optical Communications in Atmospheric Turbulence", *Journal of Optical Commununications and Networking*, Vol. 5, No. 9, pp. 1001–1009, 2013.

82. Zhang, H., W. Lii and T. A. Gulliver, "Pulse Position Amplitude Modulation for Time-Hopping Multiple-Access UWB Communications", *IEEE Transactions on Commununications*, Vol. 53, No. 8, pp. 1269–1273, 2005.

83. Anttonen, A., A. Kotelba and A. Maamela, "Energy Detection of Multilevel PAM Signals with Systematic Threshold Mismatch", *Research Letters in Communications*, Vol. 3, 2009.

84. Lee, E. A. and D. G. Messerschmitt, *Digital Communication*, Kluwer Academic Publishers, Boston, Dorddrecht, London, 1994.

85. Renzo, M. D. and H. Haas, "Performance Analysis of Spatial Modulation", *Proceedings of ICST/IEEE International Conference on Communications and Networking in China*, pp. 1–7, 2010.

86. Craig, J. W., "A New, Simple, and Exact Result for Calculating the Probability of Error for Two-Dimensional Signal Constellations", *Proceedings of IEEE Military Communications in a Changing World*, pp. 571–575, 1991.

87. Haas, S. M., "Capacity of and Coding for Multiple-Aperture Wireless Optical Communications", *Ph.D. Thesis*, 2003.

88. Mehta, N., J. Wu, A. Molisch and J. Zhang, "Approximating a Sum of Random Variables with a Lognormal", *IEEE Transactions on Wireless Communications*, Vol. 6, No. 7, pp. 2690–2699, 2007.

89. Rosenblatt, M., "Remarks on Some Nonparametric Estimates of a Density Function", *The Annals of Mathematical Statistics*, Vol. 27, No. 3, pp. 832–837, 1956.

90. Chatzidiamantis, N. D., G. K. Karagiannidis and D. S. Michalopoulos, "On the Distribution of the Sum of Gamma-Gamma Variates and Applications in RF and Optical Wireless Communications", *IEEE Transcations on Communications*, Vol. 59, No. 5, pp. 1298–1308, 2011.

91. Adamchick, V. S. and O. I. Marichev, "The Algorithm for Calculating Integrals of Hypergeometric Type Functions and Its Realization in REDUCE System", *Proceedings of the International Symposium on Symbolic & Algebraic Computation*, pp. 212–224, 1990.

92. S. Lin, D. J. C., *Error Control Coding*, Pearson Prentice Hall, New Jersey, NJ, USA, 1983.

93. Haccoun, D. and G. Begin, "High-Rate Punctured Convolutional Codes for Viterbi and Sequential Decoding", *IEEE Transactions on Commununications*, pp. 1113–1125, 1989.

94. Proakis, J. G., *Digital Communications*, McGraw-Hill, New York, NY, USA, 2001.

95. Masnick, B. and J. Wolf, "On Linear Unequal Error Protection Codes", *IEEE Transcations on Information Theory*, Vol. 13, No. 4, pp. 600–607, 1967.

96. Hwang, S. U., S. Jeon, S. Lee, and J. Seo, "Soft-Output ML Detector for Spatial Modulation OFDM Systems", *IEICE Electronics Express*, Vol. 6, No. 19, pp. 1426—1431, 2009.